



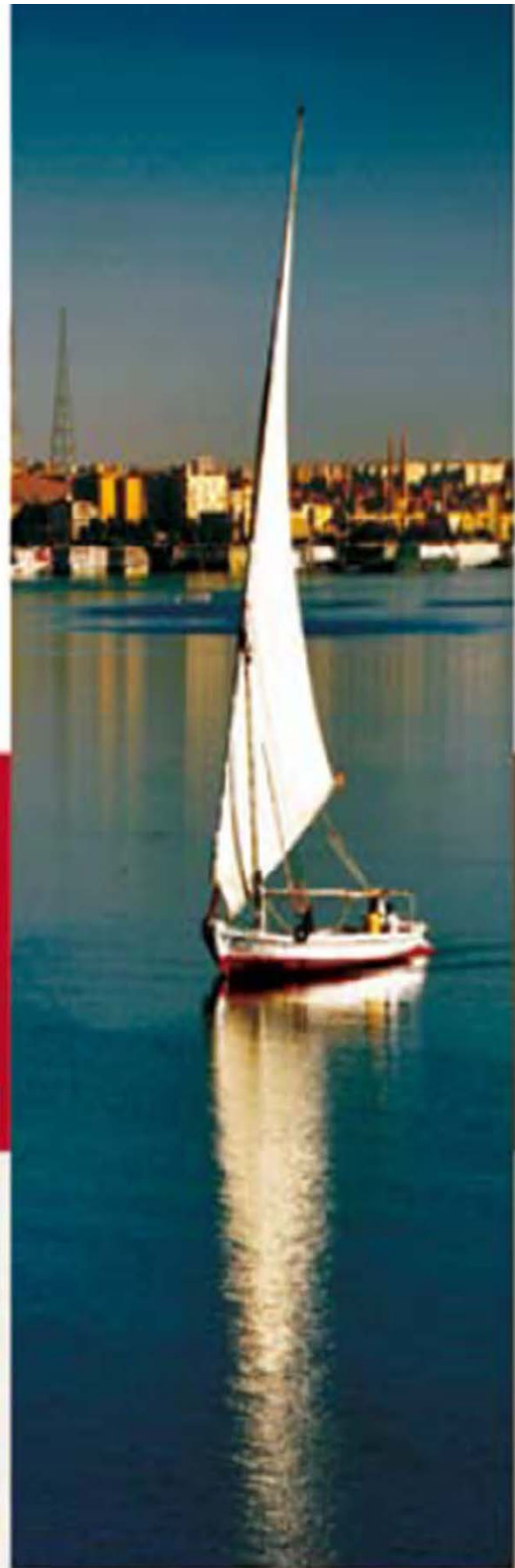
الإتحاد العربي للأسمدة
Arab Fertilizer Association
Since 1975

AFA INTERNATIONAL WORKSHOP ON

FITNESS FOR SERVICE IN CHEMICAL INDUSTRIES

November 25-27, 2012
Aswan, Egypt

Papers



ORGANIZED BY

- Arab Fertilizer Association (AFA)
- International Congress on Fracture (ICF)
- Central Metallurgical R&D Institute (CMRDI)
- Egyptian Group of Fracture (EGF)



***International Workshop on:
"Fitness for Service in Chemical Industries"***
25-27 November 2012, Aswan

Program

DAY 1: Sunday: November 25 th, 2012

08:00 **Registration**

09:15 **Welcome address :**

- Dr. Shafik Ashkar, AFA Secretary General

09:30 Session I

1. Exploration of the corrosion fatigue of steel in the gigacycle regime for oil industry

Prof. C. Bathias, Paris University, France

2. High temperature degradation and mixed mode fracture in fertilizers plants

Mr. T. Shibazaki, Chiyoda Cooperation, Japan

11:30 Networking Coffee / Tea

12:00 Session II

3. Failure Analysis of Reformer Tubes in fertilizers plants

Dr Baha Zaghoul- Ex-President of Central Metallurgical Research and Development Institute - CAIRO, EGYPT

4. An Overview of Risk-based Management Concepts and Strategies in Chemical Industries

A.M. Abdel-atif, Quality Engineering Test Establishment Government of Canada Ottawa, Canada

Dr. M. Elboudjaini, Canmet MATERIALS, Natural Resources, Canada

14:00 Networking Lunch – Isis Island Hotel

19:00 Gala Diner

DAY 2 Monday: November 26 th, 2012

09:00 Session III

5. Integrated inspection and failure analysis of boilers

Dr. H. Abdel-Aleem, CMRDI, Egypt

6. Potential for repair welding technology based on laser metal deposition for petrochemicals industry

Dr. A. Gumenyuk, The Federal Institute for Materials Research and Testing (BAM), Germany

11:00 Networking Coffee / Tea

11:30 Tour visit

15:00 Networking Lunch – Isis Island Hotel

DAY 3: Tuesday, November 28 th, 2012

09:00 Session IV

7. Different fracture modes in gas and petroleum industry

Prof. A. El-Batahgy, CMRDI, Egypt

8. Materials selection and reliability for aggressive services in the fertilizer industry

Dr. A. Asphahani, University of Akron, Ohio-ASM Materials Education Foundation-USA

9. Repairing of Cracked crank shaft in synthesis gas compressor

Eng. Hassan Mostafa Ahmed, Head of mechanical engineering sector - KIMA - Egypt

11:30 Visit to KIMA Fertilizers Company

***AFA WORKSHOP: FITNESS FOR SERVICE IN CHEMICAL
INDUSTRIES***

Aswan, EGYPT

25 - 27 Nov 2012



**Exploration of the corrosion fatigue of steel in the
gigacycle regime for oil industry**

Prof. C. Bathias

Paris University, France

Exploration of the corrosion fatigue of steel in the gigacycle regime for oil industry

Claude BATHIAS¹ and Thierry PALIN -LUC²

¹) Universite Paris X, LEME, 50 rue de Sevres, 92410 Ville d'Avray, France

²) Arts et Metiers ParisTech, I2M, UMR CNRS, Universite Bordeaux 1,
Esplanade des Arts et Metiers, 33405 Talence Cedex, France

ABSTRACT

The effect of sea water corrosion on the gigacycle fatigue strength of a martensitic-bainitic hot rolled steel used for producing off-shore components for petroleum platforms was studied. Three different environments and conditions: (i) air; (ii) air after pre-corrosion, (iii) air under real time artificial sea water flow (in situ) were considered for testing smooth specimens under fully reversed tension between 10^6 and 10^{10} cycles. A drastic effect of corrosion was observed. For the fatigue life greater than 10^8 cycles, the fatigue strength is reduced by a factor more than 5 compared with non corroded specimens (virgin). Corrosion pits due to pre-corrosion, if any, or pits resulting from corrosion in real time during cyclic loading are the crack initiation sites. The calculation of the mode I stress intensity factor at hemispherical surface defects (pits) combined with the Paris-Hertzberg-Mc Clintock crack growth rate model showed that the fatigue crack initiation regime represents most of the fatigue life in the VHCF regime. Original additional experiments shew physical evidences that the fatigue strength in the gigacycle domain under sea water flow is mainly governed by the corrosion process with a strong coupling between cyclic loading and corrosion.

KEYWORDS

Gigacycle fatigue, corrosion, steel, crack initiation, crack growth

NOMENCLATURE

a	crack length
a_{int}	crack length at initiation
a_0	crack length at the corner of the crack growth curve
b	Burger vector
E	Young modulus
N_{Prop}	number of cycles of the crack propagation period
N_{a_i-a}	number of cycles of the long crack growth period
$N_{a_0-a_i}$	number of cycles of the small crack growth period
$N_{a_{int}-a_0}$	number of cycles of the short crack growth period
R	radius of hemispherical surface defect
U_0	amplitude of the displacement at the extremity of the specimen
w	width of the crack growth specimen
ν	Poisson ratio
ΔK	range of the stress intensity factor
σ_a	stress amplitude

INTRODUCTION

Components for off-shore petroleum platforms, designed for 30 years, are loaded in fatigue in sea water environment in the gigacycle regime (around 10^9 cycles because of the ocean waves 24 hours a day). The aim of this work is to study the gigacycle fatigue strength of the low-alloy steel used for manufacturing such components and the effects on this strength of pre-corrosion and corrosion in sea water environment. Many studies carried out on steel and aluminum alloys in the gigacycle regime have demonstrated that there is not a fatigue limit for such metals beyond 10^7 cycles as was believed in the past [1, 2]. It has been shown that fatigue cracks initiate mainly at surface defects in the short fatigue life regime, but may shift to subsurface in the long life range [3]. Other studies have shown that defects like non-metallic inclusions, pores [4] or pits [5 - 7] are the key factors, which control the fatigue properties of metals in very high cycle fatigue (VHCF). Furthermore, in some works it has

been proven that crack initiation dominates the total fatigue life of specimens in gigacycle fatigue [8, 9]. On the other hand, the influence of static deformation has been studied confirming that both passive and transpassive current densities on stainless steel reach a maximum in the course of growing plastic strain [10]. Other works have investigated the dissolution of chemical products in stainless steel with active, passive and intermediate potentials where it is presumed that dissolution is enhanced during cyclic loading [11]. But the effect of aqueous corrosion on the fatigue strength with regard to crack initiation in the VHCF regime is not very much studied in literature. In this regime the material is loaded in its elastic domain at the macroscopic scale. In this work the effect of sea water corrosion (under free potential) on the VHCF strength will be studied.

After presenting the investigated material and the experimental conditions both for crack initiation tests and crack propagation tests, experimental results are presented and discussed with regard to the SEM observation of the fracture surface. It is shown that a drastic effect of sea water corrosion decreases the fatigue strength of the steel under sea water flow. The assessment of the crack growth helps us to show that crack initiation dominates the total fatigue life in the gigacycle regime. Furthermore, additional experiments allow the authors to show experimental evidences of coupling between corrosion and cyclic loading even under ultrasonic loading frequency.

MATERIAL AND EXPERIMENTAL CONDITIONS

The material studied hereafter is a non-standard hot rolled low alloy steel grade (named R5 according to the International Classification Societies of Off-shore Systems) with a typical fine grain microstructure, composed by tempered martensite and bainite, as shown in Figure 1. Its chemical composition is shown in Table 1. This steel is used after a double quenching in water at 920°C then 880°C and tempering at 650°C with water cooling. After this heat treatment its mechanical properties are: hardness 317 HB, yield strength 970 MPa, UTS=1018 MPa, Young modulus $E=211$ GPa. It has to be noticed that this steel is vacuum degassed with low hydrogen content (1 ppm maximum in the liquid steel after the vacuum treatment). Furthermore, very low non-metallic inclusions are present in this steel (see details in [12]).

Table 1: composition of R5 steel (% weight, Fe balance)

C	Mn	Si	P	S	Cr	Ni	Mo	V	O
0.22	1.22	0.3	0.009	0.003	1.07	1.07	0.5	0.09	12 ppm

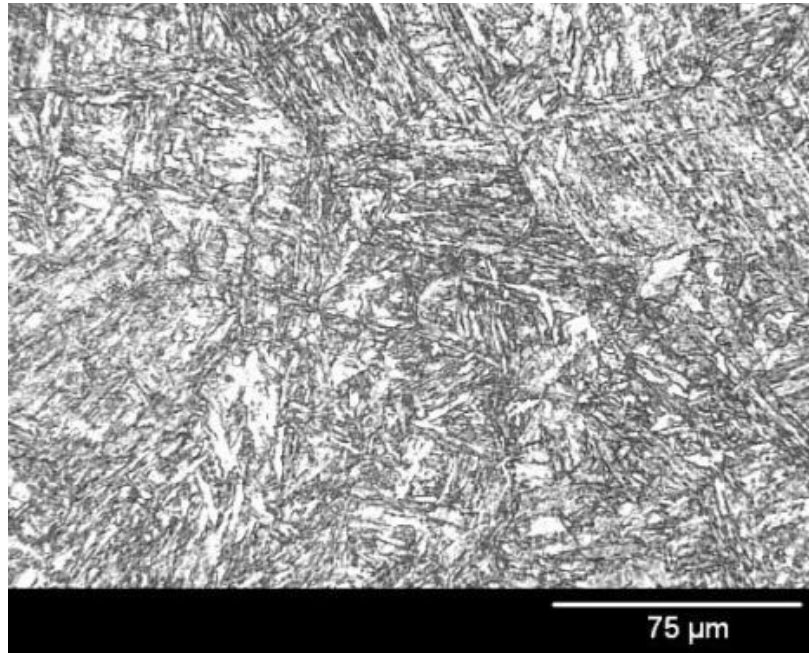


Figure 1: R5 steel microstructure (after Nital etching 2%)

Fatigue test conditions and specimen geometry

Testing machine and specimen geometry

All the fatigue tests (crack initiation and crack growth) presented hereafter were carried out with an ultrasonic fatigue testing machine [1] operating continuously at 20 kHz (no pulse loading) under fully reversed tension ($R = -1$) (see [1, 12] for details). Figure 2 shows the dimensions of the two types of specimens used for (i) VHCF crack initiation tests and (ii) fatigue crack growth (FCG) tests. The geometry of the FCG specimens was designed according to the works of Wu [13] and Sun [14]. The crack growth was measured with an optical binocular microscope with a maximum magnification $\times 200$. The roughness of the tested area of the VHCF specimens was $Ra = 0.6 \mu\text{m}$ and a few additional specimens with a better roughness ($Ra = 0.1 \mu\text{m}$) were tested too for investigating the effect of

roughness. The VHCF specimens were tested under three different conditions: (i) without any corrosion (virgin state), (ii) after pre-corrosion and (iii) under real time artificial sea water flow.

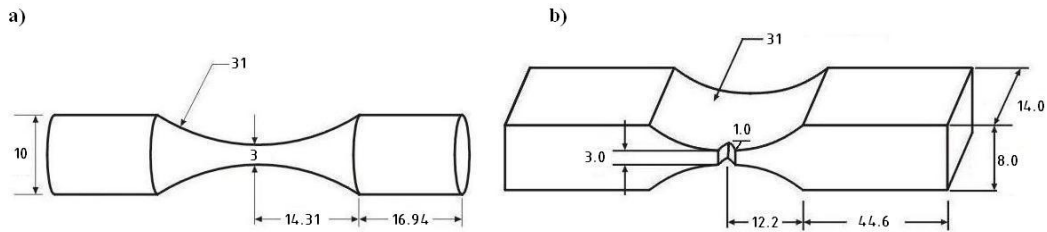


Figure 2 : Specimen geometry for (a) VHCF tests, $K_t=1.02$, (b) crack growth tests (dimensions in mm).

All the VHCF tests were calibrated by using a width band (100 kHz) strain gauge conditioner and a longitudinal strain gauge glued on the specimen surface. Such calibration allows the authors to be certain of the local strain (elastic stress) amplitude and mean value in the narrowest cross section of the specimen. These tests were carried out until a decrease of the resonance frequency of 0.5 kHz that indicates the presence of a macrocrack.

Corrosion of the specimens

The pre-corrosion of the specimens was done according to the ASTM G85 standard: 600 hours in a salt fog corrosion chamber under temperature and humidity control (35°C with 95% of humidity). The salt solution contains 5% of NaCl, its pH was 6.6 and it was applied in the chamber with a rate flow of 1.52 ml/h. After the pre-corrosion process the specimens were first chemically cleaned and then cleaned with emery paper to remove the oxide layer. Many corrosion pits were created by the salt fog (Figure 3) their diameter is about 30 to 80 μm .

To carry out VHCF tests in sea water environment a special corrosion cell was designed (see [12] for details). To avoid any cavitation it was decided to test the specimens under sea water flow (without immersion). This is representative of the splash zone of the mooring chains. To do that a peristaltic pump creates a flow of sea water (100 ml/min) on two opposite sides of the specimen surface in the

tested area (diameter 3 mm). The sea water used was the A3 standard synthetic sea water; its chemical composition in % weight is: 24.53% NaCl, 5.2% MgCl, 4.09% Na₂SO₄, 1.16% Ca₂Cl, 0.695% CaCl and 0.201% NaHCO₃. The pH of this solution is 6.6 and no electrical potential was applied between the corrosion solution and the specimens. The temperature of the sea water was 20 – 25°C (room temperature).

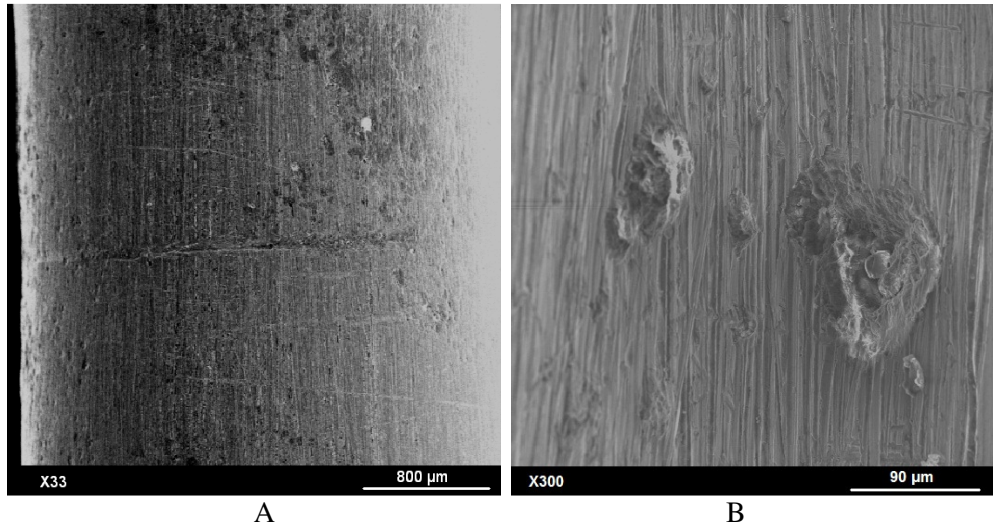


Figure 3: A) Surface of a specimen after pre-corrosion in the salt fog chamber, B) zoom on a corrosion pit.

Fatigue crack growth tests

Fatigue crack growth tests were carried out under fully reversed tension ($R=-1$) in mode I following a similar methodology than prescribed in ASTM E647 standard. Since with the ultrasonic fatigue testing device the specimen was loaded under displacement control, the range of the stress intensity factor ΔK was computed according to references [13, 14]:

$$\Delta K = U_o \left(\frac{E}{1-\nu^2} \right) \sqrt{\frac{\pi}{a}} Y(a/w) \quad (1)$$

with $Y(a/w) = 0.635(a/w) + 1.731(a/w)^2 - 3.979(a/w)^3 + 1.963(a/w)^4$.

U_0 is the displacement amplitude imposed at the top of the specimen by the horn, E is the dynamic modulus and ν is the Poisson ratio of the material, $Y(a/w)$ is a function depending on the specimen geometry, a is the crack length and w is the width of the specimen:

EXPERIMENTAL RESULTS AND DISCUSSION

Fatigue crack initiation tests

Figure 4 shows the S-N curves of the crack initiation tests. A decreasing of around 50 MPa of the fatigue strength for the specimens with pre-corrosion is observed compared to the specimens without any corrosion. The scatter of the fatigue strength of pre-corroded specimens is larger than for virgin ones. There is a drastic effect of sea water flow on the fatigue strength of the R5 steel in the VHCF fatigue regime. Indeed, for the specimens tested under sea water flow, the fatigue strength at 10^7 cycles is around 300 MPa, not far from the value for pre-corroded specimens (360 MPa), but for 3×10^8 cycles the fatigue strength is around 100 MPa only.

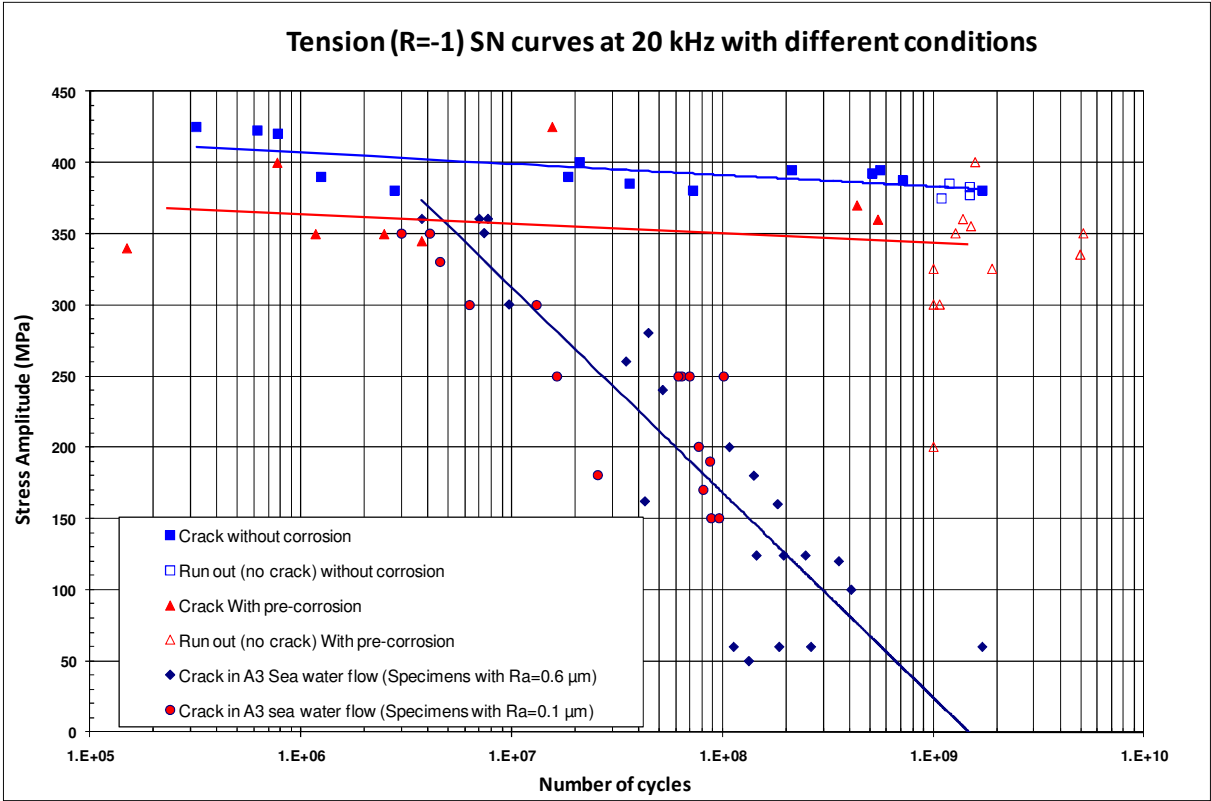
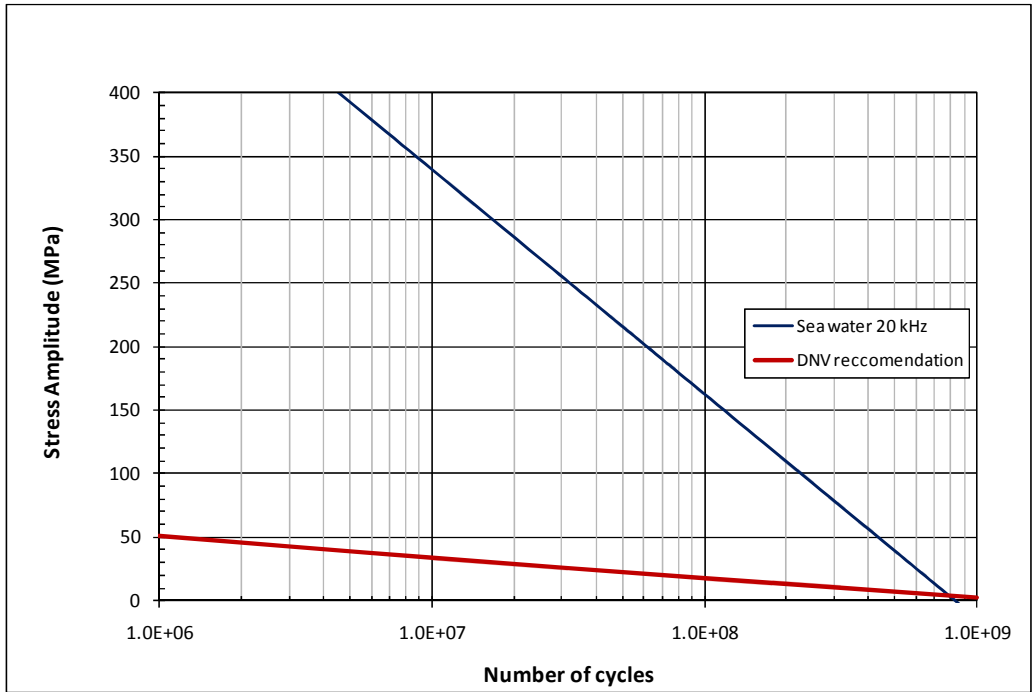


Figure 4: S-N curves of the R5 steel under fully reversed tension at 20 kHz.

The fatigue tests were carried out at 20 kHz under corrosive environment and may be seen first as non representative experiments because of the high loading frequency compared with the characteristic time of the corrosion process. But a comparison between our experimental data and the recommendations provided by the International Classification Societies of Off-shore Systems is illustrated Figure 5 for the investigated steel. This shows that the ultrasonic fatigue tests results of this study are in good agreement with such recommendations in the gigacycle regime. Furthermore the competition between cyclic loading and corrosion is discussed later in this paper.



DNV SN Curve approved for R4 and R5 steel (R=0.1)

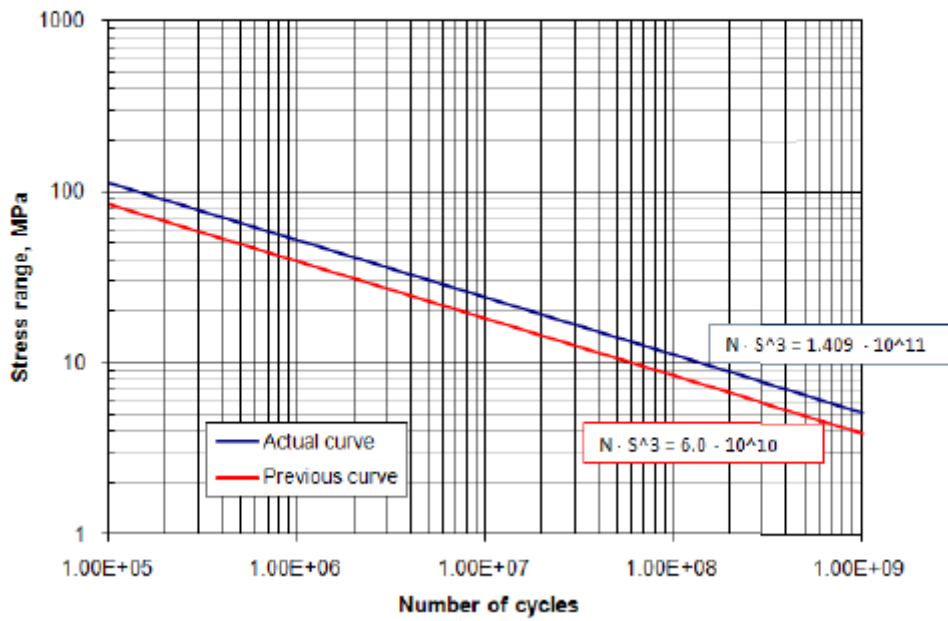


Figure 5: Comparison of the experimental SN curve on smooth specimens under fully reversed tension under A3 sea water flow for R5 steel and DVN recommendation

SEM observation of the fracture surfaces

On virgin specimens, even if some unusual internal crack initiations were observed (Figure 6), most of the fatigue cracks initiated at the specimen surface over the cycle range ($10^6 - 10^9$ cycles). Surface defects were the origin of the cracks for non-corroded specimens and corrosion pits for both pre-corroded specimens and specimens tested under sea water flow (Figures 7 – 8). For the specimens tested under sea water flow the crack initiated all around the specimen surface due to several large corrosion pits. The size of the pits depends on the time (i.e. the number of cycles); their diameter is smaller on the pre-corroded specimens (30 to 80 μm) than under sea water flow (50 to 300 μm) (Figures 7 and 8). Furthermore, a lot of small cracks, perpendicular to the loading direction (mode I), were observed at the surface of the specimen tested under sea water flow (Figure 8C); whereas such small cracks were not observed on both virgin and pre-corroded specimens. This is characteristic of a corrosion/cyclic loading interaction.

Since a significant decrease of the fatigue strength has been observed due to corrosion pits (seen as geometrical defects), it is important to determine if the crack propagation dominates or not the total fatigue life compared with the crack initiation phase.

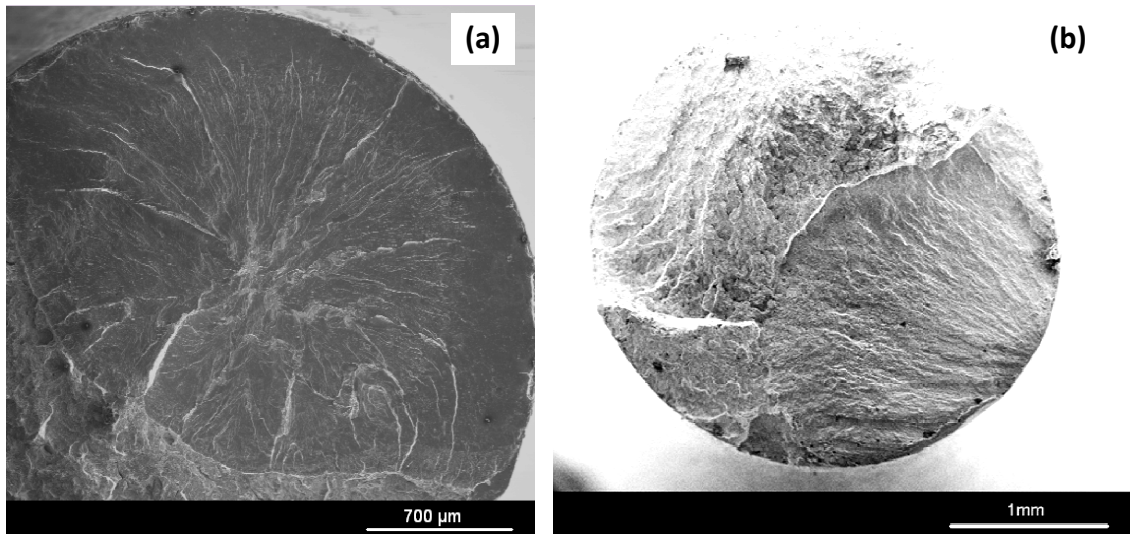


Figure 6: Fracture surface of R5 steel virgin specimens (a) Internal crack initiation $\sigma_a = 380$ MPa, $N = 2.78 \times 10^6$ cycles, (b) surface crack initiation $\sigma_a = 395$ MPa, $N_f = 5.61 \times 10^8$ cycles.

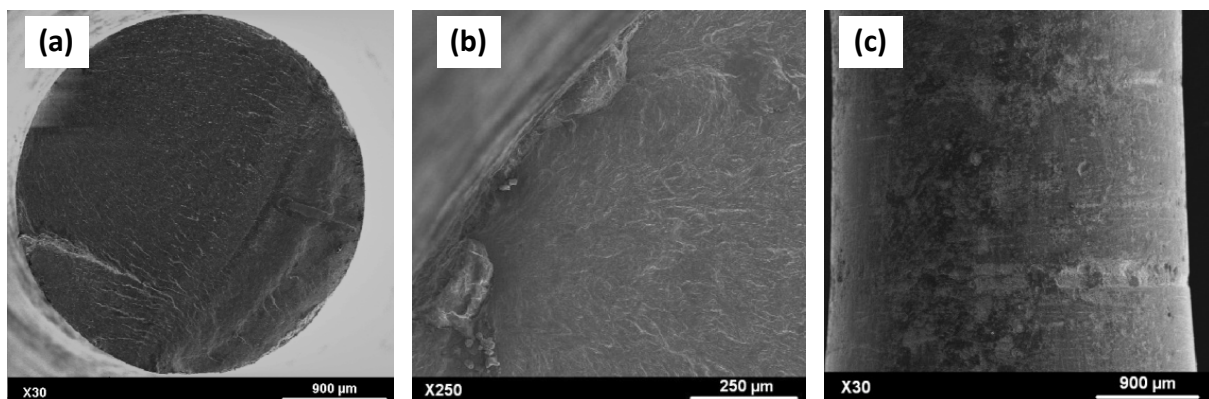


Figure 7: Specimen with pre-corrosion, $\sigma_a = 370$ MPa, $N_f = 4.37 \times 10^8$ cycles

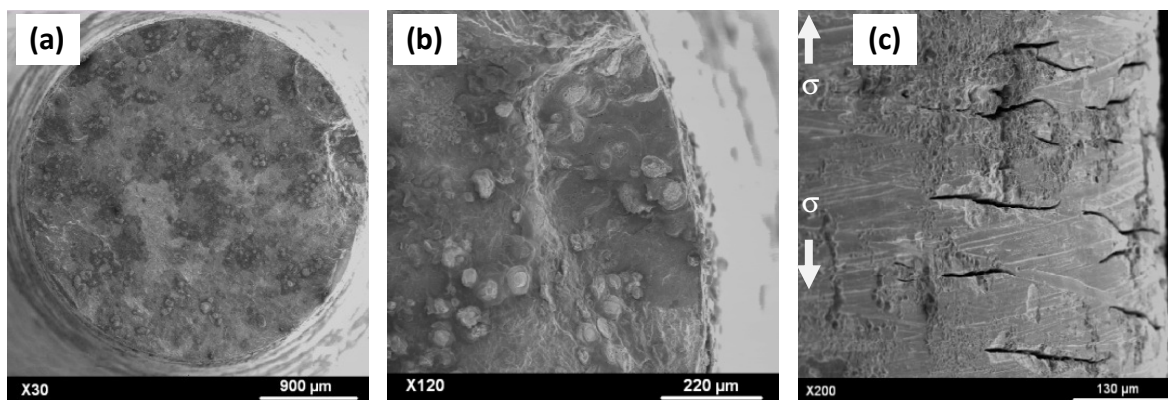


Figure 8: Specimen tested under sea water flow, $\sigma_a = 160$ MPa, $N_f = 1.8 \times 10^8$ cycles.

Assessment of the crack initiation and propagation duration

The experimental $da/dN = f(\Delta K)$ curve for the investigated steel is shown in Figure 9. This shows that in air the mode I ($R = -1$) stress intensity threshold for R5 steel is around $3.3 \text{ MPa}\sqrt{\text{m}}$ and as usual the crack growth rate is faster under sea water flow than in air [15]. The fatigue crack propagation duration was assessed according to the work of Paris et al. [8, 9], based on the Paris-Hertzberg-McClintock crack growth model $\frac{da}{dN} = b \left(\frac{\Delta K_{\text{eff}}}{E\sqrt{b}} \right)^3$ and $\left(\frac{\Delta K_{\text{eff}}}{E\sqrt{b}} \right) = 1$ at the corner, where E is the elastic modulus and b is the Burger's vector. The good agreement of this equation with our experimental data and $b = 0.285 \text{ nm}$ was shown in [12]. Since in our experiments at 20 kHz the measurement of K_{op} is not possible, in first approximation $\Delta K_{\text{eff}} \approx K_{\text{max}}$ was assumed and no water interaction with the stress intensity factor was considered.

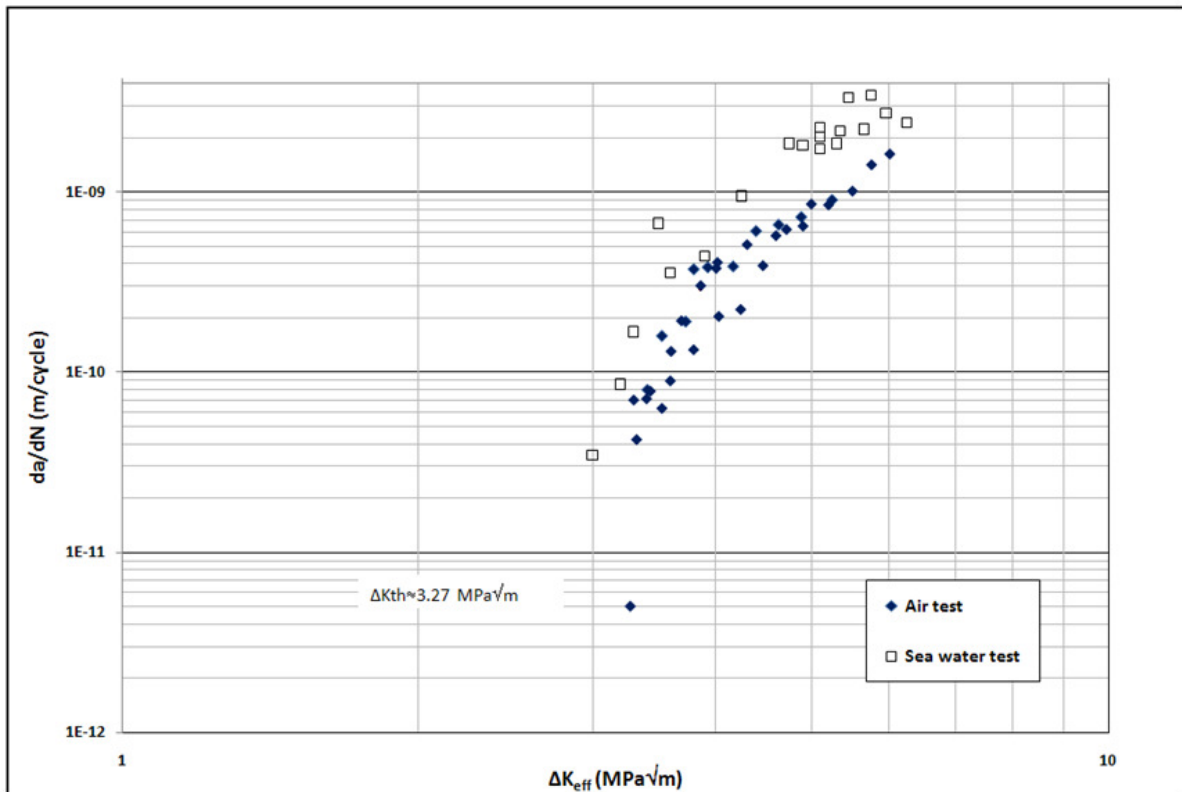


Figure 9: $da/dN = f(\Delta K)$ curve in mode I for the R5 steel ($R = -1$), in air and under sea water flow at room temperature.

To assess the crack propagation phase, a corrosion pit was modeled by a hemispherical surface defect with radius R . The existence of these hemispherical pits was observed by scanning electron microscopy on the surface of different specimens of R5 steel with pre-corrosion in salt fog chamber (Figure 3) and with corrosion in A3 sea water flow (Figure 8). The longitudinal cross section of a pre-corroded specimen (after 4.37×10^8 cycles under a stress amplitude of 370 MPa) close to the fracture surface was observed as illustrated in Figure 10A. This shows a short crack initiated at a corrosion pit. Based on this observation, an initial fatigue crack of depth a_{int} emanating from the surface of the hemispherical pit and perpendicular to the loading direction due to intercrystalline corrosion cracking was assumed. The length of the initial short crack emanating from hemispherical defects was assumed to be $a_{int} = 10 \mu\text{m}$.

$$A(v) = 1.683 + \frac{3.336}{7-5v}, B(v) = -1.025 - \frac{12.3}{7-5v}, C(v) = -1.089 + \frac{14.5}{7-5v}, D(v) = 1.068 - \frac{5.568}{7-5v}$$

It was assumed that the propagation of the fatigue crack is divided in three stages: (i) a short crack propagation during $N_{a_{int}-a_0}$ cycles, from initiation a_{int} to the crack size a_0 , then (ii) a small crack propagation period $N_{a_0-a_i}$ cycles, from a_0 to the crack size a_i , and (iii) a long crack propagation N_{a_i-a} cycles, from a_i to the final crack size a : $N_{Total} = N_{a_{int}-a_0} + N_{a_0-a_i} + N_{a_i-a}$. With these three different regimes the very quick propagation of short crack and the quick propagation of small crack compared to long crack were considered.

With these three different regimes [12] the very quick propagation of short crack and the quick propagation of small crack compared to long crack were considered. The detailed equations are given in [12], they were applied to our data assuming that the initial crack has a length, a_0 , corresponding to the corner: $da/dN=b$.

Case 1: $a_0=9.32 \mu\text{m}$, $\sigma_a=360 \text{ MPa}$, $R=48 \mu\text{m}$, $a= 2.4 \text{ mm}$, $N_{exp}=5.5 \times 10^8$ cycles on a pre-corroded specimen					
α	a_{int}/a_0	$N_{a_{int}-a_0}$	$N_{a_0-a_i}$	N_{a_i-a}	N_{Total} (cycles)
100	0.9	115,801	44,151	4,507,080	4,667,032
	0.94	13,163			4,564,394
	0.97	2,300			4,553,531
Case 2: $a_0=41.5 \mu\text{m}$, $\sigma_a=160 \text{ MPa}$, $R=300 \mu\text{m}$, $a= 2.6 \text{ mm}$, $N_{exp}=1.83 \times 10^8$ cycles on specimen tested under sea water flow					
α	a_{int}/a_0	$N_{a_{int}-a_0}$	$N_{a_0-a_i}$	N_{a_i-a}	N_{Total} (cycles)
100	0.9	515,466	168,014	10,258,700	10,942,180
	0.94	58,593			10,485,307
	0.97	10,237			10,436,951

Table 2: Hemispherical surface crack growth vs. experimental fatigue life, for $x=3$, and different a_{int}/a_0 ratios.

Two cases are shown in Table 2 with two experimental total fatigue lives N_{exp} ; several additional cases are detailed in [12]. In the first case 99.1% of the fatigue life is due to initiation. For the second case, 94% of the fatigue life was consumed by the initiation phase. Furthermore, it has been shown in [12] that with a high value of α and large a_{int}/a_0 one obtains similar N_{Total} results than with a low α and small a_{int}/a_0 , that is because with a higher α the crack does not grow as far due to the slope of the

da/dN curve in the threshold region, then a_{in}/a_0 must be larger, and with a lower α , a_{in}/a_0 must be smaller.

This calculations show that crack initiation dominates the fatigue life. Even if our calculations were carried out by using the crack growth curve in air, the conclusion is still valid because the crack growth rate for the R5 steel under sea water flow is higher than in air as shown Figure 9 and usually reported in literature [15]. Since the fatigue life is dominated by the crack initiation regime even in corrosive environment, additional experiments have been carried out to try to understand why this initiation period is significantly affected by sea water flow.

Additional experiments and discussion about the coupling between cyclic loading and corrosion

To complete these tests an ultrasonic fatigue test has been carried out on a cylindrical specimen. Since during an ultrasonic fatigue test a stationary wave is applied on the specimen, all along this cylinder different stress amplitudes are applied [17]. Figure 11B shows the distribution of the stress amplitude along the cylindrical specimen loaded in its central part with a stress amplitude of 120 MPa (highest value along the specimen). This corresponds to a mean fatigue life of 2×10^8 cycles. For observation, the specimen surface was divided in 13 zones of around 1 cm long, each one was loaded to a specific stress amplitude interval. By testing such a cylinder under sea water flow (Figure 11A), observation of the damaged areas allowed us to investigate the link between the stress amplitude and the damage due to the in-situ fatigue – corrosion process. The specimen failed after 7.37×10^7 cycles.

Microscopic observations of the cylinder surface showed that R5 steel was damaged by fatigue – corrosion in the areas where the stress amplitude was higher than 56 MPa, a few corrosion traces only were observed where the stress amplitude was smaller (Figure 11D). The final fracture occurred where the stress amplitude was between 112 and 120 MPa. This shows an experimental evidence of the coupling between the corrosion process and cyclic loading, even at ultrasonic frequency (20 kHz),

since below 56 MPa without any sea water flow there is no failure after 2×10^8 cycles (see the SN curves Figure 4).

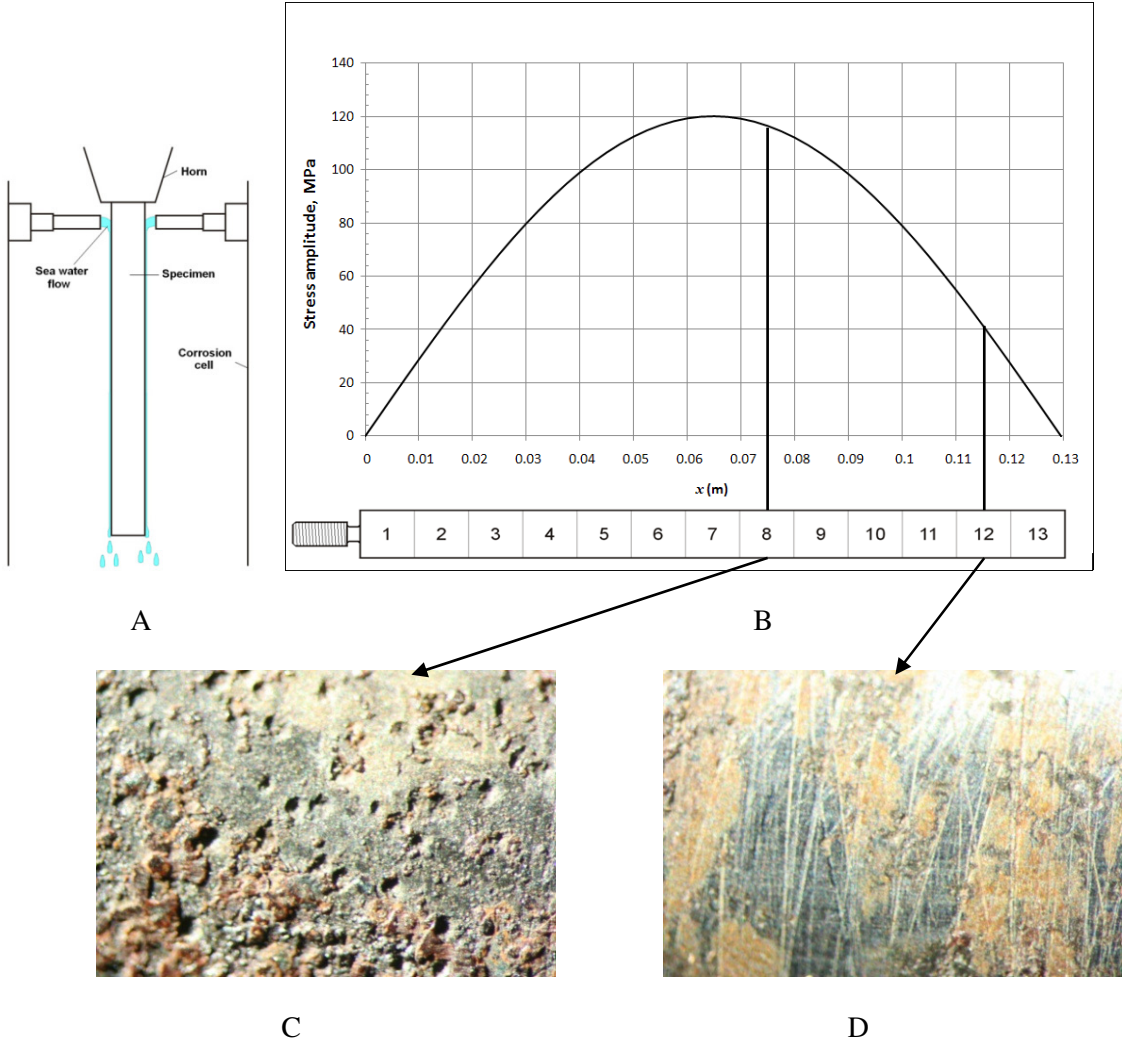


Figure 11: A) schematic illustration of the test principle of a cylindrical specimen with constant cross section under sea water flow, B) evolution of the stress amplitude along the longitudinal axis of the cylindrical specimen for a stress amplitude of 120 MPa in the central cross section, C) and D) optical picture of the specimen surface after 7.37×10^7 cycles in area 8 and area 12 loaded at different stress amplitudes.

Futhermore, three additional tests were carried out on VHCF specimens under the same conditions than all the other tests but, without any cyclic loading. Only the sea water flow was applied on the

specimen surface with the same flow rate than for the tests with cyclic loading. The aim of these tests was to quantify the corrosion damage after the same duration than 10^7 cycles (8mn20s at 20 kHz), 10^8 cycles (1h23mn20s at 20 kHz) and 10^9 cycles (13h53mn20s at 20 kHz). No corrosion trace was observed by SEM after 8mn20s. After 1h23mn20s only a few traces of corrosion appear but not pits were observed. Corrosion pits were observed at the specimen surface after 13h53mn20s. The typical size of these pits was varying between 30 and 60 μm (Figure 12) this is significantly smaller than under simultaneous cyclic loading and sea water flow (Figure 8). The same pit size was observed under sea water flow with a stress amplitude of 240 MPa after 5×10^7 cycles. This corresponds to 42 mn only at 20 KHz! This proves that there is a coupling between corrosion and cyclic loading.

Because of such coupling, the question of the roughness effect occurred. Complementary fatigue tests were carried out under sea water flow at a stress amplitude of 250 MPa on the same VHCF specimens but with a polished surface ($Ra=0.1 \mu\text{m}$) to investigate a possible roughness effect. There was no evidence of the surface roughness effect under sea water flow (Figure 4): the fatigue life is in the scatter band of other experimental data (with $Ra=0.6 \mu\text{m}$).

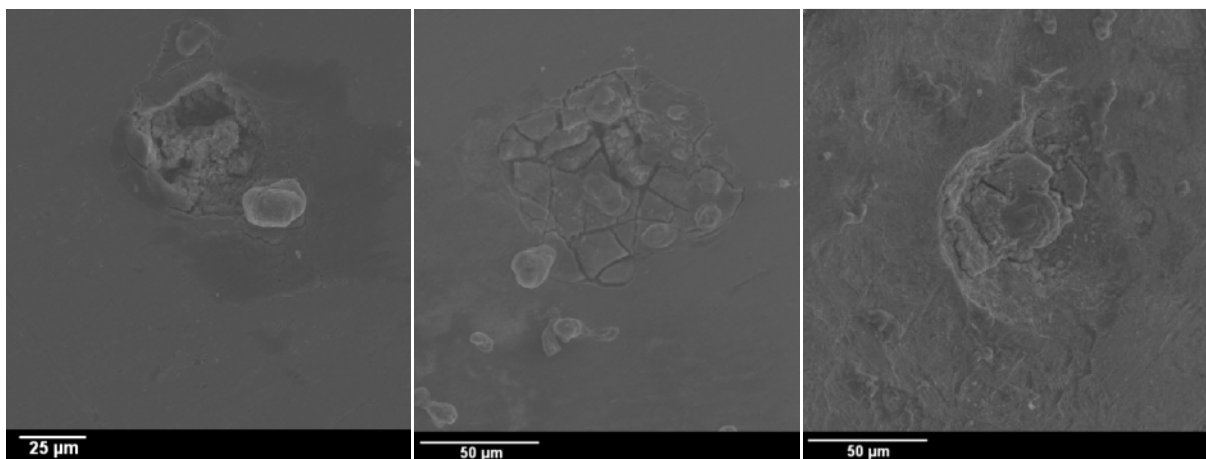


Figure 12: corrosion pits at the surface of a specimen under sea water flow during 13 h 53 min 20 s without any cyclic loading.

This work shows experimental evidence of the coupling between corrosion and cyclic stress, even at 20 kHz while some authors think that fatigue corrosion interaction is not active when the loading frequency is high because of the long characteristic time of the corrosion process compared with the loading period. The observations of this study tend to show that the number of loading cycles (not the time) is a key factor in the fatigue crack initiation phenomenon under sea water flow. Further investigations should be carried out to understand the physical phenomenon involved in the fatigue damage process assisted by corrosion. One may imagine ultrasonic fatigue tests with potentiostatic measurements to monitor corrosion current and potential evolution during a fatigue test. However, not immersed experiments (to avoid cavitation) is a big experimental difficulty for carrying such tests. Investigation of the corrosion pitting kinetics under cyclic loading is probably a key factor for a better understanding of fatigue corrosion process. In situ micro-tomography under both ultrasonic cyclic loading and sea water corrosion may an interesting way for future researches.

CONCLUSION AND PROSPECTS

Very high cycle fatigue tests were carried out up to 10^9 cycles on smooth specimens in hot rolled martensitic-bainitic steel under three different conditions (i) virgin specimens, (ii) pre-corroded specimens and (iii) under artificial sea water flow during the fatigue test. The fatigue strength at 10^8 cycles is significantly reduced by a factor of 74% compared to the virgin specimens and of 71% compared to the pre-corroded ones. The poor corrosion – fatigue strength is related to the size of the pits. The assessment of the crack growth shows that crack initiation dominates the total fatigue life when $N > 10^7$ cycles. A strong coupling between environment and cyclic loading has been proved. Under cyclic loading, even at ultrasonic frequency, fatigue damage and corrosion pitting are interacting for creating crack initiation at very low stress amplitude where no fatigue crack initiates under fatigue loading alone. This has to be more investigated for understanding the physical mechanisms involved in the corrosion fatigue. Anyway, it has been shown that ultrasonic fatigue test immersed in flowing sea water is a good experimental way to investigate very long life of steel under corrosion conditions with reasonable test time duration.

REFERENCES

- [1] C. Bathias and P.C. Paris (2005) *Gigacycle Fatigue in Mechanical Practice*, Marcel Dekker Publisher Co., New York USA.
- [2] I. Marines, X. Bin and C. Bathias (2003) An Understanding of very high cycle fatigue of metals, *Int J Fatigue* **25**, 1101-1107.
- [3] J.H. Zuo, Z. Wang and H. Han (2008) Effect of microstructure on ultra-high cycle fatigue behavior of Ti-6Al-4V, *Mat Sci Eng A* **473**, 147-152.
- [4] H.R. Ammar, A.M. Samuel and F.H. Samuel (2008) Effect of casting imperfections on the fatigue life of 319-F and A356-T6 Al-Si alloys, *Mat Sci Eng A* **473**, 65-75.
- [5] H.T. Pang and P.A.S. Reed (2007) Microstructure effects on high temperature fatigue crack initiation and short crack growth in turbine disc nickel-base superalloy Udimet 720 Li, *Mater Sci Eng A* **448**, 67-69.
- [6] R.A. Yeske and L.D. Roth (1982) Environmental effects on fatigue of stainless steel at very high frequencies, In: Wells (Westinghouse) J.M. Buck, Roth, Tien (Eds), *Ultrasonic fatigue*, The Metallurgical Society of AIME, New York, USA, pp. 365–385.
- [7] R. Ebara and Y. Yamada (1982) Corrosion fatigue behaviour of 13Cr stainless steel and Ti-6Al-4V at ultrasonic frequency, In: Wells (Westinghouse) J.M. Buck, Roth, Tien (Eds), *Ultrasonic fatigue*, The Metallurgical Society of AIME, New York, USA, pp. 349–364.
- [8] P.C. Paris (2004) The relationship of effective stress intensity, elastic modulus and Burgers-vector on fatigue crack growth as associated with “fish-eye” gigacycle fatigue phenomena, In : *Proceedings of VHCF-3*, Kyoto, Japan, 2004, pp. 1-13.
- [9] I. Marines, P.C. Paris, H. Tada and C. Bathias, (2007) Fatigue crack growth from small to long cracks in VHCF with surface initiations, *Int J Fat* **29**, 2072-2078.
- [10] E.M. Gutman and G. Soloviof (1996) The mechanochemical behavior of type 316L stainless steel, *Corrosion Science*, **38**, 1141–1145.

- [11] T. Pyle, V. Rollins and D. Howard (1975) The influence of cyclic plastic strain on the transient dissolution behavior of 18/8 stainless steel in 3.7M H₂SO₄, *J. Electrochem. Soc.*, **122**, 1445–1453.
- [12] T. Palin-Luc, R. Perez-Mora, C. Bathias, G. Dominguez, P.C. Paris and J.L. Arana (2010) Fatigue crack initiation and growth on a steel in the very high cycle fatigue regime with sea water corrosion, *Eng. Fract. Mech.*, **77**, 1953-1962.
- [13] T.Y. Wu and C. Bathias (1994) Application of fracture mechanics concepts in ultrasonic fatigue, *Eng Fract Mech*, **47**, 683-690.
- [14] Sun (2000) Etude du seuil de fissuration à haute fréquence en fatigue et en fretting fatigue. Ph.D. Thesis, CNAM, Paris France.
- [15] C. Bathias and A. Pineau (2010) Fatigue of materials and structures, ISTE Ltd and John Wiley & Sons Inc., 512 p.
- [16] P.C. Paris, T. Palin-Luc, H. Tada and N. Saintier (2009) Stresses and crack tip stress intensity factors around spherical and cylindrical voids and inclusions of different elastic properties and with misfit sizes, In Proceedings Int. Crack Path, 8 pages.
- [17] S. Stanzl-Tschegg, H. Mughrabi, and B. Schoenbauer (2007) Life time and cyclic slip of copper in the VHCF regime, *Int J Fatigue*, **29**, 2050-2059.

Corresponding author: thierry.palin-luc@ensam.eu

List of Tables

Table 1: composition of R5 steel (% weight, Fe balance)

Table 2: Hemispherical surface crack growth vs. experimental fatigue life, for $x=3$, and different a_{in}/a_0 ratios.

List of Figures

Figure 1: R5 steel microstructure (after Nital etching 2%)

Figure 2 : Specimen geometry for (a) VHCF tests, $K_t=1.02$, (b) crack growth tests (dimensions in mm).

Figure 3: A) Surface of a specimen after pre-corrosion in the salt fog chamber, B) zoom on a corrosion pit.

Figure 4: S-N curves of the R5 steel under fully reversed tension at 20 kHz.

Figure 5: Comparison of the experimental SN curve on smooth specimens under fully reversed tension under A3 sea water flow for R5 steel and DVN recommendation

Figure 6: Fracture surface of R5 steel virgin specimens (a) Internal crack initiation $\sigma_a=380$ MPa, $N_f=2.78 \times 10^6$ cycles, (b) surface crack initiation $\sigma_a=395$ MPa, $N_f=5.61 \times 10^8$ cycles.

Figure 7: Specimen with pre-corrosion, $\sigma_a=370$ MPa, $N_f=4.37 \times 10^8$ cycles

Figure 8: Specimen tested under sea water flow, $\sigma_a=160$ MPa, $N_f=1.8 \times 10^8$ cycles.

Figure 9: $da/dN = f(\Delta K)$ curve in mode I for the R5 steel ($R = -1$), in air and under sea water flow at room temperature.

Figure 10: longitudinal cross section of a specimen showing A) a fatigue crack initiation at a corrosion pit, B) the old austenitic grains are yellow highlighted, C) illustration of the short fatigue crack and the grain boundaries.

Figure 11: A) schematic illustration of the test principle of a cylindrical specimen with constant cross section under sea water flow, B) evolution of the stress amplitude along the longitudinal axis of the cylindrical specimen for a stress amplitude of 120 MPa in the central cross section, C) and D) optical picture of the specimen surface after 7.37×10^7 cycles in area 8 and area 12 loaded at different stress amplitudes.

Figure 12: corrosion pits at the surface of a specimen under sea water flow during 13 h 53 min 20 s without any cyclic loading.

***AFA WORKSHOP: FITNESS FOR SERVICE IN CHEMICAL
INDUSTRIES***

Aswan, EGYPT

25 - 27 Nov 2012

**High temperature degradation and mixed mode
fracture in fertilizers plants**

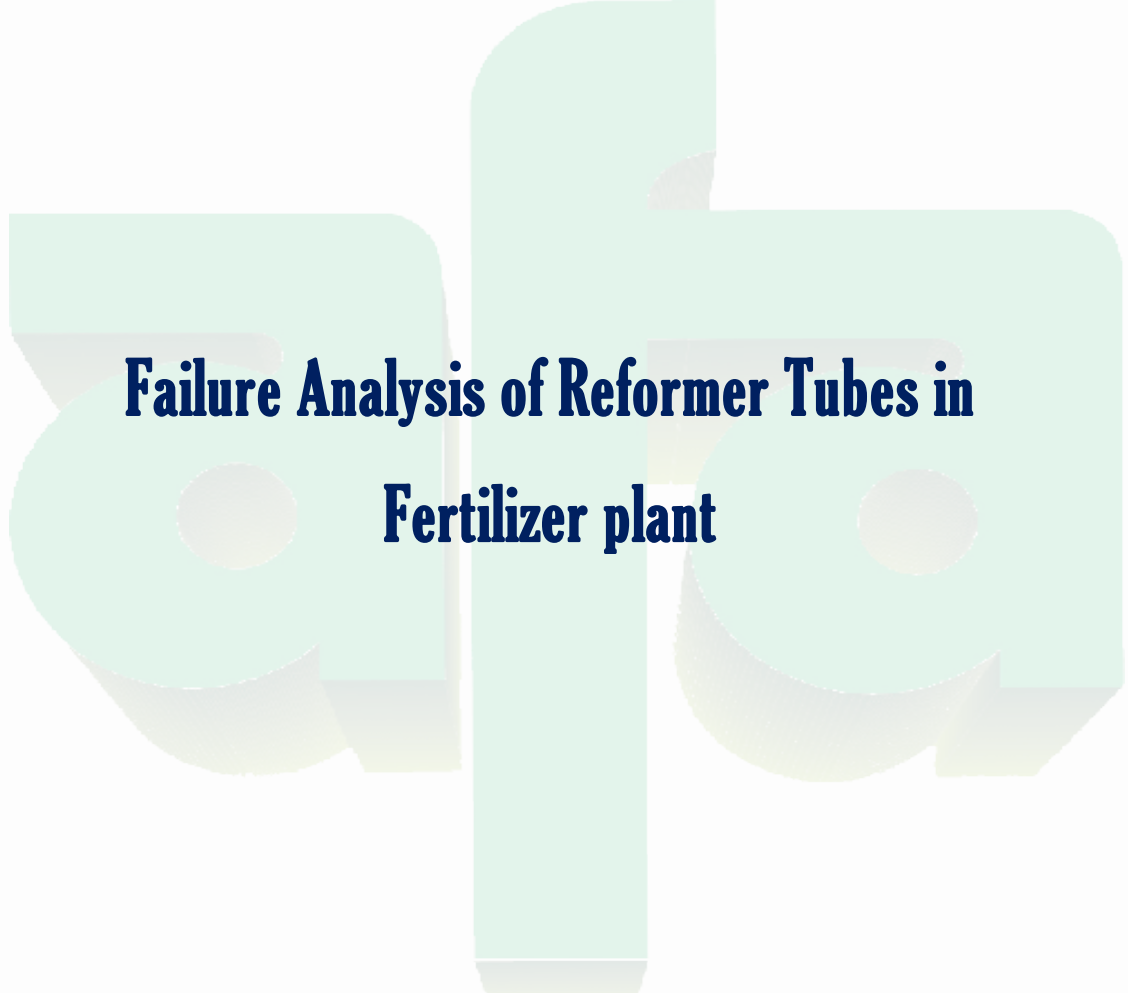
Mr. T. Shibazaki

Chiyoda Cooperation, Japan

***AFA WORKSHOP: FITNESS FOR SERVICE IN CHEMICAL
INDUSTRIES***

Aswan, EGYPT

25 - 27 Nov 2012



**Failure Analysis of Reformer Tubes in
Fertilizer plant**

Dr. B. Zaghloul

Central Metallurgical R& D Institute (CMRDI), Egypt

Failure Analysis of Reformer Tubes in fertilizer plant

*** B. M. Zaghoul* and H. A. Abdel-Aleem**

* Central Metallurgical R& D Institute (CMRDI), Manufacturing Technology
Dept. P.O.Box 87 Helwan, Egypt, bahaazaghoul@hotmail.com

General Introduction

The Kellogg design catalytic steam reformer at SEMADCO company started operation in 1994. The radiant section of the furnace contains two banks of reforming tubes (A & B). Each bank or row contains 36 tubes for a total of 72 composed of centrifugally cast Manoir 36x alloy with design tube wall temperature of 935°C. The tubes are vertically mounted with the flow entering in the top and exiting at the bottom. Each tube has a 109.8 mm. ID and 9.3 mm. wall thickness. Figure 1 shows the arrangement of a typical small or medium sized furnace with the reformer columns, which contain the catalyst, arranged in the form of two vertical walls. Most modern furnaces are of the top-fired type with burners disposed in rows on both sides of the tubes, while older furnaces may be of the side-fired type with burners distributed in two or more layers. The tubes receive the charge through the inlet pigtailed of Cr–Mo low alloy steel above the roof of the radiation chamber. The pigtailed have a shape that provides flexibility to accommodate the axial displacement of the horizontal inlet manifold and of the vertical tubes produced by thermal expansion.

The tubes are suspended through the use of counterweights or hangers. Depending on the design, a fraction of the weight of the tubes is transmitted to the furnace structure at their lower ends. The reaction gas leaves the columns through the outlet pigtailed, connecting to the outlet manifold. The outlet pigtailed provide flexibility to compensate for their thermal expansion and the thermal expansion in the horizontal outlet manifold. From the outlet manifold, the reaction gas flows through a transition piece to the recovery boiler, where it is cooled, producing saturated steam. The temperature of the charge in the inlet manifold is between 420 and 550°C. This is the wall temperature of the column segment in the furnace roof. The temperature of the reaction gas in the tubes below the floor of the furnace is between 800 and 900°C. The wall temperature of the tubes depends on several factors. One is the burner regulation, which may deviate with time. There is a loss of activity of the catalyst during its life cycle and, to compensate for this effect, the wall temperature may be increased. As the catalyst ages, there is a trend

to form a preferred path for gas flow through the catalyst bed. Thus, cooling is not uniform over the tube cross section, and hotter (and brighter) areas appear on its external surface in the form of a giraffe neck pattern, as

observed through the furnace windows. There are cases of increased severity where the hotter zones have a ring like shape known as a tiger tail. These aspects are noted to call attention to the diversity and complexity of the variables that affect the tube wall temperature. It is virtually impossible to foresee the tube wall temperature in the radiation chamber with reasonable precision based on design models. Figure 2 illustrates the temperature distribution in the radiation zone for several furnaces based on metallographic observations, the methodology of which is outlined below. It is apparent that there is a consistent trend towards the production of a maximum wall temperature in the lower half of the radiation chamber during service. In several cases this is estimated to be greater than 1000°C. Field experience shows that skin temperature measurements based on thermography are in error as they indicate maximum readings more in the direction of the burners. The design is for a nominal life of 100 000 h (11.4 years) on the basis of API Recommended Practice 530. The length of a normal campaign for a reformer furnace may vary from 12 to 36 months (8 760 to 26 300 h). However, the useful service life is found to range from around 30 000 to 150 000 h, depending on the actual operating conditions and the characteristics of the particular material. The most critical components of a reformer furnace are the tubes. It is expensive and difficult to replace or repair these, whereas other components can be repaired or replaced more easily. Because of the extreme temperature conditions, highly alloyed steels are required, and as strength is increased, generally ductility and toughness decrease. The alloys used are not easily drawn or extruded, thus cast structures are used. Centrifugal casting is now generally used as the structure is more even and the grains are oriented in a radial direction, providing greater strength and creep resistance. . In order to have long-time strength at high temperature, the austenitic Cr–Ni matrix of these alloys is strengthened through a dispersion of hard deformation-resistant carbide particles. In the as-cast condition there is a network of primary carbides along grain boundaries, lying in a dendritic pattern. When in service at high temperature, a distribution of fine secondary carbides is formed in an interdendritic manner, at the same time the primary carbides dissolve. High temperature strength (resistance to deformation) depends on a distribution of fine, strong, and stable particles. Unfortunately, there is always a tendency for particles to coarsen during high temperature service to minimize surface

energy, and diffusion takes place to facilitate this – the higher the temperature the faster the diffusion occurs. Thus there is a need to stabilize the fine dispersion of particles. The outlet pigtails and manifold require materials whose properties are a compromise between long-term high temperature mechanical strength and good ductility after aging. Alloy 800 (20Cr, 32Ni, 0.05C) is the most commonly used material. The pigtails are made of seamless tube. The outlet manifold may be of seamless pipe or of welded spindle-cast segments.

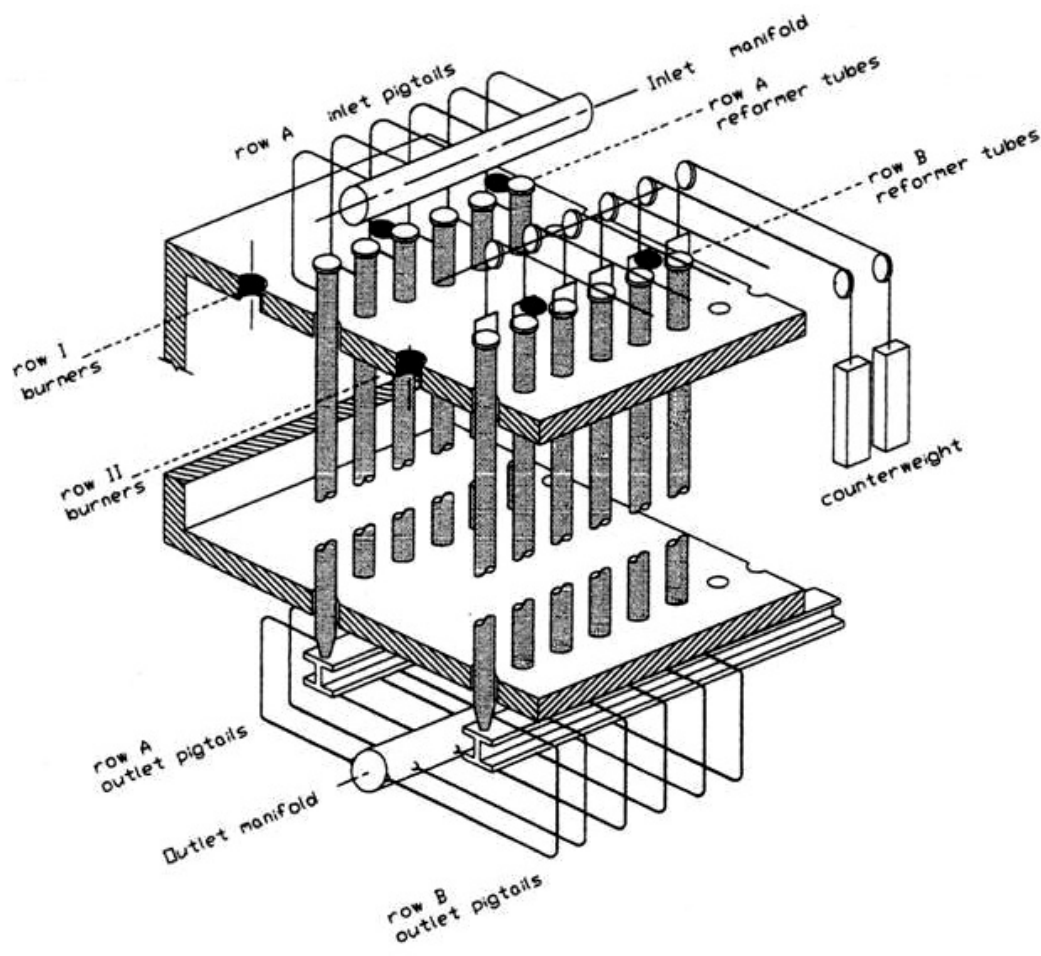


Fig. 1. Schematic view of a top fired reformer furnace

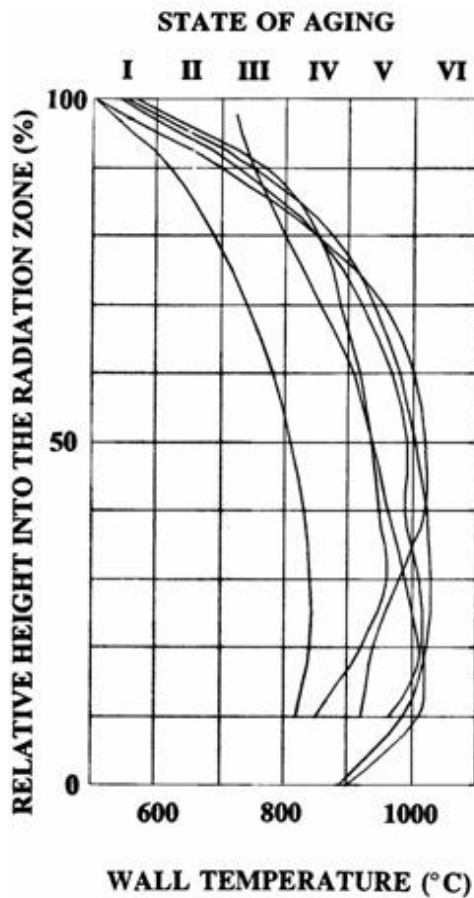


Fig. 2. Temperature distribution in the radiation zone for several reformer furnaces based on metallographic observations

Investigation of the case at SEMADCO

During a turn around time at the end of 2008, it was discovered that about 11 tubes exhibited sever bending inside the furnace with distinguished changes in the color of the outer surfaces as shown in Fig. 3. It was also noticed that there is distinguished differences in the levels of outer pigtails especially at the right side of the same bank where the bended tubes were observed Fig.4

A formal investigation was conducted by CMRDI team in order to investigate the cause of the observed incident. In line insitu evaluation of the tubes inside the fire box revealed that there was 9 tubes had encroached into other tubes as a result of severe bowing. They looked like banana shaped. The maximum bowing was observed at the upper half of the tube

length. In some cases the interval distances between the tubes become very narrow as shown in Fig. 5.

It was reported that severe rupture of one tube occurred several years ago and that tube was replaced with new one. No failure investigation was conducted at that time to understand the cause of the rupture. There is a possibility that the bowing of the tubes occurred due to the high pressure impulse released into the fire box after the initial tube rupture which took place earlier several years ago. The severe rupture damage of that tube which was found near-by the reformer is shown in Fig. 6. It should be noticed that the pressure impulse of the old ruptured tube had caused considerable damage not only inside the fire box, but even on the steel structure of the pass way platform out side the fire box.

Looking at the counter weights at the roof of the fire box, it was observed that all of them were at the same level and no counter balance had taken place during the past operation of the reformer furnace. Besides, it was also observed that there is bending occurred in one of the pull rods of the counter weight as shown in Fig. 7.

Several nondestructive examinations were performed on reformer tubes inside the fire box such as measurements of outer diameters of the tubes at different levels along the length of each tube at 1.5m, 3m, 5m, and 9m. where no distinguished changes were observed between one tube and another. Hardness measurements on the outer surface were conducted at the same levels which reflected some variations on the values from 220Hv near the top to about 180Hv near the bottom of the tubes. Die penetrant and ultrasonic tests was also performed on weld joints where no cracks were observed.

After removing the insulation from the pig tails, die penetrant test was conducted at the joints with the header. Several cracks were observed as shown in Fig. 8. Also, circumferential cracks were observed at the heat affected zone of the weld joint of the header and the reducer as illustrated in Fig. 9.

One of the bended tubes was taken out of the fire box for metallurgical investigation. The tube is shown in Fig. 10. which clearly illustrates the severe bending specially at the upper half of the tube. Several rings were cut from the tube near the top, at the maximum bowing and near the bottom of

the tube for metallographic investigation. Figure 11 illustrates the microstructure at the top side of the tube. The structure reveals fine carbide precipitations within the grains and few creep void formations at the dendritic grain boundaries where photos were taken at the inner, middle and outer sides of the tube wall thickness. The microstructure of the specimen taken at the maximum bending zone of the tube at the inner, middle and outer surfaces of the tube thickness is shown in Fig. 12. The structures exhibit rather coarser precipitation of secondary carbides inside the grains as compared with the upper zone, and coarse grain boundary carbides as well with larger number of creep voids formation at grain boundaries. It is obviously noticed in Fig. 13. That the secondary carbide precipitations within the grains of the lower part of the tube became much less and larger in size as compared with the middle part and the number of voids at grain boundaries is increased, this reflects the increase in temperature profile along the tube length.

As mentioned earlier, noticed distortion was observed in the levels of the outer pig tails, some of the severely distorted pig tails were replaced by new ones and a small part was taken from one of them near the header for metallographic investigation. The pig tails were made of alloys 800H.

The microstructure of the pig tails specimen is shown in Fig. 14. The microstructure reveals considerable number of creep voids formation at the grain boundaries of the alloy 800H with coarse secondary carbides precipitation within the grains which means that the pig tails were exposed to a higher temperature where creep voids started to occur.



Fig. 3-a Severely bended reformer tubes with color



(a) there is no deformation



(b) there is a sever deformation



(c) there is a sever deformation

Fig. 4 The photos show the sever displacement of outlet pig tails, (a) at reformer entrance. (b) at the middle of the reformer and (c) at the end of the reformer



Fig. 5. Variations in internal distance between the tubes as the result of bending



Fig. 6. Severe rupture of reformer tube which took place one year before, the photos show the large increase in tube diameter due to the creep deformation



(a) Almost in the same level



(b) There is a bending in the pull rod

Fig. 7. General view on counter weight and

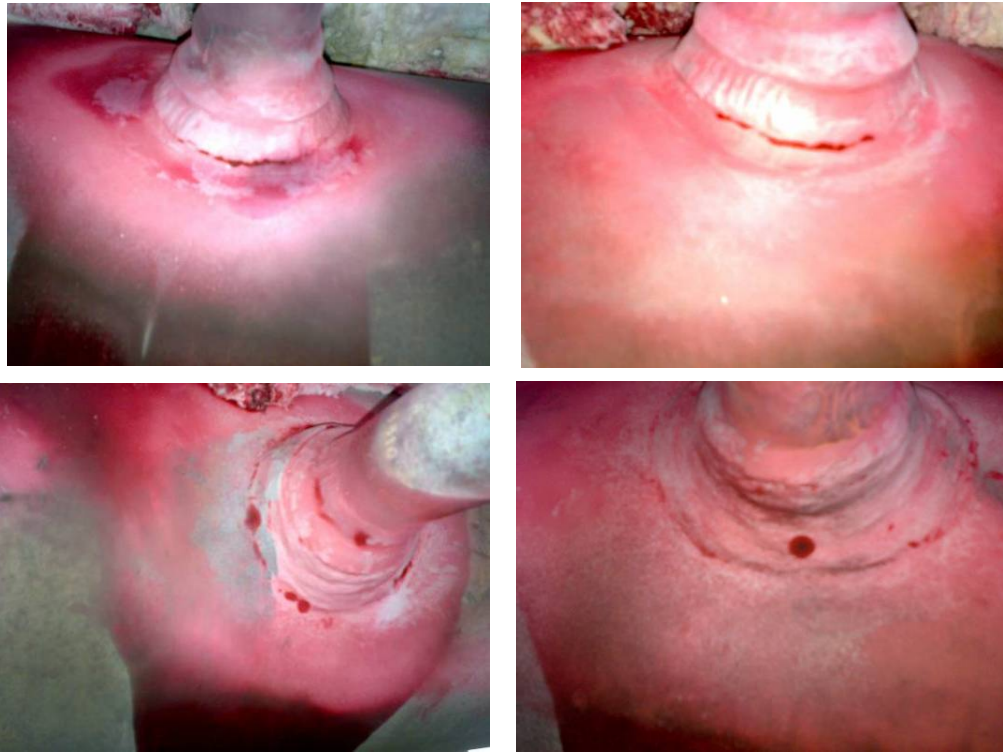


Fig. 8 Cracks at the weld joint of outlet pig tails with the header as revealed by dye penetrant test



Fig. 9. Cracks at the heat affected zone of weld joint between the outlet header and the reducer

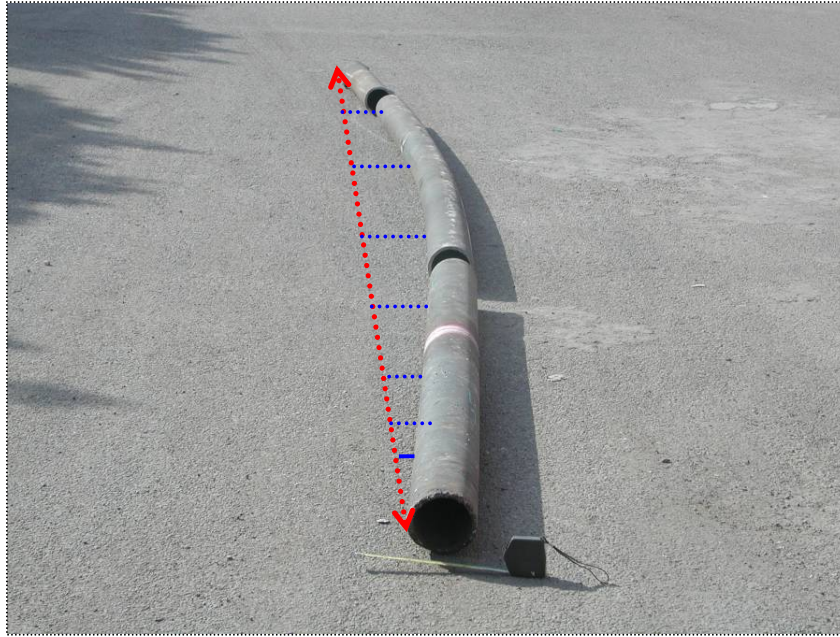


Fig. 10. The photo shows the sever bending of the tube a long its length

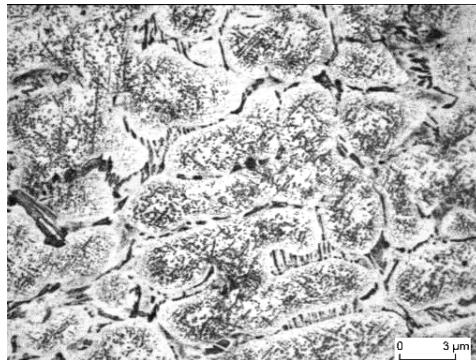
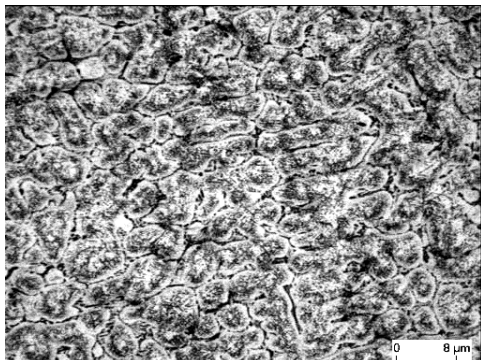
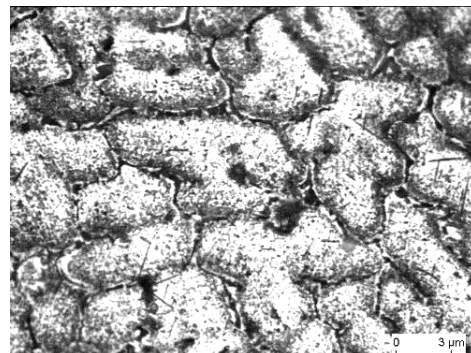
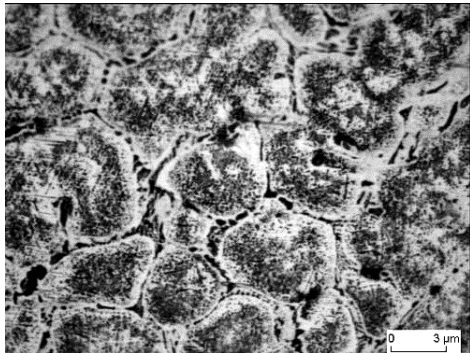


Fig. 11. The photos exhibit few void formation at the denteritic grain boundaries with fine secondary carbides precipitation with in the grains

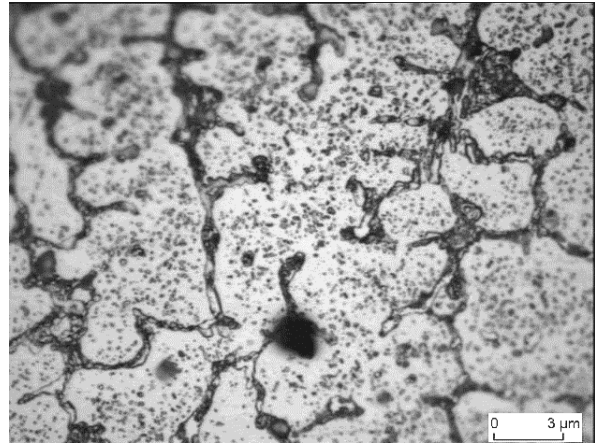
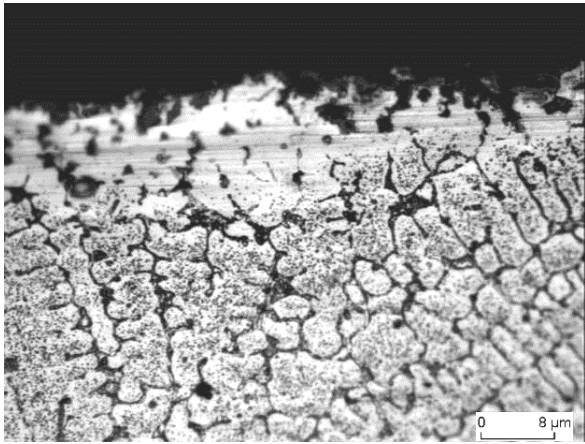
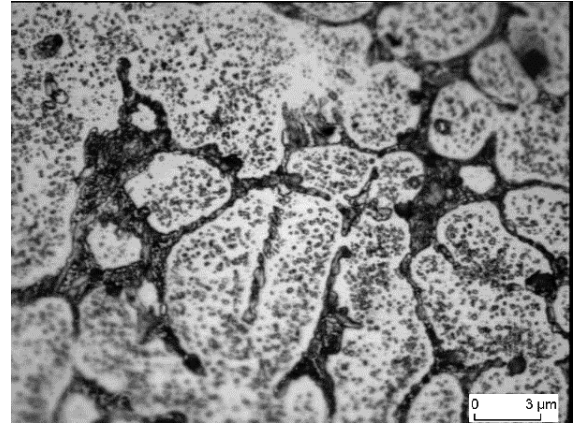
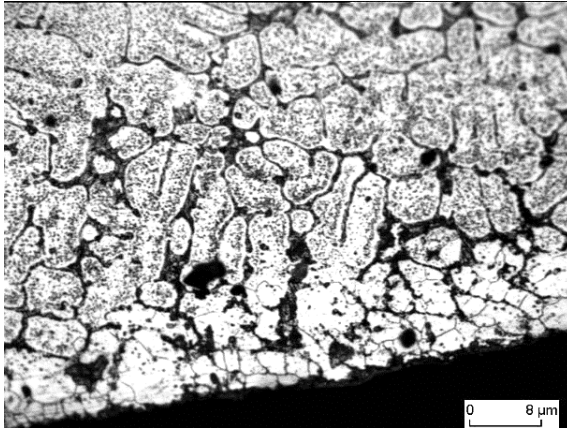
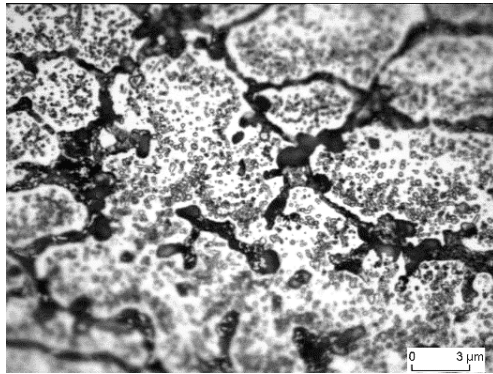
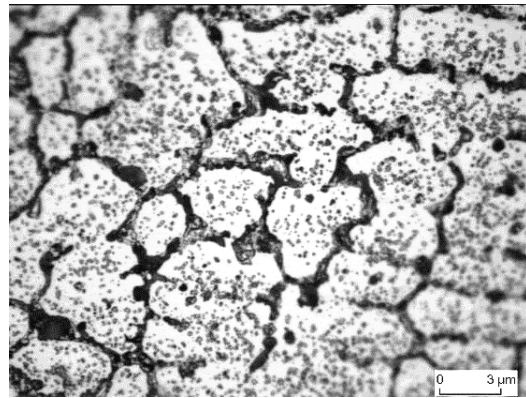
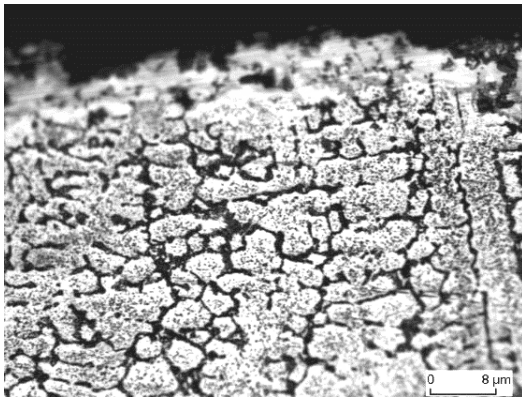


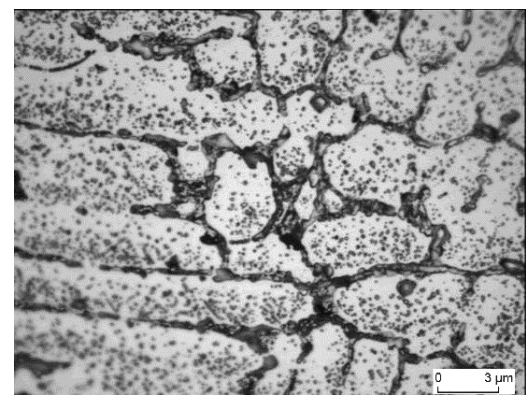
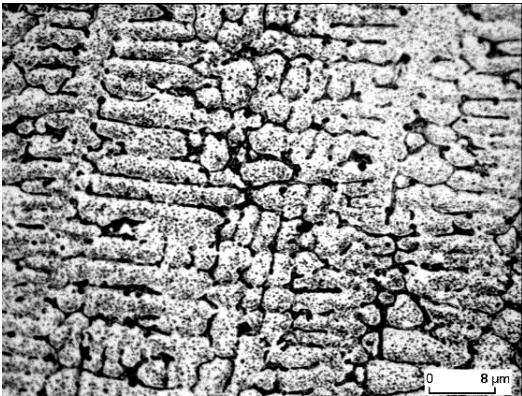
Fig. 12. The photos show the void formation at the grain boundaries of the middle part of the tube through the wall thickness. It also show the increased size of the precipitated secondary carbide



At the inner surface



At the outer surface



Through the thickness

Fig.13. The photos show the extension of voids formation through the wall thickness of the tube at lower and inside the fire box

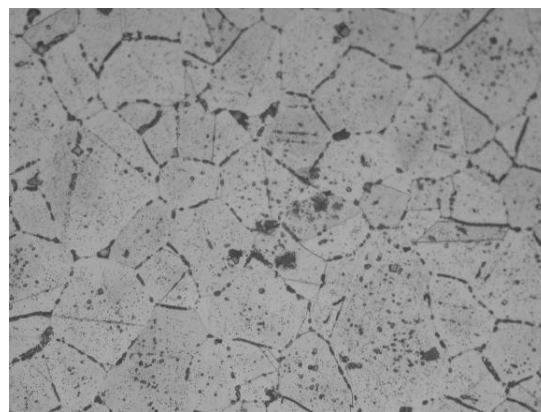
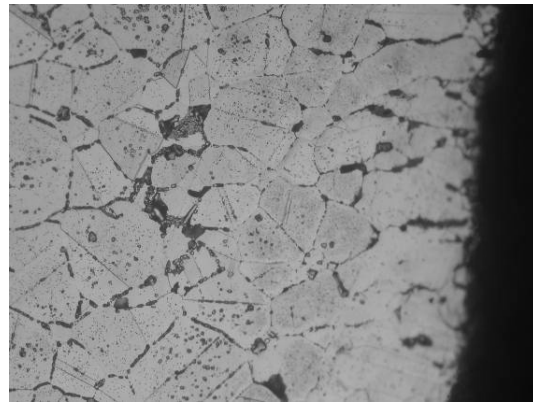
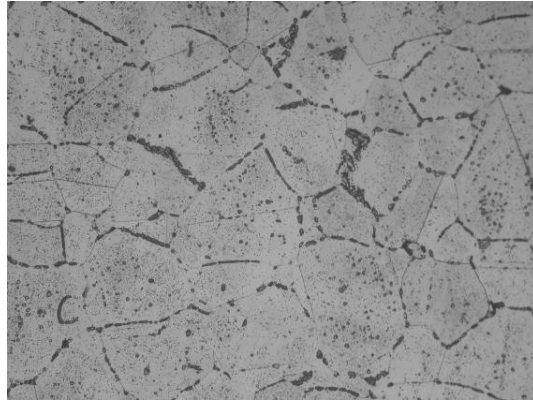


Fig. 14. Microstructure of the pig tail showing relatively large grain size with void formation at grain boundaries

DAMAGE MECHANISMS

Table 1 summarizes the most relevant mechanisms of damage accumulation that dictate the extinction of life in reformer columns, outlet pigtails, and outlet manifolds, based on extensive observations of failed components. . The table also shows the preferential sites for damage accumulation and the damage morphology. For the furnace columns, damage can be by creep, carburization, thermal shock, and accidental overheating, leading to recrystallization and, in the extreme, to liquation of the eutectic carbides in the heat-resistant cast austenitic alloys. On other occasions tubes may suffer gross distortion that, in extreme cases, can interfere with the fitness-for-purpose of the furnace. The effect of such distortions is to bring tubes locally closer together, such that there are local hot spots, arising from the reduction in radial heat loss from the tubes containing the catalyst. The most important damage mechanism leading to life extinction of the tubes is creep, and the effect of increased local temperature causes a dramatic reduction in life. Damage starts in the inner third of the wall, appearing in the form of round voids randomly distributed on dendritic boundaries. Their preferred orientation is on boundaries perpendicular to the maximum principal tensile stress. At 50% of the useful life of the tube, the boundaries show an alignment of creep voids, but without links between them being present. After 50% of useful life, an appropriately chosen cross section will show aligned voids and microcracks produced by their linkage. Some microcracks may reach the internal surface and, conservatively, it may be considered that the useful life is extinct when the cracks reach the outer half of the wall thickness. Creep damage generally results in multiple longitudinal cracks. The basic mechanism involved in causing creep damage is the generation of vacancies (missing atoms) produced during diffusion of species under stress and deformation on an atomic scale: these vacancies tend to congregate on grain boundaries forming pores. With many pores formed, there is a loss of cohesive strength on the grain boundaries and cracks initiate and propagate. The stress state within the column is complex, but it is apparent that the stress due to internal pressure plays a leading role in damage accumulation. As internal pressure varies little along the column length, damage concentrates in the hotter section. The majority of aged reformer tubes that damage distributed along their length, but useful life was controlled by the damage that accumulated in the welds between tube segments situated in the upper third of their length. The main cracks may be found in the centerline of the weld or in the heat affected zone (HAZ). These cracks are transverse to the column and are related to the suspended weight. A weld will only develop longitudinal creep cracks due to hoop stress if the adjacent parent

metal also develops this type of damage. In some cases, where the parent metal acts as a constraint to creep strain in the weld, this type of damage does not occur. Such constraint does not apply in the case of axial tensile stress. Because of this, the weld weakness permits the formation of transversely oriented cracks associated with axial stress, even at higher column sections where the wall temperature is relatively low. When the weld is not this weak, the dominant creep damage occurs in the parent metal at the hotter section of the tube, and the cracks are longitudinal, as should be the case if controlled by hoop stress.

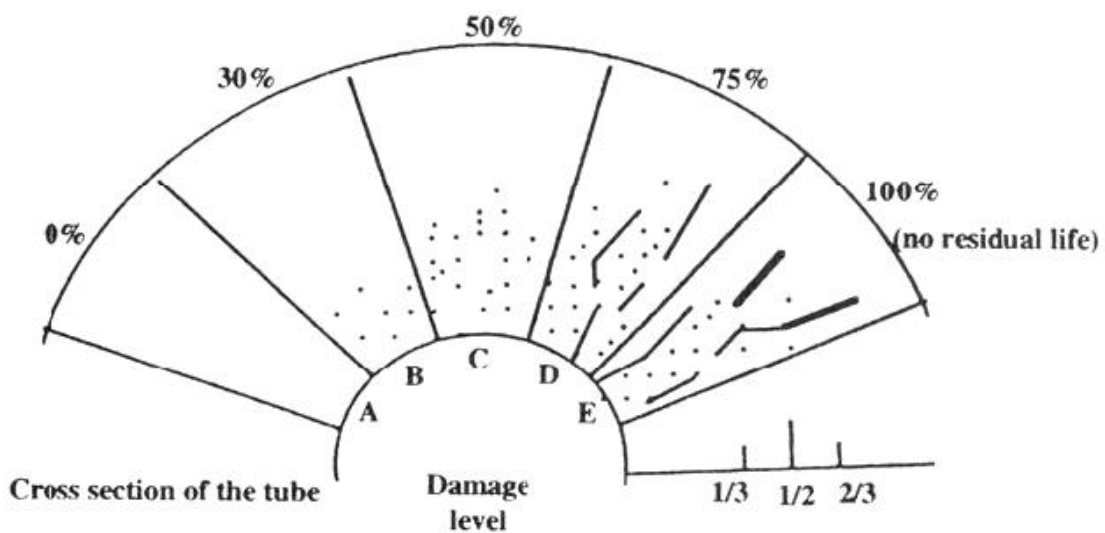


Fig. 15. Classification of the damage in the wall of a reformer tube, as indicated after metallographic preparation.

Table 1. Mechanisms for Life Extinction

Reformer Columns		
Mechanism	Damage	Site
Creep	Aligned voids and multiple cracks start in the inner third of the wall , longitudinally oriented with respect to the column.	Sections in the outer segment of the reformer column.
Creep at welds	A main crack propagates at the center line of the weld deposit starting in the inner third of the wall. Microcracks and aligned creep voids are distributed parallel to the crack. Aligned creep voids and cracks start close to the column internal surface. Cracks are oriented transverse to the column. The fusion line acts a barrier to crack propagation.	Center line of the weld deposit of the welds between cast segments. The most susceptible welds are in the upper third of the columns. Heat affected zone of the butt welds between spindle cast segments. They appear in the upper third of the columns.
Creep buckling	The offset may correspond to several column diameters. The offset may divert the column towards its neighbours or the furnace wall.	May be distributed over the complete length of the column or concentrated in one part.
Carburization	Scale formation, growth of interdendritic carbides and carbide precipitation in the austenitic matrix.	Internal surface of the hotter segment of the reformer column.
Outlet Pigtailes		
Creep	Aligned creep voids and multiple cracks longitudinally oriented, nucleated at the external surface of the pigtail.	The complete pigtail length. In some cases damage is localized at the external radius of bends.
Carburization	Scale formation, loss of thickness, and gross microstructural changes, with loss of ductility	Internal surface
Low cycle, high temperature creep-fatigue	Very localized cracking due to stress concentration, usually nucleated from wedge crack type creep damage due to grain boundary sliding.	Joint between pigtail and outlet header. May also occur at the joint between pigtail and reformer column.
Outlet Headers		
Creep	Aligned creep voids and multiple microcracks longitudinally oriented at the external surface. When the header is poorly supported damage may be transverse due to bending.	May be localized in one segment of the header due to temperature or stress overloads.
Low cycle, high temperature creep-fatigue	Multiple microcracks and aligned creep damage very localized in the stress concentration zone. Usually in small lengths of the joint perimeter, following maximum tensile stress due to bending. Damage may occur by grain boundary sliding with formation of wedge crack cavities: in other cases, relatively low stress produces cracking from round creep voids.	Joint between the header and the tee that leads to the transition piece or between the header and the transition piece where they are welded together.

DAMAGE ASSESSMENT OF REFORMER TUBES

Analytical methods have been developed to assess reformer tubes safe life, as the assessment of damage and advance planning of tubes replacement should be made to ensure that failures and unplanned shutdowns during a campaign are avoided. It is very useful to evaluate the probable extent of damage and remaining life in a particular furnace in a direct manner. A basic problem with the analytical methods is that there is a large degree of uncertainty involved, and an assumed worst case would generally give a pessimistic estimate of remaining life. However, the initial use of an analytical method to provide a first estimate is valuable in identifying if there may be a potential problem and whether a more direct evaluation using inspection procedures should be made.

Figure 15 illustrates the form of the creep damage within a section of a furnace tube and the manner in which it can be classified. The approach] considers Level A as having no detectable voids, Level B as displaying isolated cavities, Level C having oriented cavities, Level D having microcracks, and Level E having macrocracks. In this metallographic procedure, the damage is assessed from a furnace tube removed at the end of a campaign, and chosen to be as representative as possible of the overall condition of the furnace. Damage is revealed through careful (and repeated) polishing and etching of sections from the tube to emphasize the damage as indicated by cavities and microcracks. It is important that the repeated polish–etch procedure is followed as the voids that may be disclosed are not of significant size up to the time that separation occurs along boundaries and microcracks are present. The initial mechanism of void formation is thought to be decohesion at the interface of a precipitate, the small gap opening up through the repeated application of the polish–etch cycles. The voids that are disclosed on tube sections having the form of rings are arranged initially at the dendritic boundaries approximately one-third in from the inner surface. Their alignment follows a direction normal to the principal tensile stress. The microcracks that develop propagate to the internal surface to produce leakage. Experience has shown that the process is sufficiently slow that an effective forecast of the remaining life expectancy can be made by simple qualitative metallography applied to the cross-sections of an extracted sample tube. Reformer tubes are fabricated from several spindle-cast segments butt-welded together. Experience has shown that there are two possible sites for the alignment of the voids. When the weaker link

corresponds to the spindle-cast metal, the alignment and the cracks that follow are arranged in longitudinal planes within the tube. When the weaker link is the weldment, the alignment may be localized in a plane transverse to the tube axis and lying either in the center of the weld or within the heat-affected zone. Thus, different levels of creep life consumption can be attributed to different sections of the reformer tube, based on the distribution of voids and cracks, leading to simple assessment criteria based on the qualitative observations. An important point is that the extent of creep damage is seldom distributed evenly around the complete cross-section of a reformer tube, and this needs to be considered in the sampling procedure for metallographic examination. Complete sections rather than segments of the tube wall are required for the evaluation.

The microstructures of the cast austenitic stainless steels of the ASTM A297 type, Grades HP, or similar, as used for reformer furnaces, change substantially with aging at high temperature and so do their mechanical properties. For example, the ductility at ambient temperature falls to the extent that the tensile elongation may be less than 5% for material aged between 600 and 700°C. Such behavior is normal and the furnace geometry is such that the limited ductility does not interfere with the fitness-for-purpose of the tube. Thus the aging process in itself should not be considered as a process of damage. The changes in microstructure are, however, useful indications of the actual wall temperature. They may be evaluated by field metallography using replicas or by the more conventional destructive metallography applied to cross-sections of a sacrificed reformer furnace tube.

The microstructural changes that take place as a result of prolonged exposure to temperature are primarily alterations in carbide morphology. While time has an influence, the most important factor is temperature, and the microstructures that result can be correlated closely to the service temperature. The microstructural features that relate to the assessment of service temperature were shown in Figures 8-13, and their development is described as follows:-

Below about 600°C microstructural changes are not detectable with light microscopy, and this is designated State I of aging. From 600 to 700°C the primary carbides tend to coalesce and become blocky; as well, secondary carbides nucleate in the interior of the austenite matrix, precipitating first along the edges of the dendrite arms. This is termed State II. Between 700 and 800°C the primary carbides transform completely from a eutectic

morphology to form compact blocks, and very fine secondary carbides are dispersed throughout the matrix, producing State III of aging. Between 800 and 900°C the morphology of the primary carbides stabilizes and the secondary carbides coalesce. Because of carbon diffusion to the primary carbides, there is a loss of secondary carbides along the dendrite boundaries. This is termed State IV. For material exposed to temperatures between 900 and 1000°C, larger coalesced secondary carbides are observed, their numbers being much less than at lower temperatures. A zone denuded in secondary precipitates surrounds the primary carbides: this is State V. Above 1000°C, secondary carbides disappear and the austenite matrix has an appearance similar to the as-cast condition: this is termed State VI. Observations of the transformations of steels of the types discussed indicate that the initial changes in microstructure take place relatively rapidly at a given temperature level (within a few thousand hours) and that thereafter the extent of the change with time becomes small. Thus, the microstructural changes provide a reasonable estimate of the temperature profile to which a furnace tube has been subjected provided they have been in service for several thousand hours.

Conclusion :

The results obtained from metallographic investigation which showed considerable number of creep voids formed at grain boundaries and many of them had coalesced and formed micro fissures or cracks particularly at the lower part of the tube together with the sever bending of the tubes due to the expansion by plastic deformation , indicate that the tubes have already reached the tertiary creep range and about to fracture after relatively short time .

Based on the above mentioned explanation on materials , damage mechanisms and assessment, it could be concluded that all bended tubes should be replaced by new ones in order to avoid the occurrence of any tube rupture again inside the fire box during the next operation period . Such bended tubes are about to rupture if continued operation at such high temperatures.

The results also indicated that the tubes had been operating at higher temperature than the designated one as indicated by the large number of creep voids at grain boundaries, coalescence of primary grain boundary carbides and coarsening of secondary carbides particularly at the bottom of the fire

box. Also, the void formation and precipitation of coarse secondary carbides at the microstructure of the pig tails give indication for higher operating temperature than the designated one. It should be also indicated that the bending of the tubes occurred as a result of the constrained counter balance which could not move as intended to be, resulting in the severe bending of the tube and considerable stresses at the pig tails and the header. These stresses have caused the observed distortion in the levels of pig tails and also the cracks which were noticed at the weld joints between the pig tails and the header. Such cracks were repair welded and inspected by gamma rays after welding and distorted pig tails were replaced by new ones.

Recommendations.

- 1- New set of reformer tubes should be ordered for replacement as soon as possible.
- 2- One or two segments of the header should also be ordered to replace the repaired portion since it might crack again as a result of constrained internal stresses left in the header.
- 3- The company should perform the usual inspection procedure as mentioned in the designer manual by contentious measurement and recording of skin temperature and pressures. Observing hot spots, monitoring the fire condition of the burners, noticing impingement on the tubes or bending of the tubes , watching the counter weights and the leveling of pig tails are very important.
- 4- All possible nondestructive testing techniques should be applied during any shut down of the reformer

Reference:

Tito ling da siveria and Iam le may; The Arab Journal for science and engineering, Vol. 31, No. 2C December 2006 . and its related reference

***AFA WORKSHOP: FITNESS FOR SERVICE IN CHEMICAL
INDUSTRIES***

Aswan, EGYPT

25 - 27 Nov 2012



**An Overview of Risk-based Management Concepts and
Strategies in Chemical Industries**

A.M. Abdel-Atif

Quality Engineering Test Establishment Government of Canada

Ottawa, Canada

An Overview of Risk-based Management Concepts and Strategies in Chemical Industries

A.M. Abdel-latif
Quality Engineering Test Establishment
Government of Canada
Ottawa, Canada

2012-11-29

Fitness for Service in Chemical
Industries NDT & Structural Integrity of
Aircraft

1

Outline

- Total life cycle design consideration
- Measures that Must be Taken for Safe Operations
- Failure Mechanisms
- Challenges facing inspection and maintenance
- Corrosion/Erosion in chemical industries
- Risk management strategies
- Need for Condition monitoring
 - Non Destructive testing and condition monitoring
 - Conventional and non conventional techniques
- Acoustic Emission and corrosion monitoring
- Critical Requirements for data Analysis
- Risk-based Inspection and Maintenance Procedures
- Conclusions

2012-11-29

Fitness for Service in Chemical
Industries NDT & Structural Integrity of
Aircraft

2

Total Life Cycle in Design

- Materials selection operating in different systems operating in aggressive environment
- Environmental compatibility
 - Effect of product on the environment
 - Effect of environment on the product
- Safe design life and metallurgical structural property correlation based on load limits and mechanical properties

2012-11-29

Fitness for Service in Chemical
Industries NDT & Structural Integrity of
Aircraft

3

Total Life Cycle in Design in Chemical Industries

- Resistance to corrosion and/or erosion
- Containment and Preventing leaks
 - Avoiding contamination by corrosion product (processing industries)
 - Maintaining structural integrity, and mechanical properties despite of corrosion or erosion attack.
 - Performance for continuous operation for more than two years. The cost of breakdown is enormous in terms of damage to the environment, clean up, downtime. All these justify the use of expensive materials
- Designing to codes

2012-11-29

Fitness for Service in Chemical
Industries NDT & Structural Integrity of
Aircraft

4



2012-11-29

Fitness for Service in Chemical
Industries NDT & Structural Integrity of
Aircraft

5

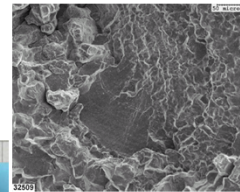
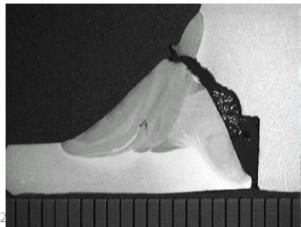


2012-11-29

Fitness for Service in Chemical
Industries NDT & Structural Integrity of
Aircraft

6

Explosions in Waste Heat Recovery Unit



2012

Aircraft

7

Ammonium Nitrate Explosion

A huge explosion ripped through AZF (Azote de France) fertilizer factory in an industrial zone on the outskirts of Toulouse, southwest of France, at 10:15 am, Friday 21 September 2001. The explosion occurred in a warehouse in which stored granular ammonium nitrate.

The amount is said to be between 200 to 300 tonnes of ammonium nitrate, used to make fertilisers. The explosion had been caused by an accident following an "incident in the handling of products". The exact cause remains unknown.



2012-11-29

Fitness for Service in Chemical Industries NDT & Structural Integrity of Aircraft

8

Causes for Leaks in Refineries and Processing Plants

- **Containment losses in a refinery, petrochemical or chemical process plant can be influenced by maintenance and inspection**
 - **Mechanical Failure 41%**
 - **Process Upset 8%**
 - **Sabotage/Arson 3%**
 - **Unknown 18%**
 - **Operational Error 20%**
 - **Design Error 4%**
 - **Natural Hazard 6%**

2012-11-29

Fitness for Service in Chemical
Industries NDT & Structural Integrity of
Aircraft

9

Root Causes for Failure

- **Number of root causes related to safety and safety critical equipment and process control systems:**
 - **Defective or wrongly designed isolation valves**
 - **Deficiencies in the inspection and maintenance procedures for critical equipment**
 - **Unreliable or inadequate process control equipment**
 - **Wrong material selection and inadequately inspected welds in safety critical systems**
 - **Lack of adequate response systems and measures in place**
 - **Absence of contingency plans**

2012-11-29

Fitness for Service in Chemical
Industries NDT & Structural Integrity of
Aircraft

10

Measures that Must be Taken for Safe Operations

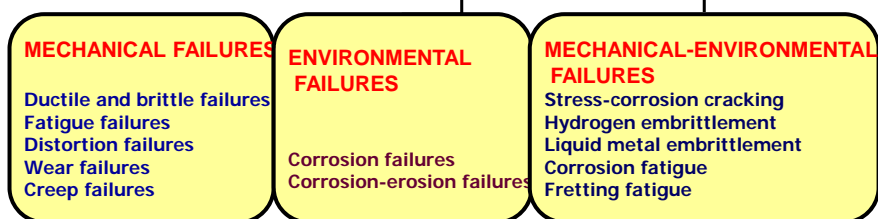
- Define limit state functions for Containment based on extensive knowledge of:
 - Corrosion local /general
 - Stress corrosion cracking
 - Fatigue and corrosion fatigue
 - Creep and creep fatigue
 - Erosion mechanisms
 - Metallurgical considerations.
- Limit load solutions based on:
 - Fracture mechanics
 - Safe life
 - Design limitations and allowable

2012-11-29

Fitness for Service in Chemical
Industries NDT & Structural Integrity of
Aircraft

11

Types Of Failures



2012/11/29

Fitness for Service in Chemical
Industries NDT & Structural Integrity of
Aircraft

12

Failure Modes in Components

- Failure modes take many forms such as fracture, distortion, corrosion, The active stressors are external influences that can direct or indirect cause the failure are:
 - Mechanical- applied stresses, pressure, impact, residual stresses, fretting movement
 - Environmental - exposure to aggressive environment, material compatibility issues,
 - Electrochemical- exposure to corrosive environment
 - Overheating to oxidation and corrosion of turbine Engine components

2012-11-29

Fitness for Service in Chemical
Industries NDT & Structural Integrity of
Aircraft

13

Challenges Facing Inspection and Maintenance

Maximising

- Plant efficiency / reliability levels
- Product generation/throughput
- Competitiveness/ Competition with other producers
- Increase in market share

Minimising (Economic Considerations)

- manning costs
- materials costs
- maintenance work load
- transportation and support
- downtime affecting revenue/operating costs

Maintaining

- contractual nominations

2012-11-29

Fitness for Service in Chemical
Industries NDT & Structural Integrity of
Aircraft

14

Definition of Risk

- Real risk- determined by actual circumstance as the future unfolds (Properties of the hardware)
- Systems- related risks
 - Statistical Risk- determined from currently available data based on engineering design assumptions
 - Predicted risk- based on the analysis of systems, modes and historical data as well as lessons learned from previous failures
 - Perceived risk – determined by institutive individuals or society.
 - Severity of consequences of if an accident occurs taking into consideration the probability of happening
 - Society attitudes concerning tolerance to catastrophic accidents

2012-11-29

Fitness for Service in Chemical
Industries NDT & Structural Integrity of
Aircraft

15

Four Areas of Risk

- Risks to people (Safety Risk)
- Risks to the environment
 - Environmental clean up
 - Community problems
- Risks to the business interruption (Business Risk)
 - Loss of market share
 - Extended downtime
- Risks to capital assets
 - Item repair and or replacement
 - Repair and replacement of structural assets

2012-11-29

Fitness for Service in Chemical
Industries NDT & Structural Integrity of
Aircraft

16

Risk Equation

$$\text{Probability of Failure} \times \text{Consequences} = \text{Risk}$$

Consequence

- Injury to individuals
- Environmental clean up
- Extensive repair
- Downtime
- Loss of market share
- Community problems

Standard Consequence Analysis techniques

- Fault trees
- Leak and Dispersion modeling / Probabilities of ignition Software
- Financial consequence models
- Environmental impact models

2012-11-29

Fitness for Service in Chemical
Industries NDT & Structural Integrity of
Aircraft

17

Justification for Risk Analysis

- To give clear picture of the decisions that must be made to ensure the functional requirements can be met.
- Failure mode and effect analysis (FMEA) to review the reliability of the systems and components. It includes criticality analysis (CrA), failure hazard analysis (FHA) to determine the safety of the systems and expose all the leading causes of failure
- For safe operations we need to develop strategies for risk based inspection and risk based maintenance based on non destructive inspection procedures to ensure structural integrity of the systems and components.

2012-11-29

Fitness for Service in Chemical
Industries NDT & Structural Integrity of
Aircraft

18

Elements of Risk Based Maintenance Strategies

- Risk Based Maintenance (RBM) working process is based on the following detailed processes:
 - Risk Based Inspection (RBI)
 - Safety Integrity Level Assessment (SIL)
 - Reliability Centered Maintenance (RCM)
 - Data management systems and links to CMMS/ERP
 - Technical hierarchy and failure modes, failure and root cause analysis (RCFA)

2012-11-29

Fitness for Service in Chemical
Industries NDT & Structural Integrity of
Aircraft

19

Risk and Hazard Analysis

- The object of risk and hazard analysis is to identify the level of risk and to pinpoint the critical parts of the system that represent the greatest risk of failure.
- Failure free conditions are possible when:
 - Attention to past experiences with similar systems
 - A sound, aggressive risk and hazards analysis during all phases
 - Development of suitable corrective action safety measures and safety programs
 - A continuous and searching review of all phases of program efforts based on systems' reliability data

2012-11-29

Fitness for Service in Chemical
Industries NDT & Structural Integrity of
Aircraft

20

Elements of Risk based Maintenance Management

- The Risk Based Management Philosophy incorporates the latest models in:
 - Reliability Centered Maintenance (RCM) and Root Cause Failure Analysis (RCFA)
 - Risk Based Inspection (RBI)
 - Safety Integrity Analysis (SIL)
 - Task bundling and resource load-levelling

2012-11-29

Fitness for Service in Chemical
Industries NDT & Structural Integrity of
Aircraft

21

Corrosion in Chemical Processing Systems

- Corrosion is a serious problem in chemical process plants specially fertilizer plants. Improper selection of material of construction can lead to equipment failures and unexpected shut downs.
- With improvement in material technology and proper selection of M.O.C. in critical areas, there is marked improvement in reliability of modern fertilizer plants.

2012-11-29

Fitness for Service in Chemical
Industries NDT & Structural Integrity of
Aircraft

22

Erosion-corrosion

- It encompasses a spectrum of mechanisms from accelerated corrosion to a purely mechanical damage, which causes high rates of material loss in industries
- Another definition it is the acceleration or increase in rate of deterioration or attack on a metal because of the relative movement between a corrosive fluid and the metal that results in removal of surface layer gradually in form of small chopping
- Erosion-corrosion is characterized in appearance by grooves, gullies, waves, rounded holes and usually exhibits a directional pattern

2012-11-29

Fitness for Service in Chemical
Industries NDT & Structural Integrity of
Aircraft

23

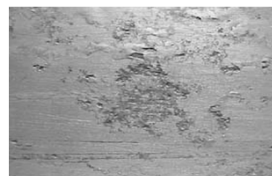
Filiform corrosion



Fig 1 Filiform corrosion on an aileron fastener:

(a) exposed;

(b) underpaint



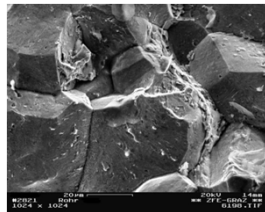
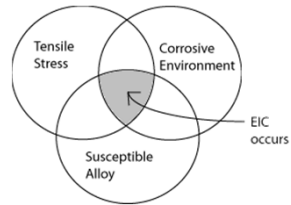
*Figure 2 - Intergranular corrosion
exfoliation on a wing spar.*

2012-11-29

Fitness for Service in Chemical
Industries NDT & Structural Integrity of
Aircraft

24

Stress Corrosion Cracking

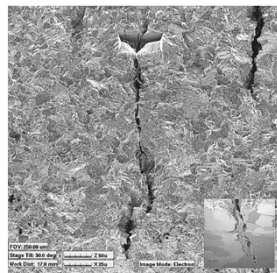
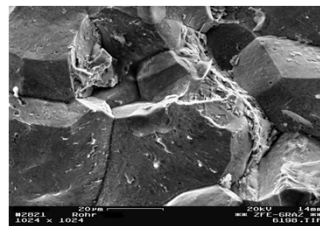
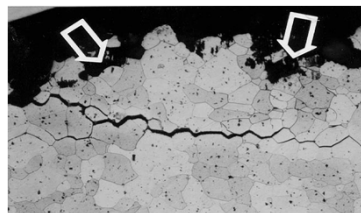


2012-11-29

Fitness for Service in Chemical
Industries NDT & Structural Integrity of
Aircraft

25

Stress Corrosion Cracking



2012-11-29

Fitness for Service in Chemical
Industries NDT & Structural Integrity of
Aircraft

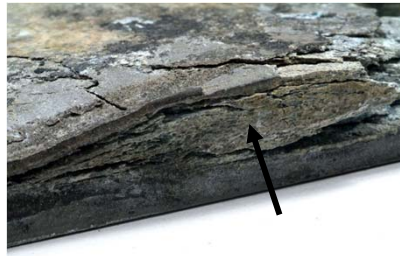
26

Pitting and Pillowing



Pitting

2012-11-29



Pillowing & Exfoliation

27

Fitness for Service in Chemical
Industries NDT & Structural Integrity of
Aircraft

The Need for Permanent Condition Monitoring

- Mentoring is required in multiple piping systems often experience localized flow enhanced corrosion erosion effects that vary with locations experiencing cavitations at bends, slugging areas, and turbulence flow within pipes
- Corrosion and erosion are leading causes of reported spills and pipeline failures
- Estimated 60% of the cost of maintenance are related to spills

2012-11-29

Fitness for Service in Chemical
Industries NDT & Structural Integrity of
Aircraft

28

Improving Plant Reliability through Corrosion Monitoring

Corrosion monitoring techniques are:

- Intrusive methods: such as weight loss coupons and over a period of time and changes in electrical resistance to evaluate the corrosion rate under laboratory conditions and can not definitely give an accurate evaluation of the real condition of equipment or pipeline affected by corrosion.
- Non intrusive methods such as ultrasonics UT to measure thickness along the pipeline.
- On-line corrosion monitoring using sensors

2012-11-29

Fitness for Service in Chemical
Industries NDT & Structural Integrity of
Aircraft

29

Monitoring is Important

- because:
 - Ensure Asset Integrity
 - Loss of Capital Equipment
 - Avoid pollution to environment & damage to public image
 - Reduce Life Cycle cost
 - Optimization of maintenance schedules

2012-11-29

Fitness for Service in Chemical
Industries NDT & Structural Integrity of
Aircraft

30

Corrosion Monitoring Techniques:

- **Direct Measurements**
 - Non Destructive Inspection (NDI)
 - Electrical Resistance (ER) Probes
 - Material Test Coupons
 - Galvanic Currents
 - Cyclic Potentiodynamic Polarization (CPP)
 - Linear Polarization Resistance
 - Electro Chemical Noise (EN)
 - Electrochemical Impedance Spectroscopy (EIS)

2012-11-29

Fitness for Service in Chemical
Industries NDT & Structural Integrity of
Aircraft

31

Methods of NDT

Visua
|
Tap Testing

Microwave

Thermography

Magnetic Particle

X-ray

Acoustic Microscopy

Acoustic Emission

Liquid Penetrant

Ultrasonic

Magnetic Measurements

Replication

Flux Leakage

Laser Interferometry

Eddy Current

2012-11-29

Fitness for Service in Chemical
Industries NDT & Structural Integrity of
Aircraft

32

What are Some Uses of NDE Methods?

- Flaw Detection and Evaluation
- Leak Detection
- Location Determination
- Dimensional Measurements
- Structure and Microstructure Characterization
- Estimation of Mechanical and Physical Properties
- Stress (Strain) and Dynamic Response Measurements
- Material Sorting and Chemical Composition Determination



2012-11-29

Fitness for Service in Chemical
Industries NDT & Structural Integrity of
Aircraft

33

Six Most Common NDT Methods

- Visual
- Liquid Penetrant
- Magnetic
- Ultrasonic
- Eddy Current
- X-ray



2012-11-29

Fitness for Service in Chemical
Industries NDT & Structural Integrity of
Aircraft

34

When are NDE Methods Used?

- To assist in product development
- To screen or sort incoming materials
- To monitor, improve or control manufacturing processes
- To verify proper processing such as heat treating
- To verify proper assembly
- To inspect for in-service damage

2012-11-29

Fitness for Service in Chemical
Industries NDT & Structural Integrity of
Aircraft

35

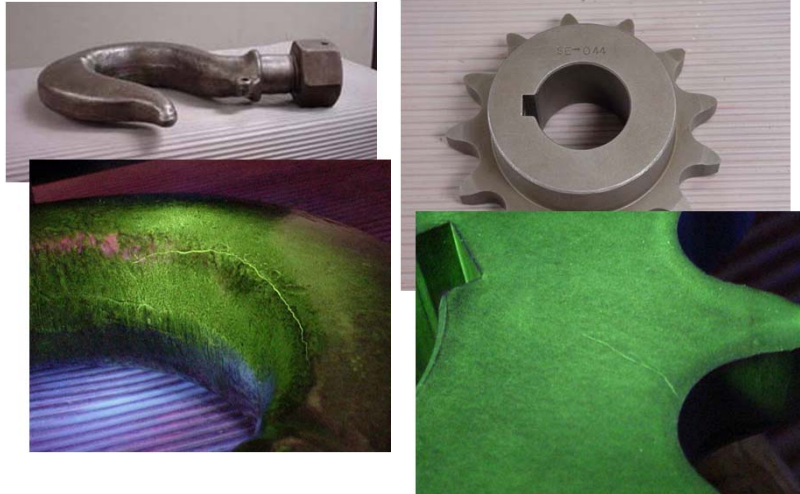
Monitoring Systems Requirements

2012-11-29

Fitness for Service in Chemical
Industries NDT & Structural Integrity of
Aircraft

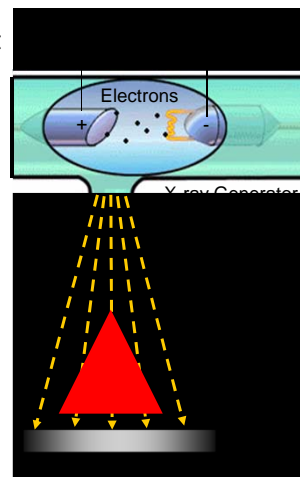
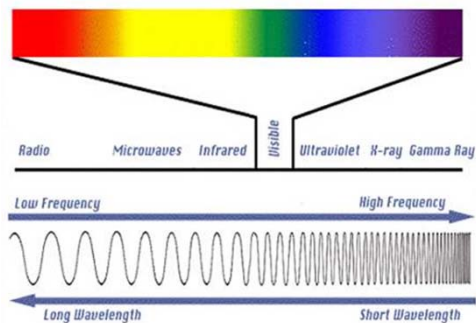
36

Magnetic Particle Crack Indications

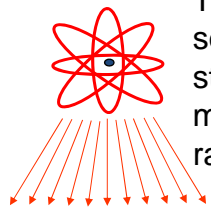


Radiography

The radiation used in radiography testing is a higher energy (shorter wavelength) version of the electromagnetic waves that we see as visible light. The radiation can come from an X-ray generator or a radioactive source.



Film Radiography



The part is placed between the radiation source and a piece of film. The part will stop some of the radiation. Thicker and more dense area will stop more of the radiation.

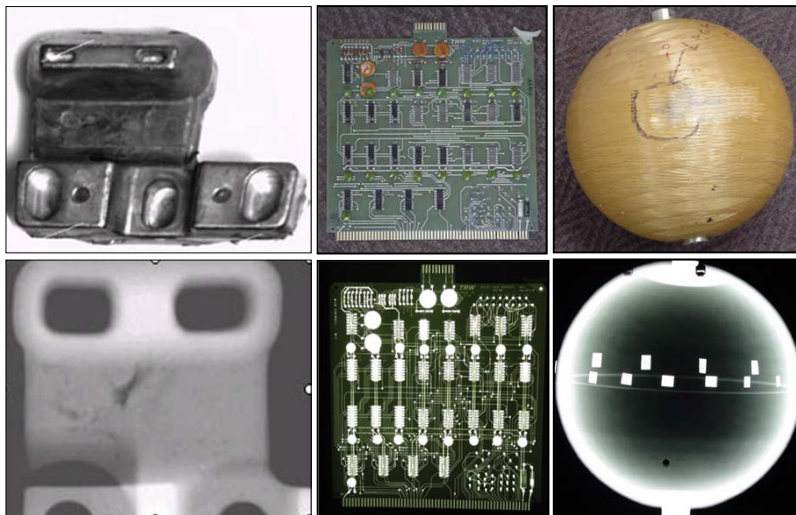


The film darkness (density) will vary with the amount of radiation reaching the film through the test object.

-  = less exposure
-  = more exposure

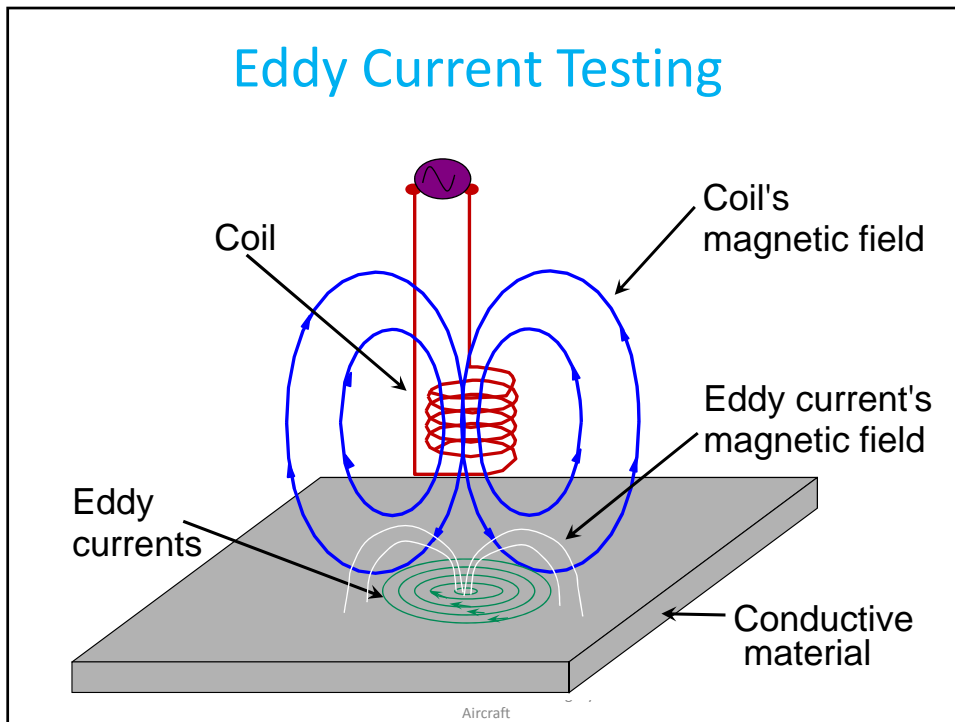
2012-11-29 Top view of developed film Fitness for Service in Chemical Industries NDT & Structural Integrity of Aircraft

Radiographic Images



2012-11-29

Fitness for Service in Chemical Industries NDT & Structural Integrity of Aircraft



Eddy Current Testing

Eddy current testing is particularly well suited for detecting surface cracks but can also be used to make electrical conductivity and coating thickness measurements. Here a small surface probe is scanned over the part surface in an attempt to detect a crack.




2012-11-29
 Fitness for Service in Chemical Industries NDT & Structural Integrity of Aircraft
 42

Basic Principles -System Requirement

- The first phase in the development of a permanent continuous monitoring tool is to determine needs of potential users :
 - The tool should be easy to use, and data collected should be independent of the skills of the operator, i.e. anyone can operate the instrument
 - The tool should provide repeatable measurements, i.e. higher reliability compared to competing techniques, which can be a significant advantage for the concept

2012-11-29

Fitness for Service in Chemical
Industries NDT & Structural Integrity of
Aircraft

43

Improving Plant Reliability through Corrosion Monitoring

- External and internal corrosion attacks of process equipments can reduce equipment performance and lead to unexpected failures and plant shut downs.
- External attack is by ambient environment whereas internal attack is caused by process fluid handled inside.
- Corrosion monitoring is an essential input in Residual Life Assessment and Aging
- Life prediction of the safe design life of critical components in aggressive service conditions.

2012-11-29

Fitness for Service in Chemical
Industries NDT & Structural Integrity of
Aircraft

44

Improving Plant Reliability through Corrosion Monitoring

Corrosion monitoring techniques are:

- Methods that indirectly measure parameters related to corrosion and inter corrosion behavior from some model of corrosion process, e.g. electrochemical potential, pH and temperature.
- Methods that directly measure corrosion behavior, e.g., Non-destructive Inspection,
- Material Test Coupons, Galvanic Currents etc

2012-11-29

Fitness for Service in Chemical
Industries NDT & Structural Integrity of
Aircraft

45

Corrosion Monitoring Techniques:

- **Direct Measurements**
 - Non Destructive Inspection (NDI)
 - Electrical Resistance (ER) Probes
 - Material Test Coupons
 - Galvanic Currents
 - Cyclic Potentiodynamic Polarization (CPP)
 - Linear Polarization Resistance
 - Electro Chemical Noise (EN)
 - Electrochemical Impedance Spectroscopy (EIS)

2012-11-29

Fitness for Service in Chemical
Industries NDT & Structural Integrity of
Aircraft

46

Common Inspection Practices

- Monitoring of any material loss process involves manually
- Scanning pipe-works, vessels and pipelines with an ultrasonic probe by an skilled operator
- Inspector is also responsible for having a suitable UT probe (size, frequency, type, temperature resiliency, etc ...) and coupling medium for a specific inspection
- For correct corrosion/erosion estimates (metal loss trends) several readings at same point on different time interval are required

2012-11-29

Fitness for Service in Chemical
Industries NDT & Structural Integrity of
Aircraft

47

Common Inspection Practices

- Traditionally - High cost may be incurred due to the necessity of removing insulation, erecting scaffolding, shutting down plants, excavating pipelines and logistics

What we need is:

A surveillance system that can be installed in restricted, critical or costly to access areas and then monitored remotely or with occasional access just to download data

2012-

Fitness for Service in Chemical
Industries NDT & Structural Integrity of
Aircraft

48

The Key Component of the Permanent Monitoring System

- Probes (Sensors)
- Electronics data processors
- Visualization software

2012-11-29

Fitness for Service in Chemical
Industries NDT & Structural Integrity of
Aircraft

49

The Key Features for a Permanent Monitoring System

- Non – Intrusive Inspection
- Sensors are bonded to the inspection area permanently
- Remote Location Monitoring- (manned or un-manned) remote pipeline sites or inaccessible area (e.g. Power Plants, Refineries, etc...)
- No recurring Scaffolding/Excavation Costs
- Early Warning System can be utilized with a customized software to provide trending, warning and alarm information with availability of data on demand or with occasional/periodic access

Operator Safety

- Eliminates the need to send operator into hazardous locations and environment or remote areas to carry out wall thickness measurements
- Measurement Accuracy

2012-11-29

Fitness for Service in Chemical
Industries NDT & Structural Integrity of
Aircraft

50

Effective Features of Permanent Monitoring System

- Improved measurement reliability is considered more important than accuracy/sensitivity. However, improved accuracy & resolution would be significant plus for the tool
- Sensor positioning is critical for repeatability and reproducibility of data points for periodic comparison and conclusion for calculating metal loss rates and different degradation phenomena
- Portability is also important
- The number of sensors used may be critical to the success of inspection since each user will likely to have different configuration and sizes for different inspection locations

2012-11-29

Fitness for Service in Chemical
Industries NDT & Structural Integrity of
Aircraft

51

Electronic Hardware Specifications

- Multi Channel Conventional Ultrasonic Probes capable of recording thickness measurements from all channels simultaneously within a predefined time-interval
- Portable electronics in a customizable box:
 - Includes basic features of a portable flaw detector
 - Flexible to implement extra features on customer request
 - Data storage capabilities & Ethernet peripherals
- Wireless capability, with several alarming options, e.g. audible, visual for system performance
- Connect and operate from a laptop using available Ethernet port up to a distance of 100 m

2012-11-29

Fitness for Service in Chemical
Industries NDT & Structural Integrity of
Aircraft

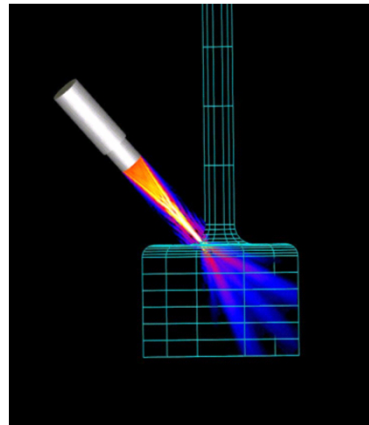
52

Ultrasonic Imaging

High resolution images can be produced by plotting signal strength or time-of-flight using a computer-controlled scanning system.



Gray scale image produced using the sound reflected from the front surface of the coin



Gray scale image produced using the sound reflected from the back surface of the coin (inspected from "heads" side)

2012-11-29

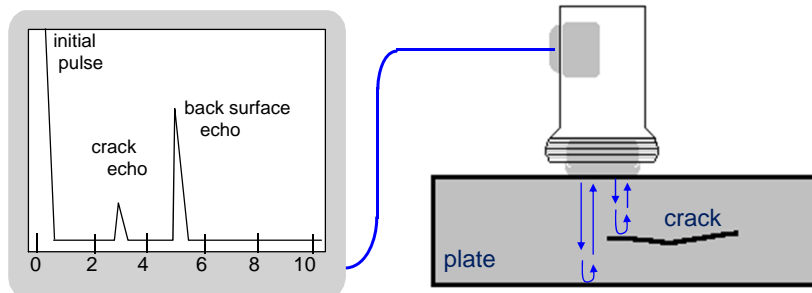
Services for Service in Chemical Industries NDT & Structural Integrity of Aircraft

53

Ultrasonic Inspection (Pulse-Echo)

High frequency sound waves are introduced into a material and they are reflected back from surfaces or flaws.

Reflected sound energy is displayed versus time, and inspector can visualize a cross section of the specimen showing the depth of features that reflect sound.



Oscilloscope, or flaw detector screen

2012-11-29

Services for Service in Chemical Industries NDT & Structural Integrity of Aircraft

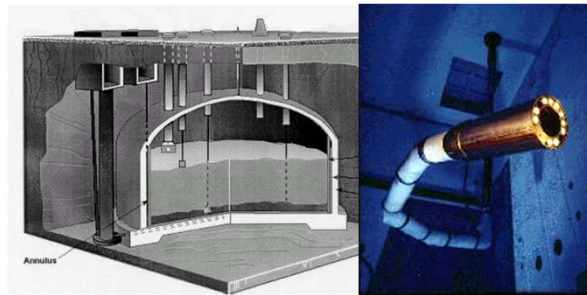
54

Storage Tank Inspection

Robotic crawlers use ultrasound to inspect the walls of large above ground tanks for signs of thinning due to corrosion.



Cameras on long articulating arms are used to inspect underground storage tanks for damage.



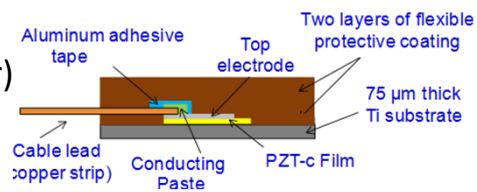
2012-11-29

IndustriesNDT & Structural Integrity of Aircraft

55

Sensors Components

- Metal Substrate
- PZT-Film (actual sensor)
- Top Electrode
- Conducting Paste
- Cable Lead (copper strip)
- Adhesive Tape
- Weather Protective Coating
- Cable from Cable Lead to Electronics Box



2012-11-29

Fitness for Service in Chemical IndustriesNDT & Structural Integrity of Aircraft

56

Erosion - Corrosion

- Erosion-corrosion propagation leads to an increase of AE activity and to the emission of signals with high value of hits, number of counts, amplitude, frequency and energy.
- The most effective range of amplitude for erosion-corrosion in case of laminar flow is between 61 dB to 65 dB, and for turbulent from 68 dB up to 72 dB.
- From AE signals, it is possible to identify whether the type of the flow is laminar or turbulent, which can be done by the form of the AE energy, which for turbulent flow reaches a very high level of AE energy above the saturation level of 65000 v².s with low activity. On the other hand for laminar flow it shows a high AE activity and propagation at lower AE energy level.

2012-11-29

Fitness for Service in Chemical
Industries NDT & Structural Integrity of
Aircraft

57

Erosion-corrosion

- It encompasses a spectrum of mechanisms from accelerated corrosion to a purely mechanical damage, which causes high rates of material loss in industries
- *Another definition it is the acceleration or increase in rate of deterioration* or attack on a metal because of the relative movement between a corrosive fluid and the metal that results in removal of surface layer gradually in form of small chopping
- Erosion-corrosion is characterized in appearance by grooves, gullies, waves, rounded holes and usually exhibits a directional pattern

2012-11-29

Fitness for Service in Chemical
Industries NDT & Structural Integrity of
Aircraft

58

Acoustic Emission

- Acoustic Emission (AE) is stress waves produced by sudden movement in stressed materials
- The traditional emission sources are defect-related deformation processes such as crack growth and plastic deformation
- The AE propagation from the source, throughout the structure can be listened and that technique is used worldwide for detecting and locating defects as they occur, across the entire monitored area, providing early warning of failure, in a timely and cost effective manner
- AE for online monitoring, to improve a great ability in detecting corrosion under insulation of piping during operation.
- For monitoring erosion-corrosion with association of acoustic emission, an AE signals are analyzed in terms Hits, Amplitude, counts, energy, frequency and time, during operations in service.

2012-11-29

Fitness for Service in Chemical
Industries NDT & Structural Integrity of
Aircraft

59

Acoustic Emission Testing (AE)

- Pre-diagnosis enhances the safety and integrity of the whole pipeline systems
- Early detection of erosion-corrosion enhances the overall system dependability and safety
- AE assessment can be used as the basis for continuous plant monitoring, increasing structural safety and reducing shutdown costs for inspection
- AE has the highest accuracy in quantified damages for intermediate and relative high corrosion rates

2012-11-29

Fitness for Service in Chemical
Industries NDT & Structural Integrity of
Aircraft

60

Acoustic Emission Testing (AE)

- Erosion-corrosion in pipeline is characterized by using the detection of the acoustic emission (AE) during the operation of the pipeline at different flow rates and velocities
- By comparison with other techniques, the sensitivity of the AE technique is higher than other conventional non-destructive testing methods like dye penetrant, magnetic interference or ultrasonic testing
- Online monitoring for erosion-corrosion in pipeline is extremely important for early detection of any abnormal phenomena that may lead to catastrophic accidents.

2012-11-29

Fitness for Service in Chemical
Industries NDT & Structural Integrity of
Aircraft

61

AE for Monitoring Erosion-Corrosion

- From AE signals, it is possible to identify whether the type of the flow is laminar or turbulent, which can be done by the form of the AE energy, which for turbulent flow reaches a very high level of AE energy above the saturation level of $65000 \text{ v}^2 \cdot \text{s}$ with low activity. On the other hand for laminar flow it shows a high AE activity and propagation at lower AE energy level.
- Erosion-corrosion propagation leads to an increase of AE activity and to the emission of signals with high value of hits, number of counts, amplitude, frequency and energy.
- The range of the amplitude for erosion-corrosion for carbon steel elbow in a fully operating system is between 60 dB to 71 dB.
- The most effective range of amplitude for erosion-corrosion in case of laminar flow is between 61 dB to 65 dB, and for turbulent from 68 dB up to 72 dB.
-

2012-11-29

Fitness for Service in Chemical
Industries NDT & Structural Integrity of
Aircraft

62

AE-Analysis Parameters

- Correlation between counts and amplitude, a laminar flow can be identified from turbulent flow without the need to know the velocity of the flow by checking the form of the signal as it has a uniform shape unlike turbulent flow.
- The frequency range of erosion-corrosion in seawater 60-350 kHz and the maximum peak is 110 kHz for laminar flow and 130 kHz for turbulent one.
- Rate of erosion-corrosion is directly proportional to hits as the velocity increases.
- Generally, AE method is a promising technique to monitor the erosion corrosion process in carbon steel pipelines.

2012-11-29

Fitness for Service in Chemical
Industries NDT & Structural Integrity of
Aircraft

63

Erosion Corrosion –AE data Analysis

- Also from the correlation between counts and amplitude, a laminar flow can be identified from turbulent flow without the need to know the velocity of the flow by checking the form of the signal as it has a uniform shape unlike turbulent flow.
- The frequency range of erosion-corrosion in seawater 60-350 kHz and the maximum peak is 110 kHz for laminar flow and 130 kHz for turbulent one.
- Rate of erosion-corrosion is directly proportional to hits as the velocity increases.
- Generally, AE method is a promising technique to monitor the erosion corrosion process in carbon steel pipelines.

2012-11-29

Fitness for Service in Chemical
Industries NDT & Structural Integrity of
Aircraft

64

Critical Requirements for data Analysis

- There is a need for advanced centralized data viewing and integration of NDT to asset management databases
- NDT data gathered from modern on-stream techniques, in a user friendly form that will permit data fusion and structure visualization, is discussed and software based solution is presented
- Fusion of in service Acoustics Emission and automated UT testing for corrosion mapping as applied on spheres, pressure vessels and above ground storage tanks.
- Fusion of Acoustic Emission data with ones from ultrasonic scanning can be very effective in condition health monitoring.

2012-11-29

Fitness for Service in Chemical
Industries NDT & Structural Integrity of
Aircraft

65

Fusion of NDT

- An increasing demand for cost-effective inspections and maintenance is driving the industry to modern solutions, which will provide the necessary inspection results for the condition monitoring of equipment in chemical plants and refineries with minimum disruption to operations and low cost.
- Results visualization is an important step towards successful interpretation of NDT data to proceed with efficient structural integrity assessment and fitness for service.
- Visual combination of NDT data from different methods is becoming increasingly important as modern NDE techniques produce large amounts of results within short inspection time.

2012-11-29

Fitness for Service in Chemical
Industries NDT & Structural Integrity of
Aircraft

66

Disaster Management Plan

- Disaster Management forms an integral part of any Industrial Activity Management in dealing with the hazards and risks which may have impact on environment, human lives, health and safety and business interests. It is the means by which an industry manages itself in order to mitigate these risks
- Management planning is the identification and assessment of the principal hazards.
- The hazard can be fire, explosion, toxic release, failure of structure or vessel holding hazardous substances, sudden heavy toxic emissions from exhausts/ vents.

2012-11-29

Fitness for Service in Chemical
Industries NDT & Structural Integrity of
Aircraft

67

Disaster Management Plan For Chemical Processing Factories

- Identification of vulnerable points likely to result in Disaster are essential through Operational experience and Past history.
- The "Off-Site Emergency / Disaster Management plan" begins beyond the premises of the plant.
- The off site emergency plan will be under the control of local administration. The plant authorities need to extend their cooperation to the local administration.
- The Plant authorities should make available their 'on site emergency plan' so that the nature of risks and hazards involved in the plant will be known to all the concerned people.
- The copies of emergency plans should be with the government authorities (e.g. Administrator / Fire station officer/ Factory Inspectorate/ Environment Authorities etc).
- The people living in the immediate vicinity of the plant should be made fully aware of the plant activities and the possible risks associated with the processes.

2012-11-29

Fitness for Service in Chemical
Industries NDT & Structural Integrity of
Aircraft

68

Summary of Risk-based Inspection and Maintenance Procedures

- Develop a generic procedure for risk based inspection and maintenance (RBM).
- Develop the procedure that :
 - defines the principles behind making risk based decisions
 - defines the scope and limitations of an RBM analysis
 - set requirements to an RBM analysis
 - describes the management processes needed to support the use of risk based techniques
 - provides the steps in developing a RBM plan
- Develop and document methods for risk assessment to be used within RBM
- Prepare industry specific workbooks for the petrochemical, power, steel, and chemical industries.

2012-11-29

Fitness for Service in Chemical
Industries NDT & Structural Integrity of
Aircraft

69

Benefits from RBI/RCM Implementation

- Increased intervals between turnarounds (4 yrs to 6 yrs)
- Decrease in hidden failures, process trips (not quantified)
- Improved process monitoring allowing for mitigation of failures
- Fully documented, consistent and integrated maintenance and
- Decrease in maintenance costs (est. 8% to 10%)
- Development of operator-round process monitoring procedures.
- Identification of "other reliability issues" such as design changes, procedure changes, potential hidden failures, significant drawing errors
- Identification of non critical equipment that were and eliminating many unnecessary maintenance tasks

2012-11-29

Fitness for Service in Chemical
Industries NDT & Structural Integrity of
Aircraft

70

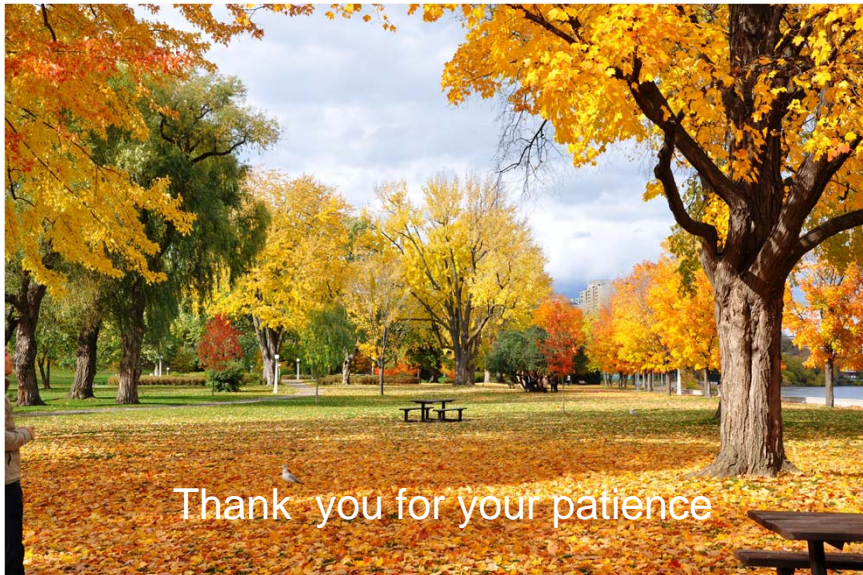
Conclusions

- Experience from conducting RBI and RCM studies for refineries, petrochemical, chemical, and offshore topsides has demonstrated significant potential risk reductions and cost benefits of the predictive and proactive maintenance strategies developed.
- The benefits of the integrated RBM process will be exceeding the benefits achieved for the individual initiatives *due to synergy effects* such as: job packing, improvement to data management and workflow.
- Improved reliability of the equipment items and hence the system can be achieved.
- Maintenance intervals can be optimized based on the continuous feed back from the maintenance activities and the failure records and failure causes identified.

2012-11-29

Fitness for Service in Chemical
Industries NDT & Structural Integrity of
Aircraft

71



Thank you for your patience

2012-11-29

Fitness for Service in Chemical
Industries NDT & Structural Integrity of
Aircraft

72

***AFA WORKSHOP: FITNESS FOR SERVICE IN CHEMICAL
INDUSTRIES***

Aswan, EGYPT

25 - 27 Nov 2012



Integrated inspection and failure analysis of boilers

Dr. H. Abdel-Aleem

CMRDI, Egypt

Integrated Inspection and Failure Analysis of Boilers

H. A. Abdel-Aleem *, Essam Ibrahim* and B. M. Zaghoul*

* Central Metallurgical R& D Institute (CMRDI), Manufacturing Technology Dept.
Welding and inspection Lab. P.O.Box 87 Helwan, Egypt, khamedk@yahoo.com

ABSTARCT

The integrated inspection has a significant economic benefit. It minimized the risk of unplanned shutdowns due to trouble failure, allows boilers to be operated more aggressively and provides a wealth of diagnostic information. The integrated inspection usually includes non destructive evaluation (NDE) for different boiler components and failure analysis for failed component. NDE for boilers is done to obtain enough data to allow the engineer to assess and make decisions regarding the integrity of boiler competent. Beside the non destructive evaluation, failure analysis of failed component play vital role to identify the cause of a failure and how to prevent it from recurring. Integrated inspection can be an important part of the boiler fitness survey.

Key words; Boilers, integrated inspection and Failure analysis

1. INTRODUCTION

NDE for boilers is done to obtain enough data to allow the engineer to assess and make decisions regarding the integrity of boiler competent. The selection of appropriate NDE methods will depend on material of the component and location the damage type which expected as well as the limitations caused by the arrangement and geometry of the component. Failure analysis is the process of collection and analyzing all the available data to identify the cause of a failure and how to prevent it from recurring. it is an discipline in many industries such as petrochemicals industries and fertilizer industries. Failure analysis provide a clear picture of the root case and include recommendations to avoid similar future failure. Beside the non destructive testing, failure analysis of failed component is used to prevent future occurrence, and /or to improve the performance of the components.

2. INTEGRATED INSPECTION

The presentation will draw on the experience of Welding Research and Inspection Department at CMRDI in conducting metallurgical inspections and failure analysis on boilers and preparing detailed inspection report on remaining life assessment

The purpose and methodology of life assessment for boilers are to :-

- Evaluate the present state and the condition of the boiler components in order to continue stable and reliable boiler operation
- Evaluate the remaining life for Superheater and Reheater by metallurgical inspection
- Evaluation of creep life and future inspection scheme by metallurgical inspection for water wall, economizer, Superheater and Reheater tubes

- Evaluation degree of creep damage for Superheater and Reheater by hardness test
- Evaluate the remaining life based on thickness Measurement for water wall,
- Evaluate the remaining life based on thickness thinning for economizer due to low Temperature Corrosion,
- Evaluate the remaining life based on thickness thinning for Superheater and Reheater tubes due to high Temperature Corrosion
- Confirm the cause of the inner scale generation
- Evaluate the remaining life based on check of metal structure ,inner scale ,etc for sample tube at laboratory
- Evaluate the remaining life based on check of metal structure ,inner scale ,etc for sample tube

3. FAILURE ANALYSIS OF BOILER WATER WALL FURNACE TUBE

The presentation will also focus on the most common types of pressure part failure and metallurgical mechanism involved based on actual data obtained from the inspection of several boilers. Failure of water furnace wall tube will be presented. In the presented case study, the boiler has experienced failure problem with one of its water wall furnace tubes after 209000 hours of operation. The nominal outer diameter and wall thickness of these tubes are 63.5mm and $6.73 \pm 12\%$ mm, respectively. The boiler' water wall tubes were made of low alloy steel type ASTM SA213-T2 as mentioned by the company side.

The boiler's design pressure and temperature are 178-180 kg_f/cm^2 and 540 $^{\circ}\text{C}$, respectively. The subject boiler is a vertical type with a capacity of 1,070 ton/hr and it has been set into operation since 1985. The boiler tubes were subjected to acid cleaning in August, 1992.

The rupture took place within the firing zone of the boiler. The ruptured part of the tube was cut out for failure investigation. Meanwhile, other non-ruptured tube sample was cut out from the same boiler furnace in-service-tubes to evaluate the present status of the subject boiler furnace tubes. Also, new tube (from the plant warehouse) was inspected for comparison.

3.1 Investigation

3.1.1 Macro-investigation

The received tube sample of 35 cm length, cut from in-service seamless tube, was carefully examined before sectioning it for destructive investigations. It is clear from Fig. 1 that the received tube had a large longitudinal fish-mouth rupture with about 29 cm length. The tube showed large bulging before fracture with a height reaches to 15 mm . Moreover, the rupture terminated at one end in a thick-walled transverse tear. The ruptured tube part was totally covered by a thick stacked deposits at the fire side, while these deposits were thin, friable and was easily removed at the other side (180° from the fracture edges), as shown in Fig.1.

Regarding the in-service- non-ruptured tube, the received sample was about 25 cm length with 64 mm outer diameter as shown in Fig. 2. The part was totally covered by heavy irregular deposits at

the fire side, while the other side (180° from the fire side) was smooth without any deposits, as shown in Fig. 2. Visually, there was no indication for bulging in the tube fire side.

In order to examine the inner surfaces, the ruptured and non-ruptured tubes were cut longitudinally around its ruptured/bulged zone (in the spacer weld). In general, abnormal thick radish color layer of deposits covering both the tube inner surface facing the fire and the other side were observed.

For more detailed investigation, the ruptured and non-ruptured tubes inner surfaces were chemically cleaned to completely remove the deposited products from the original inner surfaces. The original inner surface of the ruptured tube at the fire side showed small and shallow pitting most probably from the previous acid cleaning, while these pitting were less pronounced at the other side. Regarding the inner surface of the non-ruptured tube, the fire side showed some strongly stacked deposit layers, while the other side was free from any surface defects.

The deposited products collected from tubes inner and outer surfaces were analyzed using X-ray diffraction (XRD) technique for the phases identifications. It was found that the outer scale consisted mainly of sodium sulfides (Na_2SO_4), iron oxide (magnetite Fe_3O_4), and iron sulfides (FeSO_4), while the tube inner scale consisted mainly of iron oxides (hematite Fe_2O_3 , magnetite Fe_3O_4 , and FeOOH).

The ruptured and non-ruptured tubes wall thicknesses at different locations were measured and recorded in Table 1 which shows great variations in the ruptured tube wall thickness especially at the fracture edges. The results indicated that the wall thickness was about 7.4 mm at the other fire side, while it reached 4.8 mm at the fracture edges (Table 1). On the other hand, both the fire and other sides of the non-ruptured tube part showed almost same wall thickness measurements of about 7.5 mm. These results have been confirmed by sectioning the tubes at different locations for ovality checking (See Figs.3 and 4). The ovality of the in-service-non-ruptured tube cross-section, as shown in Fig. 4, was reasonable, while there were thinning in the tube cross-section of the ruptured tube even before the fracture as shown in Figs. 3 (b) and (c). It is important to record here that the new tube (from the power plant warehouse) showed reasonable ovality with about 7.6 mm and 64 mm wall thickness and outer diameter, respectively, as shown in Fig. 5.

Table 1. Wall thickness at different locations at tube samples.

Tube sample	Wall thickness, mm	
	Fire side	Other side (180° from the fire side)
Ruptured tube	4.8	7.5
Non-ruptured tube	7.4	7.6

Samples were cut from the received tubes (ruptured, non-ruptured, and new tubes) for material confirmation. The chemical analysis of the material given in Table 2 together with the analysis of ASTM SA213-T2, Seamless Ferritic and Austenitic Alloy-Steel Boiler, Superheater and Heat –Exchanger Tubes, shows that all the received tubes materials (ruptured, non-ruptured, and new tubes) conform to of ASTM SA213-T2.

Table 2. Chemical composition of received tube samples together with the specified range for ASTM SA213-T12 steel (wt.%).

Materials	Chemical compositions%							
	C	Mn	P	S	Si	Cr	Mo	Fe
ruptured	0.148	0.394	0.014	0.010	0.222	0.613	0.506	Bal.
Non-ruptured	0.141	0.397	0.014	0.009	0.219	0.623	0.501	Bal.
New tube	0.159	0.379	0.020	0.014	0.166	0.603	0.490	Bal.
ASTM SA213-T2	0.1~ 0.2	0.3~ 0.60	≤0.025	≤0.025	0.1~ 0.3	0.5~ 0.81	0.44~ 0.65	Bal.

3.1.2 Micro-investigation

Metallographic examinations were conducted on several samples cut from the received tubes (ruptured, non-ruptured, and new tube) and the results are shown in Figs. 6-10. Microstructure of the received ruptured tube at the fire side exhibited ferrite and almost complete decomposition of pearlite. Eventually, at the ruptured edges, the pearlite carbide plates vanished altogether. Another important notice in this critical area is the formation of isolated voids particularly, on grain boundaries of the fractured edges (See Fig. 6). These microstructural observations (pearlite decomposition and voids formation) were detected also in areas apart from the fracture at the fire side (See Fig. 7 (a)). At areas relatively away from the fracture edges, but still at the fire side (90° from the fracture edges), small volume fraction of pearlite in grey color (traces) are detected (See Fig. 7 (b)). On the other hand, the other side (180° from the fracture edges) showed normal ferrite (white) – pearlite (grey) structure with lamellar pearlite structure (See Fig. 8).

Regarding the non-ruptured tube, the fire side showed ferrite– pearlite structure, but the pearlite phase was partially decomposed into ferrite and spheroidal carbides, as shown in Fig.9 (a). The other side of this tube showed normal ferrite-pearlite structure with its lamellar structure as shown in Fig. 9 (b).

Concerning the new tube part, as expected, the structure over all the wall cross-section shows normal ferrite-pearlite structure as shown in Fig. 10.

Survey of hardness measurements through the wall thickness of the received tubes of the ruptured, non-ruptured, and new tubes were carried out and the results are shown in Table 3. Generally, lower hardness values were obtained at the ruptured edges (121HV) compared with 140HV for non-ruptured tube, which confirm the structure deterioration at the ruptured edges.

Table 3. Hardness measurements at different locations at the received tube parts.

locations	Hardness, HV		
	Fracture edges	Fire side	Other side (180 ⁰ from the fracture edges)
Rupture tube	121	128	137
Non-ruptured tube	-	136	139
New tube	-	144	145

The given hardness values are the average of five readings.

For checking the tubes inner-surface-scale-thickness, samples from the tubes cross-section were sectioned, mounted and polished by conventional metallographic methods and shown in the micrographs in Fig. 11. It was clear from these micrographs (Fig. 11) that the inner-surface-scale of the ruptured tube was ranging from 360 μm to 410 μm , while that of the in-service-non-ruptured tube reached 500 μm at the fire side. The inner scale of the ruptured tube was lower than that of the non-ruptured one due to that some of the inner scale of the ruptured tube was broken during tube bursting.

3.2 Discussions

Chemical analysis of all the received tube parts showed that their materials were conformed to ASTM SA213-T2 steel. Visual and macroscopic investigations of the ruptured tube showed large fish-mouth rupture shape with no indications of external corrosion damage. Wall thinning was observed at fire side, especially at the fracture edges. Another important finding is the presence of abnormal thick, layer of iron oxides covering the ruptured tube inner surface, either at or away from fire side. These oxide scale layer reaches 410 μm at the fire side. Visual and macroscopic investigations of the tubes after chemical cleaning showed smooth surfaces without any indications of considerable localized corrosion or pitting.

Unlike expected original microstructure of normal low alloy steel that is ferrite-pearlite structure with lamellar pearlite morphology, optical microscopic examination of the ruptured tube has revealed great microstructural changes especially at the fracture edges. Microstructure of the fracture edges and at its surroundings at the fire side exhibited complete decomposed pearlite structure in addition to voids at grain boundaries, which resulted in deteriorated structure with low hardness values. On the other hand, the other side of the tube shows normal ferrite laminated-pearlite structure even at the fracture location.

These findings increase the possibility that fracture of the received boiler water wall tubes is attributed mainly to **localized overheating damage** at the fire side, where the metal temperatures in this area exceed design limits for days, weeks, months, or longer.

The observed localized structural degradation (complete pearlite decompositions and voids formation) of the received ruptured tube indicated that the tube material at the ruptured area was severely overheated. The relatively normal structure observed at the fire side of the non-ruptured tube confirms the localized overheating in the area at the ruptured tube. This type of localized rupture usually occurred shortly after an unusual set of circumstances such as inhomogeneity distribution of the heat inside the furnace. One of the main causes of the temperature inhomogeneity is the **bad conditions of the fire burners and its related air guides**. Moreover, heavy internal deposition of the oxide scales accelerates the occurrence of the rupture by insulating the tube wall from cooling effects of the water, contributing to overheating. These overheating results in structure degradation (pearlite decompositions and voids formation) of the tube wall thickness.

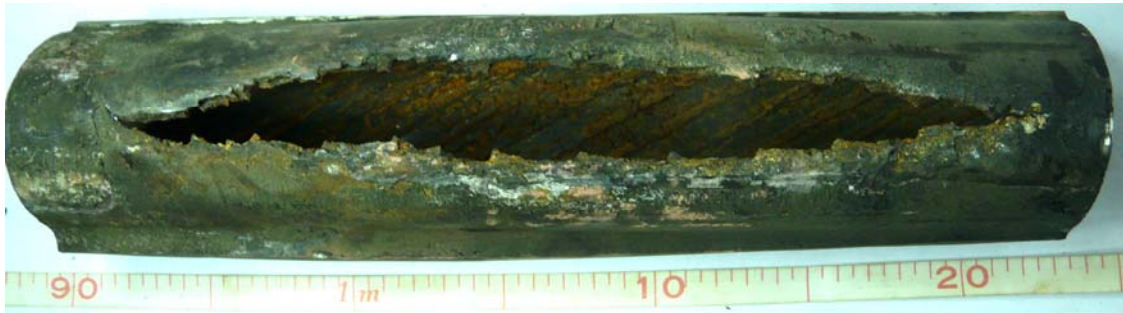
The maximum allowable design temperature is primarily a function of tube metallurgy. So, tube material loses much of its strength at temperatures higher than the designated limits, which results in slow plastic deformation and thickness reduction at these areas. These localized plastic deformation or bulging increases surface area that exposed to heat, allowing a greater metal temperature at these deformed spots than the surrounding metal. Moreover, the localized deformation or bulging changes the tube geometry at these areas, which produces a flow disturbance of the running water to a degree that reduces the water cooling efficiency. This close cycle of temperature raising and deformation continue until the remaining wall thickness can not withstand the internal pressure and rupture or bursting becomes more likely.

3.3 Recommendation

Based on the results obtained in the investigation conducted on the boiler tube, it can be concluded that failure of the ruptured tube could be attributed mainly to localized overheating damage at the fire side of the tube.

To reduce the danger of overheating damage, it is highly recommended to:

- The boiler burners and its related air guides must be checked and the defected one must be repaired or replaced immediately.
- The tubes in the regions of the burners levels should be checked immediately by Ultrasonic thickness meter and sump (replica) test.
- It is strongly recommended that the other tubes should be subjected to detailed investigations including different non-destructive testing to evaluate its condition during the nearest shut down.
- The water wall tubes should be subjected to acid cleaning to remove the heavy internal oxide scales.

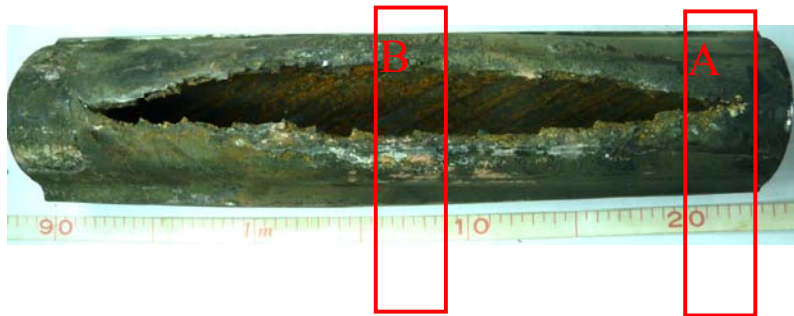


View of the fracture side

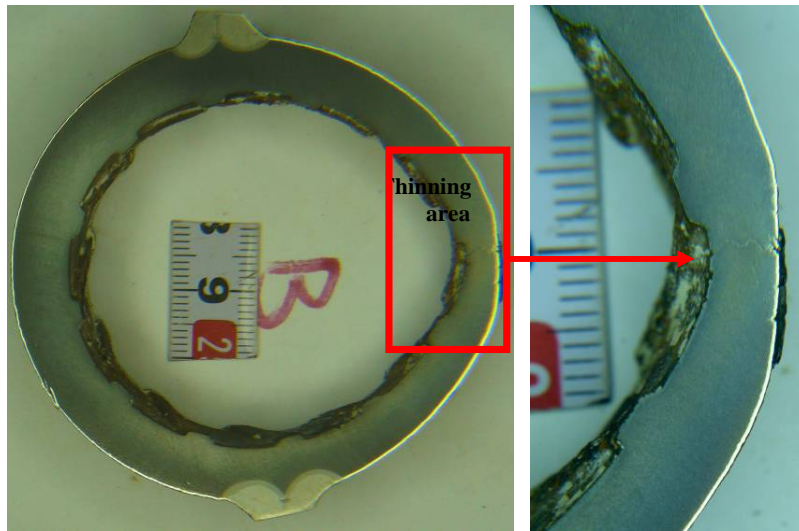
Fig. 1 General views of the received ruptured tube sample.



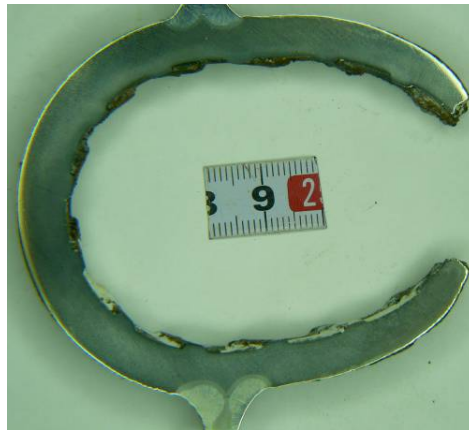
Fig. 2 General views of the received in-service-non-ruptured tube sample.



(a) General view of the received ruptured tube



(b) Views of the ruptured tube cross-section at the beginning of the fracture (section A in (a))



(c) View of the ruptured tube cross-section at the center of the fracture (Section B in (a))

Fig 9 View of the ruptured tube cross-section at different locations showing the tube bad ovality and its thinning at the fire side.

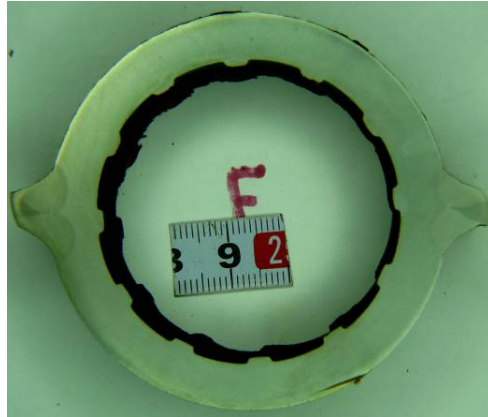
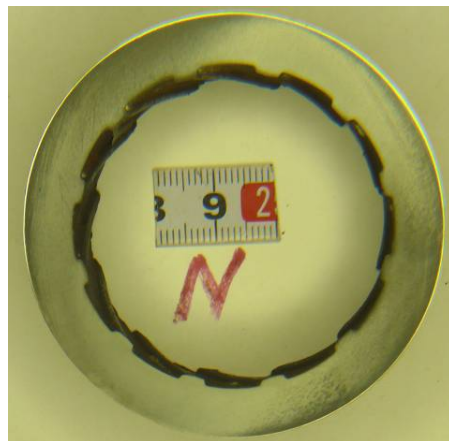


Fig 4 View of the in-service-non-ruptured tube cross-section showing good tube ovality.

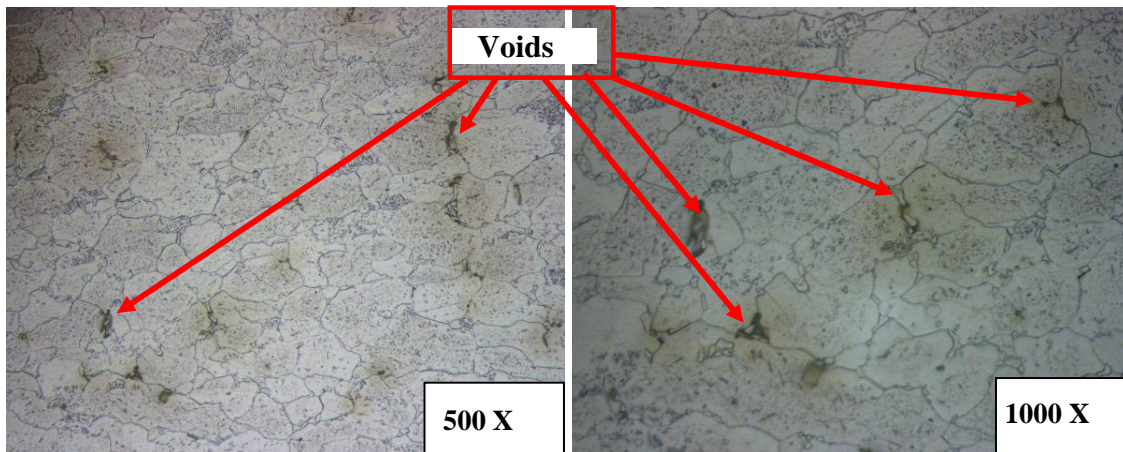
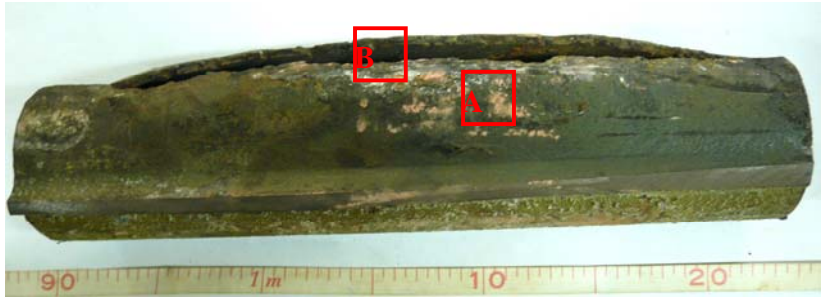


(a) View of the received new tube

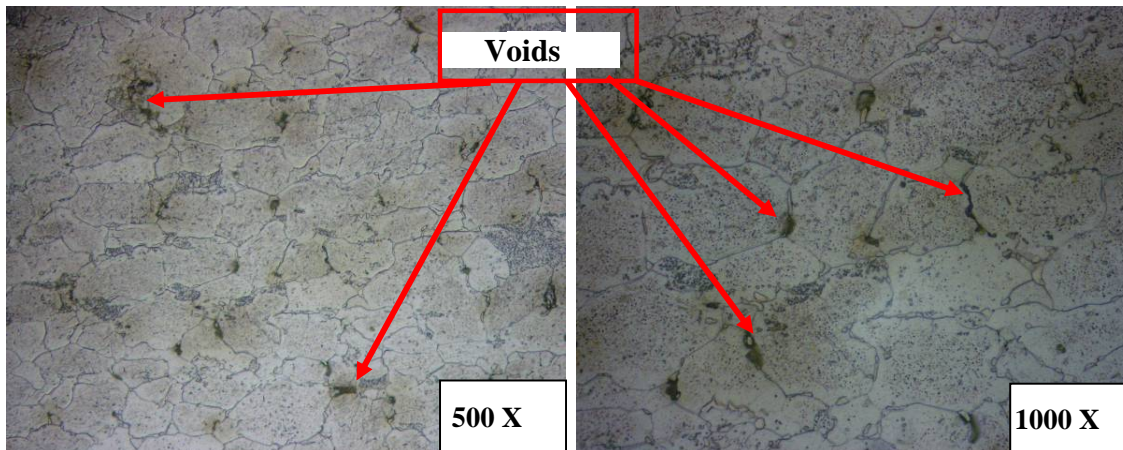


(b) View of the new tube cross-section showing good ovality

Fig. 5 General views of the new tube and its cross-section.

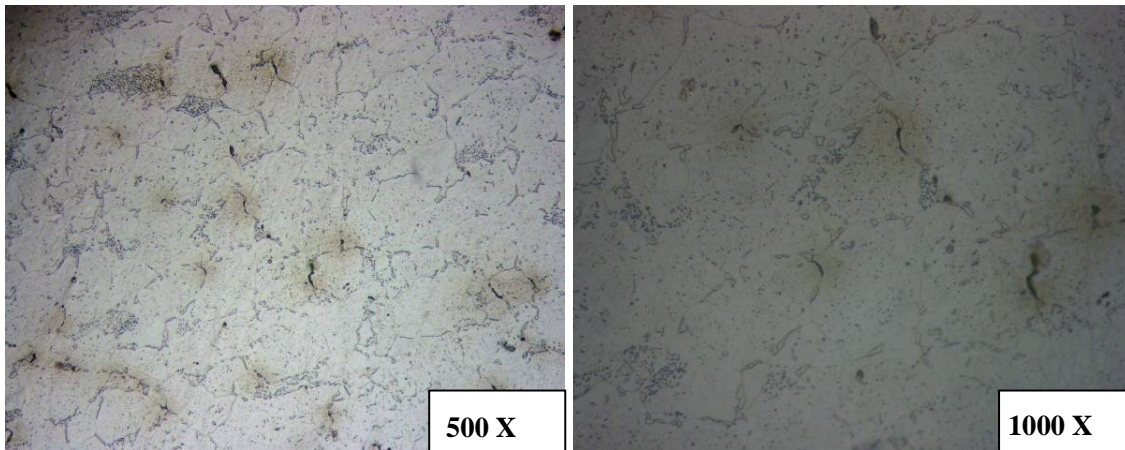


(a) At the fire side (Section A)

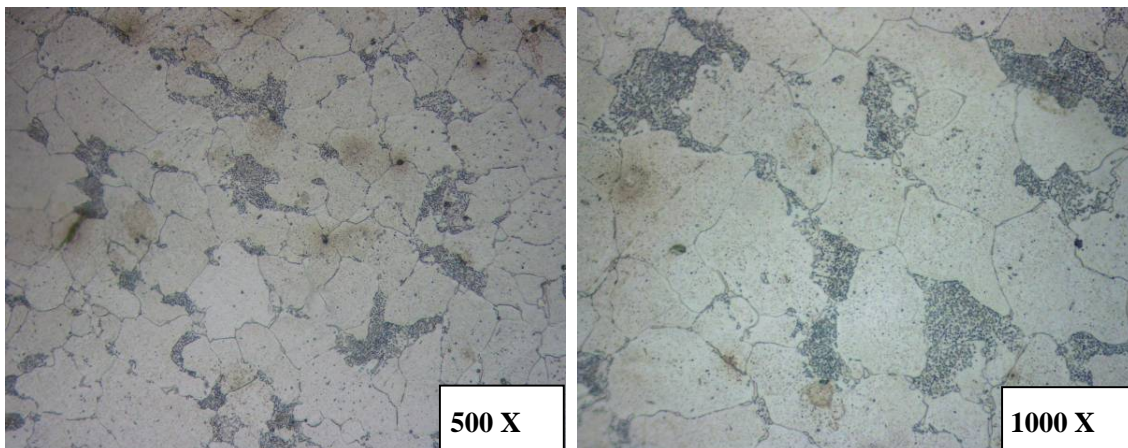


(b) At the fracture edges (Section B)

Fig. 6 Micrographs of the ruptured tube microstructure at the fracture side showing complete deteriorated structure (ferrite+ decomposed pearlite+ grain boundaries voids).

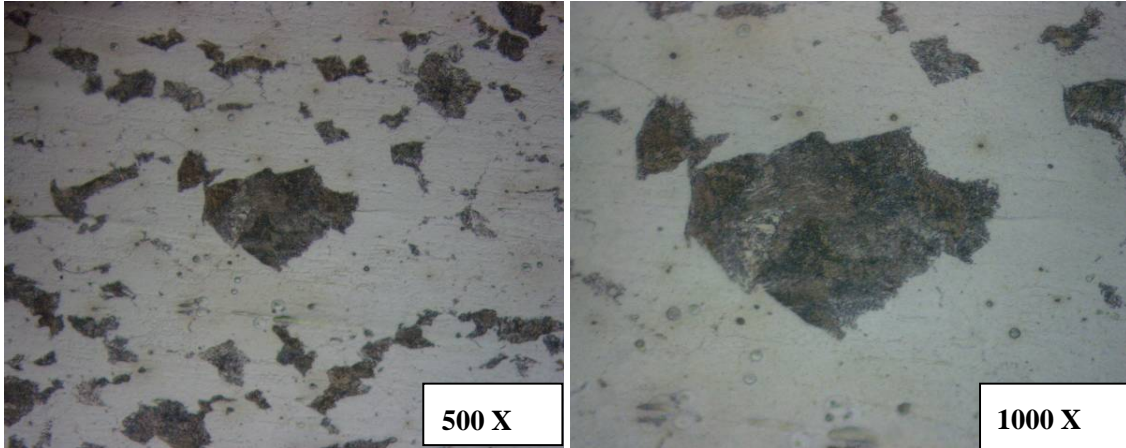


(a) At area before fracture (complete deteriorated structure) (Section A)

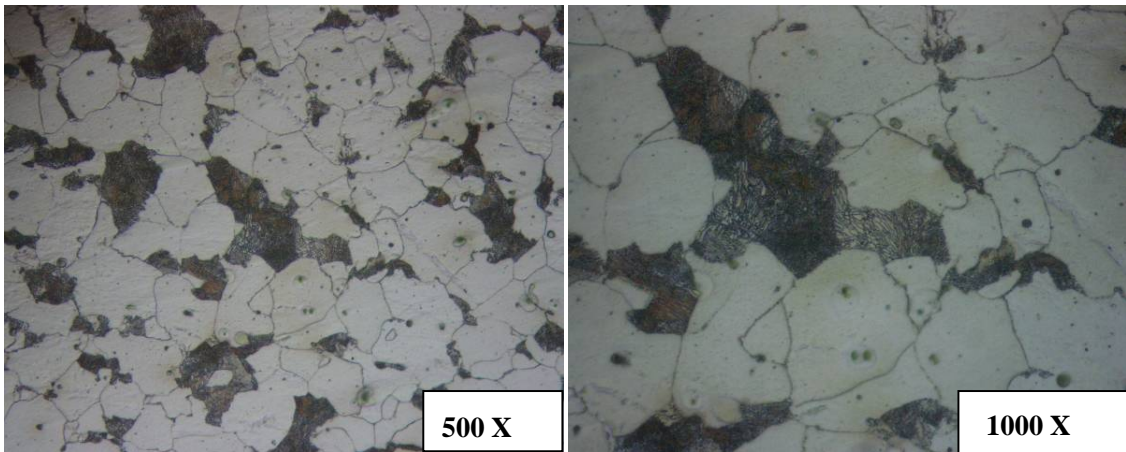


(b) At area 90° from the fracture edges (partial deteriorated structure) (Section B)

Fig. 7 Micrographs of the ruptured tube microstructure at the fire side before fracture showing deteriorated structure at the fracture line and partial deteriorated structure at area far from it.

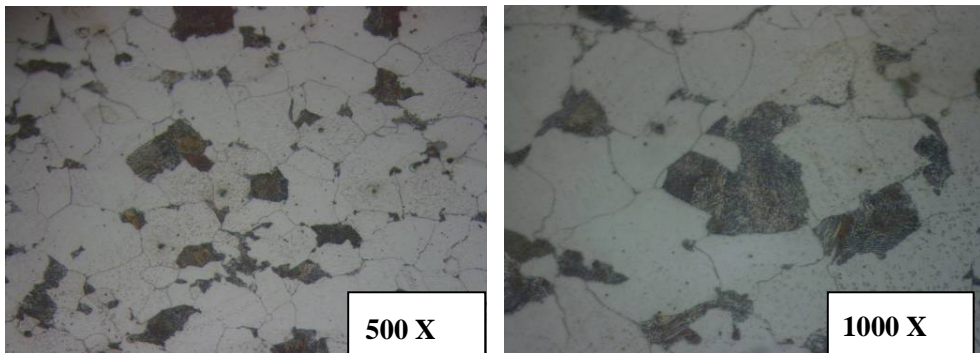


(a) At the fracture area (Section A)

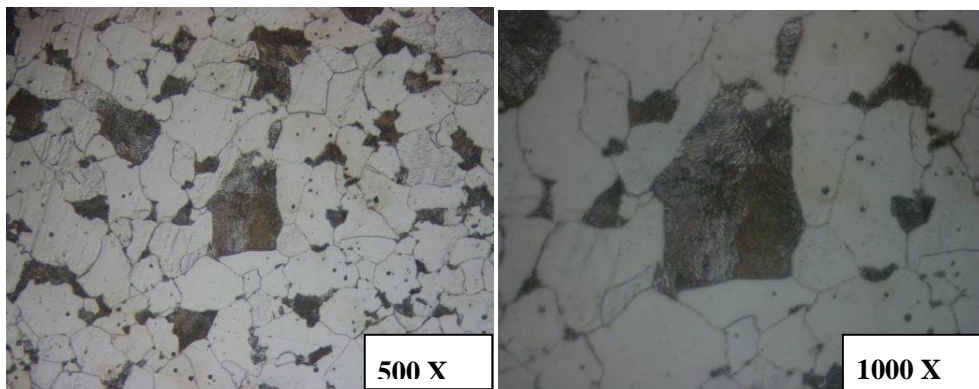


b) At area relatively far from fracture (Section B)

Fig. 8 Micrographs of the ruptured tube microstructure at the other side (180° from the fracture edges) showing normal ferrite (white) – pearlite (grey) structure with lamellar pearlite structure.



(a) At the fire side showing partial deteriorated structure



b) At the other side (180° from the fire side) showing normal structure.

Fig. 9 Micrographs of the in-service-non-ruptured tube microstructure at different locations showing partial deteriorated structure at the fire side and normal ferrite- pearlite structure at the other side.

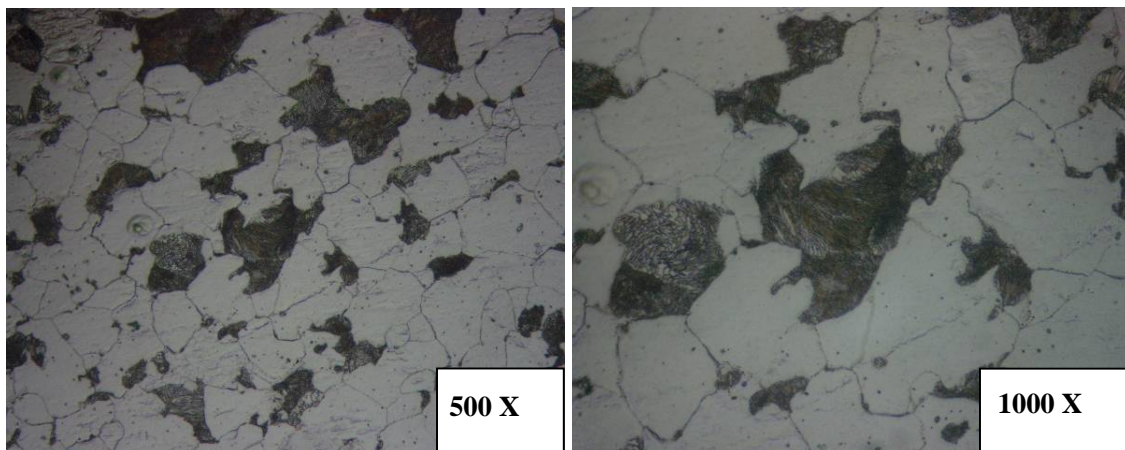
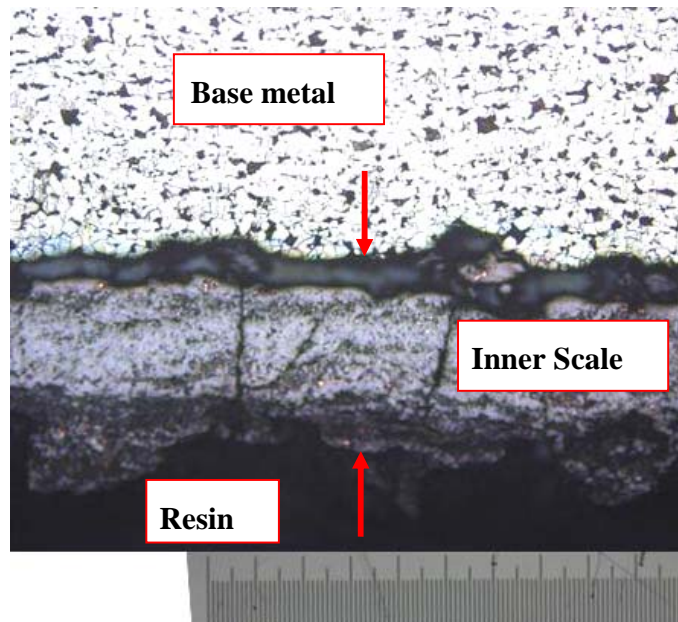
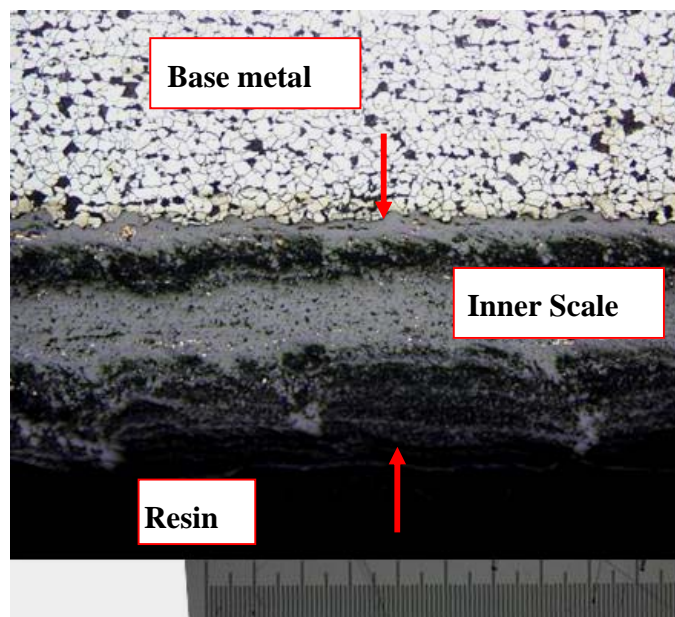


Fig. 10 Micrographs of the new tube microstructure showing normal ferrite- pearlite structure.



(a) Ruptured tube (~410 μm)



(b) In-service-non-ruptured tube (~510 μm)

Fig. 11 Micrographs of the inner side of both ruptured and non-ruptured tubes showing their inner oxide scale.

***AFA WORKSHOP: FITNESS FOR SERVICE IN CHEMICAL
INDUSTRIES***

Aswan, EGYPT

25 - 27 Nov 2012

**Potential for repair welding technology based on
laser metal deposition for petrochemicals industry**

Dr. A. Gumenyuk

**The Federal Institute for Materials Research and
Testing (BAM), Germany**

Laser metal deposition as repair technology for stainless steel and titanium alloys for petrochemicals industry

Benjamin Graf ^{a,*}, Andrey Gumenyuk ^{a,b}, Michael Rethmeier ^{a,b}

^aFraunhofer Institute for Production Systems and Design Technology, Pascalstraße 8-9, 10587 Berlin, Germany

^bBAM Federal Institute for Materials Research and Testing, Unter den Eichen 87, 12205 Berlin, Germany

Abstract

In a repair process chain for petrochemicals industry, damaged areas or cracks can be removed by milling and subsequently be reconditioned with new material deposition. The use of laser metal deposition has been investigated for this purpose. The material has been deposited into different groove shapes, using both stainless steel and Ti-6Al-4V which are widely used in petrochemicals industry. The influence of welding parameters on the microstructure and the heat affected zone has been studied. The parameters have been modified in order to achieve low heat input and consequently low distortion as well as low metallurgical impact. Finally, an evaluation of the opportunities for an automatized repair process is made with the aim of future application in petrochemicals industry.

Keywords: laser metal deposition; laser powder cladding; repair welding; Ti-6Al-4V; stainless steel

1. Motivation / State of the Art

The demand on repair welding technology based on mobile automatic welding process is especially high in petrochemical industry where the risk of damage during the service of the components being in contact with corrosive media and/or operating at elevated temperatures and pressures increased with increasing their lifetime. Compared to conventional repair welding technologies like tungsten inert gas or gas metal arc welding [2], laser metal deposition allows material deposition with multiple advantages. Its low heat input leads to low distortion and low thermal damage in the base material. Furthermore, smaller dilution and a finer microstructure can be achieved. The stable and repeatable energy input of the laser beam grants a high reproducibility of the material deposition and in the same time high degree of the process flexibility because of extremely small size of the weld pool and compactness of the welding head. In combination with beam delivery systems used optical fiber these provide broad possibilities for robot based applications. All mentioned factors contribute to a high reliability and the opportunity to automate the processes.

In recent years, the relevance of laser metal deposition as an innovative repair technology is continuously increasing. Laser metal deposition allows creating a metallurgical bonded material deposition on a substrate. The current state of laser metal deposition is described in [1].

The laser beam of a CO₂ or a solid state laser is used as heat source. The filler material is either fed in by wire or by a powder injected into the molten pool by nozzle [3, 4]. Powdery filler material has higher flexibility regarding the chemical composition as well as better accessibility. The powder feed is included in the inert gas nozzle, allowing for directional independent powder delivery.

Laser metal deposition has been established in several industrial applications for 12 years. It is typically used for hard facing or repair purposes, namely the repair of damaged surfaces. Examples are found in the mould and die industry. Laser metal deposition is used to repair sintered tools [5] or deposit vanadium-carbide tool steels for die repair [6]. However, in a repair process chain that consists of milling the damaged part and consecutive rebuilding by new material deposition, the use of laser metal deposition has rarely been studied. This repair process chain is needed for the repair of casted or welded products having intolerable defects like voids or cracks inside the material.

Commercially pure titanium and titanium alloys as well as different grades of stainless steels are widely used in chemical and petrochemical industries because of their excellent corrosion resistant properties. The application of laser cladding process for processing of stainless steels was studied in [7,8]. The use of Ti-6Al-4V in laser metal deposition considered in [9, 10]. The aim of this paper is to show the feasibility of laser metal deposition for re-filling milled grooves and therefore its feasibility for new repair applications on example of some stainless steels grade and titanium alloys used in chemical and petrochemical industry.

2. Experimental

2.1. Specimen preparation

Specimens with three different groove shapes were prepared by milling. In this case-study it was assumed that intolerable defects extend not deeper than 10 mm from the surface, therefore a groove depth of 10 mm was chosen. Acetone was used to clean the groove after milling. The specimens differ in the necessary volume that has to be filled and in the accessibility for the laser beam and the powder jet. The specimens are shown in figure 1.

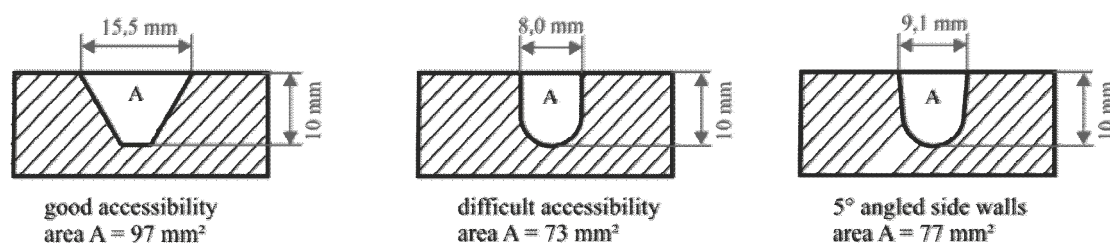


Fig. 1. Specimen: a) V-groove; b) U-groove; c) U-groove with angled side walls

2.2. Laser metal deposition

The metal deposition was conducted using a TRUMPF TruDisk 2.0 kW Yb:Yag laser, figure 2. Powdery filler material was injected in the melt pool by a 3-jet powder nozzle that was positioned with a 5-axis machine. Helium 5.0 was used as carrier gas for the powdery filler material. Argon 5.0 was used as

shielding gas, creating a local inert gas atmosphere with less than 50 ppm oxygen. The materials used included stainless steel and the titanium alloy Ti-6Al-4V, both as base material and as filler material. Powder grain size between 45-125 μm has been used.

The metal deposition was done layer by layer. Each layer is made by welding multiple adjacent tracks. After each layer, the powder nozzle was elevated a defined distance, in order to build a three dimensional deposition consecutively.



Fig.2 Equipment for laser metal deposition with 2kW disc laser

The welding parameters are shown in Table 1. The optical system is able to change the focal length and consequently the laser spot diameter on the substrate within a range of 0.6 mm to 2.2 mm. The maximum spot size of 2.2 mm is used to deposit big tracks, while smaller spot sizes are used for smaller tracks with faster cooling times. The parameters for titanium alloy have first been tested on the flat surface of the specimen, with a trailing inert gas nozzle in case a) and without it in case b). Then the parameters b) were used for rebuilding the groove in the titanium alloy.

After visual inspection, the welding results have been analyzed by cross sections, microscopy, x-ray testing and hardness measurement. The powder efficiency was obtained by comparing the overall injected powder mass to the increase of the mass of the specimen before and after welding.

Table 1. Welding parameters

Welding parameters	V-groove 1	V-groove 2	U-groove	a) Ti	b) Ti
Welding velocity	0.5 m/min	1.0 m/min	1.0 m/min	0.5 m/min	1.0 m/min
Laser power	1.0 kW	1.0 kW	1.0 kW	2.0 kW	1.0 kW
Laser spot diameter on surface	2.2 mm	2.2 mm	2.2 mm	2.2 mm	1.0 mm
Powder mass flow	4.0 g/min	8.0 g/min	8.0 g/min	9.4 g/min	3.8 g/min
Material	CrNi-Steel	CrNi-Steel	CrNi-Steel	Ti-6Al-4V	Ti-6Al-4V

3. Results and Discussion

3.1. CrNi-Steel

Cross sections of the welded specimen are shown in figure 3. In the V-groove 1 and 2 no cracks could be detected in the cross section or X-ray testing (Fig. 4). The V-grooves show good side-wall fusion. Due to the lower welding velocity, the single tracks in V-groove 1 are bigger and the overall number of tracks needed is lower. But due to the low welding velocity, the overall heat input is around 50 % higher. Therefore, a higher distortion must be expected. In order to increase the productivity, a short operation time is intended. In this regard the parameters used for V-groove 2 are advantageous. The high welding velocity of 1.0 m/min leads to a shorter operating time, even though 150 tracks are needed compared to 118 tracks in V-groove 1.

The cross-section of the U-shaped groove (Fig. 3c) shows defects at the side-wall of the groove. Because of accessibility issues, the laser beam couldn't be adjusted perpendicular to the side-wall, resulting in irregular material deposition. Part of the powder jet was impeded by the upper lip of the groove, causing irregularities in the powder stream close to the groove side-walls. In this region, the safe deposition of powder is hindered. Wider grooves or inclined side-walls are necessary.

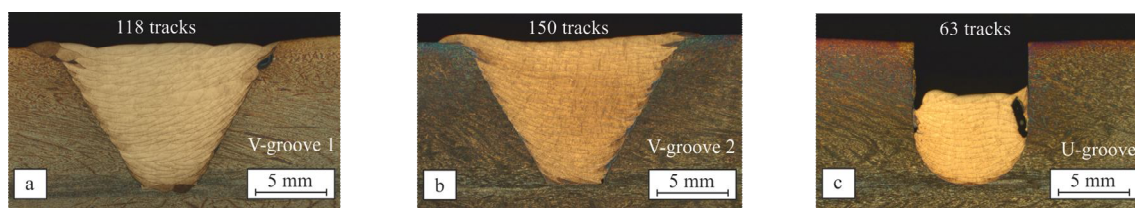


Fig. 3. Cross sections and X-ray testing, stainless steel,

a) $v = 0.5 \text{ m/min}$, $P = 1.0 \text{ kW}$; b) $v = 1.0 \text{ m/min}$, $P = 1.0 \text{ kW}$; c) $v = 1.0 \text{ m/min}$, $P = 1.0 \text{ kW}$

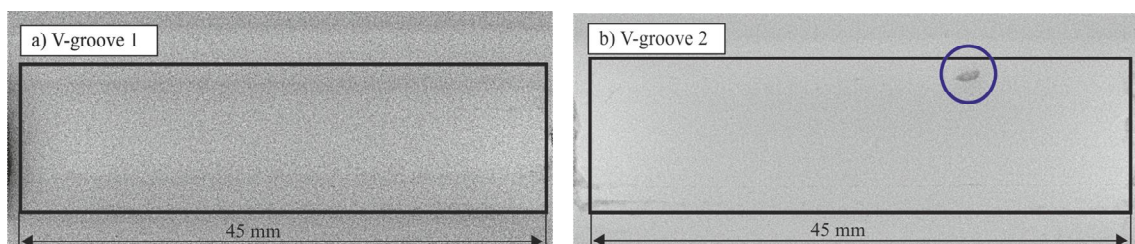


Fig. 4. X-ray testing, stainless steel, a) $v = 0.5 \text{ m/min}$, $P = 1.0 \text{ kW}$; b) $v = 1.0 \text{ m/min}$, $P = 1.0 \text{ kW}$

The x-ray testing shows no cracks (Fig. 4). In V-groove 2 one void is visible. Overall, the x-ray test proves the good quality of the repair welding result. The powder efficiency for V-groove 1 and 2 was measured with 78 % and 75 %. The high efficiency is due to the used maximum laser spot size. While the powder jet spot size is unchangeable, a larger laser spot can cover a bigger portion of the powder spot and therefore melt more of the injected powder.

3.2. Titanium alloy Ti-6Al-4V

Besides the influences of the welding parameters on microstructure and overall heat input, for titanium alloys the cooling time is an important factor. Smaller tracks have faster cooling times, which leads to smaller grain sizes. Furthermore, faster cooling times facilitate the shielding gas coverage. Because of the high affinity of titanium alloys to atmospheric gases like oxygen, nitrogen and hydrogen, the demands for the shielding gas coverage are very high. An additional trailing inert gas nozzle might be needed in order to cope with these demands. But additional nozzles are difficult to use in modern repair tasks of varying and complex parts, because of the accessibility and different welding positions. Therefore if the deposited tracks cool down fast enough, the use of an additional inert gas nozzle might be avoided. Instead, the gas flow of the powder nozzle is enough to protect the titanium alloy from reaction with atmospheric gases.

Figure 5 shows the influence of the welding parameters on the track size. It is possible to use low welding velocity and a high laser power to get single tracks with a height of about 2 mm (Fig. 5a). But due to slow cool down times, an additional inert gas nozzle was needed. The cross section b) shows smaller track sizes that were deposited with only one fourth of the energy input per unit length. No additional inert gas nozzle was used. Between the different layers, no heat tint was observed.

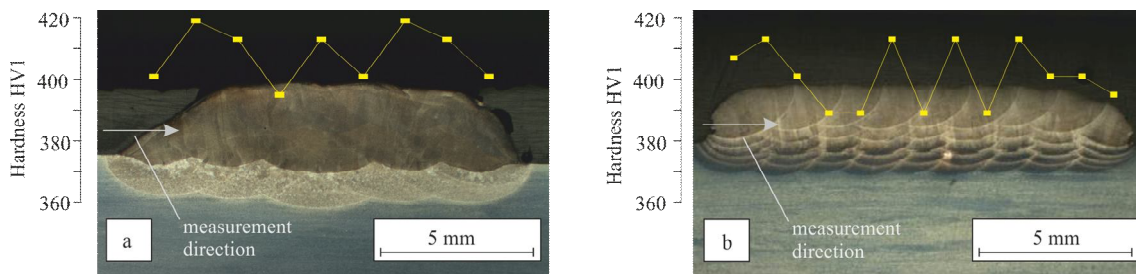


Fig. 5. Cross sections and hardness measurement of titanium alloy Ti-6Al-4V; a) $v = 0.5$ m/min, $P = 2.0$ kW; b) $v = 1.0$ m/min, $P = 1.0$ kW

The hardness HV1 in the weld bead is averaged 408 HV1 (Fig. 5a) and 401 HV1 (Fig. 5b). No significant difference in the hardness of the weld with trailing inert gas nozzle (Fig. 5a) and the weld without it (Fig. 5b) is apparent. It can be concluded that the inert gas atmosphere was sufficient, there was no increased hardness due to reaction with atmospheric gases.

Cross sections of the rebuilt grooves are shown in figure 6. Due to varying angles and positions of the powder nozzle, it is not possible to use a trailing nozzle for creating an inert gas atmosphere in the groove base and along the side walls. Therefore the welding parameters from figure 6 b) with a low energy input per unit length were used. Both grooves show good side-wall fusion. The U-groove shape with a 5° angled side wall was used based on the results obtained with steel and straight walls (Fig. 3c). The angled side-wall leads to better accessibility for the powder jet. Furthermore, the deposition strategy was improved. In each layer, the tracks on the left and right side wall were done first; subsequently the material was deposited in the middle of the groove.

The powder efficiency was measured with 72 % for both specimens. Although the used laser spot diameter of 1.0 mm is smaller than the diameter used with steel (2.2 mm), the powder efficiency is comparable. Part of the powder not molten in the process the first time is distributed in the groove base and molten in the weld process for the next layer. Too much residual powder in the groove base will affect the welding process in a negative way, but that was not an issue in the conducted experiments. There was no need to manually remove residual powder out of the groove base.

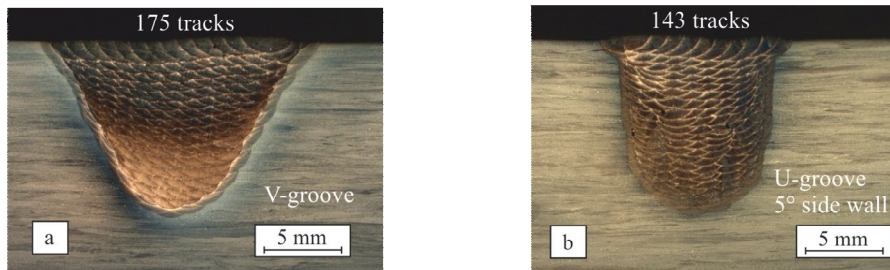


Fig. 6. Cross sections of rebuild grooves, titanium alloy, $v = 1.0$ m/min, $P = 1.0$ kW

3.3. Automated deposition strategy

In order to get an automated filling process, the following deposition strategy was used. It is designed to use constant offsets between layers and tracks:

- Consecutive layers are always deposited in the same height difference
- Adjacent tracks use the same overlap distance
- Nozzle inclination for side wall fusion
- Material deposition along the side walls first, followed by the middle of the groove

Small deviations in the track size add up and may lead to irregularities that require manual adjustment of the deposition strategy. This could mean adjusting the normally fixed elevation of the powder nozzle for consecutive layers, or adding in additional tracks to level unevenness. Due to the good reproducibility of welding results in laser metal deposition, it is possible to weld multiple layers without manual adjustment. Based on the low variance of the welding results observed in the conducted experiments, the deposition strategy is appropriate for an automated repair process.

4. Conclusions

This article has analyzed the feasibility of laser metal deposition for re-filling milled grooves for repair applications. Stainless steel and a titanium-alloy were used. Different U- or V-groove shapes were rebuilt without defects and good side-wall fusion, as long as the groove is wide enough for good powder jet accessibility. Titanium alloy could be deposited without an additional trailing inert gas nozzle, using low heat input leading to short cooling times. No heat tint or increased hardness was observed.

A deposition strategy was developed that leads to the deposition of defect-free layers without manual adjustment. Laser metal deposition therefore shows a high potential for an automated repair process.

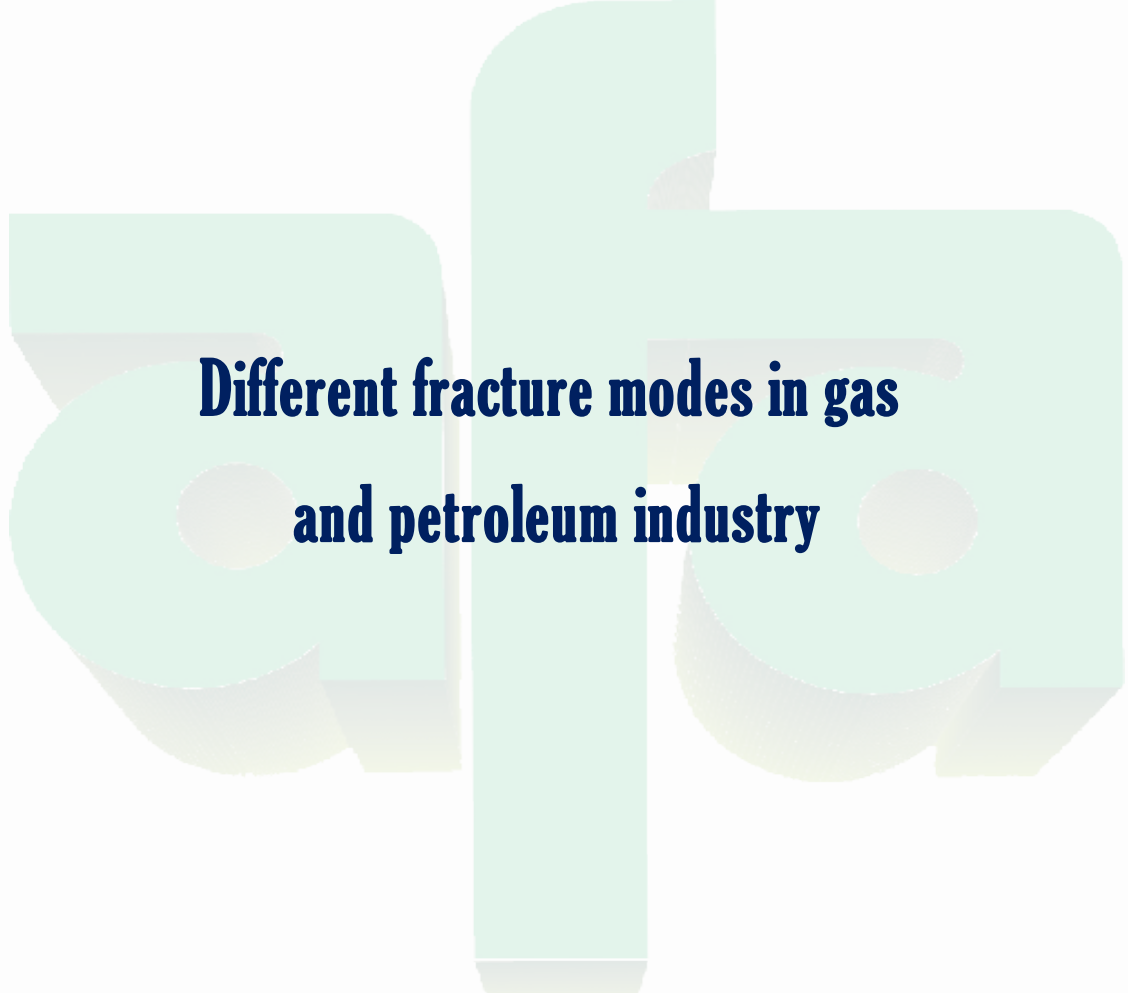
References

- [1] Birger, E.M.; Moskvitin, G.V.; Polyakov, A.N.; Arkhipov, V.E.: Industrial laser cladding: current state and future. In: *Welding International*, Vol. 25 No. 3 (2011), 234-243
- [2] Lant, T.; Robinson, D.L.; Spafford, B.; Storesund, J.: Review of weld repair procedures for low alloy steels designed to minimise the risk of future cracking. In: *Int. J. Pressure Vessels Piping*, 11-12 (2001), 812-818
- [3] Capello, E.; Previtali, B.: The influence of operator skills, process parameters and materials on clad shape in repair using laser cladding by wire. In: *J. Mater. Process. Technol.*, 174 (2006), 223-232
- [4] Sexton, L.; Lavin, S.; Byrne, G.; Kennedy, A.: Laser cladding of aerospace materials. In: *J. Mater. Process. Technol.*, 122 (2002), 63-68
- [5] Capello, E.; Colombo, D.; Previtali, B.: Repairing of sintered tools using laser cladding by wire. In: *J. Mater. Process. Technol.*, 164-165 (2005), 990-1000
- [6] Leunda, J.; Soriano, C.; Sanz, C.; Garcia Navas, V.: Laser Cladding of Vanadium-Carbide Tool Steels for Die Repair. In: *Physics Procedia*, 12 (2011), 345-352
- [7] Song, J.; Deng, Q.; Chen, C.; Hu, D.; Li, Y.: Rebuilding of metal components with laser cladding forming. In: *Applied Surface Science*, 252 (2006), 7934-7940
- [8] Pinkerton, A.; Li, L.: Multiple-layer cladding of stainless steel using a high-powered diode laser: an experimental investigation of the process characteristics and material properties. In: *Thin Solid Films* 453-454 (2004) 471-476
- [9] Yuwen, S.; Minghong, H.: Statistical analysis and optimization of process parameters in Ti6Al4V laser cladding using Nd:YAG Laser. In: *Optics and Lasers in Engineering*, 50 (2012), 985-995
- [10] Suáreza, A.; Tobará, M.J.; Yáñez, A.; Pérez, I.; Sampedro, J.; Amigó, V.; et al.: Modeling of phase transformations of Ti6Al4V during laser metal deposition. In: *Physics Procedia*, 12 (2011), 666-673

***AFA WORKSHOP: FITNESS FOR SERVICE IN CHEMICAL
INDUSTRIES***

Aswan, EGYPT

25 - 27 Nov 2012



**Different fracture modes in gas
and petroleum industry**

Prof. A. El-Batahgy

CMRDI, Egypt

***AFA WORKSHOP: FITNESS FOR SERVICE IN CHEMICAL
INDUSTRIES***

Aswan, EGYPT

25 - 27 Nov 2012



**Materials selection and reliability for aggressive
services in the fertilizer industry**

Dr. A. Asphahani

University of Akron, Ohio-ASM Materials Education

Foundation-USA

Arab Fertilizer Association Workshop
Aswan, Egypt
November, 2012

Materials Selection and Reliability for Aggressive Services in the Fertilizer Industry

Dr. Aziz Ibrahim Asphahani

Senior Advisor-Corrosion Program / University of Akron, Ohio-USA
ASM Materials Education Foundation-USA

ABSTRACT

Materials reliability, performance enhancement and life-cycle costing represent important issues to Design, Engineering, Operations, Management and Maintenance personnel in the Chemical Industries. The use of high-performance alloys to improve operations, guarantee fitness for service, ensure reliability and extend service life of process equipment is fast becoming a practical, cost-effective answer.

Advances in materials science and engineering, coupled with understanding the characteristics of materials degradation/corrosion problems led to the formulation of “specialty” corrosion-resistant alloys. These high-performance alloys were evaluated and effectively implemented in aggressive services in various chemical processing industries.

The factors affecting corrosivity in chemical processing, and specifically in wet phosphoric acids (e.g., concentration, temperature, impurity) and the role of alloying elements (e.g., chromium, molybdenum, tungsten, copper) are discussed. Steps are described, illustrating the development of “tailor-made” materials to provide simultaneously excellent corrosion resistance and reliable, cost-effective equipment in chemical processing (with specific example for the production of “super-phos” acid for the fertilizer industry).

Comparative corrosion/performance data and cost-effectiveness with other alloys are tabulated. Field trials and successful applications at various plants are presented.

INTRODUCTION

For years, in the chemical processing industries (CPI), nickel-based alloys have been depended upon to handle corrosive streams. Also, the cobalt-based alloys have been essential to minimize degradation due to wear.

While some noble, refractory metals (e.g., Ta, Cb, Ti, Zr) and their alloys offer excellent resistance to several corrosive media, these materials fail to provide the versatility of nickel-based alloys, especially when fluoride ions are present in process streams. Also many of these refractory metals often do not permit practical field repairs. In contrast, the nickel-based alloys are well known for their excellent weldability characteristics which have augmented their acceptance as the best, economical choice for solving severe/chronic corrosion problems.

Similarly, many steels are often inadequate in severe wear conditions; and ceramic alternatives are too brittle to provide a reliable performance. The cobalt-based alloys are well known for their outstanding resistance to various forms of wear (e.g., erosive, adhesive, abrasive) and have been used extensively in a multitude of industrial services.

Conventional corrosion-resistant materials (e.g., stainless steels) and protective measures (e.g., coatings, inhibitors) were often selected on the basis of initial cost and perceived efficiency in the intended design. However, the unsatisfactory performance of such conventional approaches is becoming an increased liability to plant operations. Recurring maintenance shutdowns and unscheduled downtimes are leading to a greater emphasis on cost reduction as well as causing real concerns about the reliability of equipment and the safety of personnel. Such emphasis and concerns are the driving force behind the search by plant corrosion engineers for the correct choice of materials of construction. As such, the uniqueness of nickel-based and cobalt-based alloys in providing combinations of excellent mechanical and corrosion/wear properties is the reason for the increased demand for these high-performance alloys in CPI aggressive/critical services.

It is the purpose of this paper to describe advanced nickel-based products: HASTELLOY C-22 alloy and HASTELLOY G-30 alloy, and a new cobalt-based product: ULTIMET alloy. The factors affecting corrosion and the role of alloying elements are reviewed. Field trips and successful applications in various industrial services are cited, with specific case histories illustrating the performance of these advanced alloys.

C-22 ALLOY

Of the Ni-Cr-Mo-W system, HASTELLOY alloy C was the prominent alloy during the 1940s to 1960s ^[1]. Many developments in melting and processing practices have been made since the original implementation of alloy C (oxygen blowing of heats

made it possible to reduce the carbon content of alloy C to a nominal 0.05 wt. %). With such development, it became feasible to have large-scale wrought production of the alloy. However, grain boundary precipitation of carbides in the as-welded condition was known to promote intergranular corrosion. This required a post-weld solution heat-treatment to dissolve the carbides and restore the corrosion resistance of the alloy. Such heat-treatment was a cumbersome operation, especially with large process equipment.

The detrimental role played by the relatively high carbon and silicon contents led researchers at BASF^[2] to identify alloy C-type with 0.01 wt. % C maximum and 0.08 wt. % Si maximum. The advent of the argon-oxygen-decarburization (AOD) process then made this theoretical alloy C-276 a commercial reality.

Despite its excellent corrosion resistance, alloy C-276 was not completely free of preferential weld and heat-affect zone attack due to precipitation of Mo- and W-rich intermetallic phases^[3]. The electron vacancy number (N_v) of alloy C-276 had not been controlled and, as a consequence, the alloy became susceptible to formation of intermetallic compounds of the mu-phase type when exposed to temperatures in the range of 650-1100°C.

Even though alloy C-276 possessed versatile corrosion resistance, it exhibits limited resistance to oxidizing acid environments. In addition, alloy C-276 has impaired thermal stability due to mu-phase precipitation. Better understanding of the specific roles of chromium, molybdenum, and tungsten in imparting corrosion resistance to the nickel-base alloys has led to a new generation of this versatile Ni-Cr-Mo-W family, C-22 alloy^[4]. The chemistries of C-276 and C-22 alloys, along with that of another Ni-Cr-Mo alloy (alloy 625) are listed in Table 1.

The criticality of the proper amounts of chromium, molybdenum, and tungsten in C-22 alloy is due to the fact that in reducing acids, molybdenum, and tungsten are beneficial additions for uniform and intergranular corrosion resistance. Molybdenum and tungsten, however, are ineffective additions for uniform corrosion resistance in oxidizing acid environments. The role of chromium is just the opposite of that of molybdenum and tungsten. That is, chromium is ineffective in reducing acids^[5] and beneficial in oxidizing acids. In view of these concepts, a logical basis for comparison of corrosion resistance of the various compositions is an atomic percent factor (APF) that reflects the opposing role of chromium atoms to those of molybdenum and tungsten. The atomic weights of the elements involved are: chromium-52; molybdenum-96; and tungsten-184. It can be seen that tungsten is approximately twice as heavy as molybdenum and four times heavier than chromium. Therefore, the atomic percent factor is defined as the ratio of four times the chromium weight percent over the sum of twice the molybdenum weight percent and the tungsten weight percent [APF=4Cr/(2Mo+1W)].

In oxidizing environments, such as nitric acid and sulfuric acid plus ferric sulfate (ASTM G-28A), the higher the chromium content (the higher the APF), the lower are the corrosion rates. On the other hand, in reducing environments such as boiling hydrochloric acid and dilute sulfuric acid, the higher the molybdenum and tungsten contents (the lower the APF), the lower are the corrosion rates.

The ultimate versatility providing the best resistance to both oxidizing and reducing environments is achieved by the careful adjustment of alloying elements to yield an APF factor in the range of 2.5 to 3.3 (Figure 1). C-22 alloy lies within this range identified for the lowest corrosion rates in oxidizing and reducing environments.

In addition, the C-22 composition of 22Cr-13Mo-3W-3Fe shows a much improved thermal stability over that of 16Cr-16Mo-4W in alloy C-276. Intergranular corrosion is observed in alloy C-276 within less than two minutes of aging at 928°C, while C-22 alloy remains resistant to such intergranular attack, even after aging at the same temperature for up to 15 minutes ^[6].

C-22 alloy has undergone an extensive evaluation program. Since its inception, the alloy has been subjected to a multitude of laboratory tests, resulting in a large body of corrosion data. When tested for resistance to uniform corrosion, C-22 alloy outperformed alloys C-276 and 625 by consistently showing the lowest corrosion rates in a variety of oxidizing mixed acid media (Table 2). Also, C-22 alloy exhibited the lowest corrosion rates of several Ni-Cr-Mo-W alloys when tested in reducing dilute hydrochloric acid and sulfuric acid (Table 3).

Initially, it was thought that the improvements in uniform corrosion rates would be achieved at the expense of resistance to pitting and crevice corrosion. However, the resistance to such forms of localized attack was actually improved. C-22 alloy showed the best resistance to pitting and to crevice corrosion attack, as characterized by the critical temperatures above which pitting or crevice corrosion occurs ^[7]. It is presumed that in terms of localized corrosion properties, the increase in chromium content in C-22 alloy has more than compensated for the slight reductions in molybdenum and tungsten contents, as compared to those of alloy C-276.

As for its resistance to stress corrosion cracking (SCC), C-22 alloy showed the best performance of the commonly used alloys, C-276 and 625 (Table 4). While alloy C-276 is considered to be the most resistant alloy to SCC in hot deep sour gas environments, C-22 alloy outperformed alloy C-276 in the accelerated laboratory tests. Also (as shown in Table 5), C-22 alloy offered better resistance to hydrogen embrittlement than alloy C-276 ^[8].

Finally, the sought-after improvement in resistance to heat-affected zone attack and degradation of weldments was achieved with the 22Cr-13Mo-3W-3Fe composition of C-22 alloy. This alloy showed better resistance than alloy C-276 (Figures 2) in various corrosion tests conducted in various laboratories in the USA, Japan ^[9], and West Germany ^[10]. Preferential attack of heat-affected zones or weldments in aggressive environments is caused by selective dissolution of Mo- and W-rich intermetallic and carbide phases (or their adjacent depleted zones). The reduction of Mo and W content in C-22 alloy versus alloy C-276 is responsible for improving the thermal stability of the alloy and thus its enhanced resistance to corrosion in the as-welded condition.

G-30 ALLOY

The G-30 alloy was specifically developed to provide improved resistance to corrosion in aggressive, wet process phosphoric acid ^[11]. Even through many variables play a role in the corrosiveness wet process phosphoric acids, years of experience with metallic materials (Table 6) have helped establish trends that identify the beneficial effects of some alloying elements. Knowing that the wet phosphoric acid process streams might reflect oxidizing acid conditions containing traces of sulfuric acid, alloying with 30% chromium along with 1 to 2% copper became necessary (Table 7). Also, since the

process streams involve halide ions (fluorides and chlorides), the 30% Cr alloys with no molybdenum (such as alloy 690) have proven inadequate (Table 8). Further, the synergistic effect of adding tungsten to molybdenum-containing alloys highlights the need for 2 to 3% tungsten along with the 4 to 6% molybdenum (Table 9). With the addition of 10 to 20% iron to reduce costs, a nominal composition of 30Cr-15Fe-5Mo-2.5W-1.5Cu is identified for the G-30 alloy.

The thermal stability and sensitization resistance to heat-affected zone attack are of great concern in welding. The thermal stability is described by the rates of the precipitation reactions whereas sensitization involves not only the types and amounts of precipitates, but also the depleted zones associated with the precipitates. In the G-type alloys a variety of precipitation reactions occur, depending on the levels of chromium, molybdenum, carbon, and columbium. The effect of these precipitation reactions on the intergranular attack is identified by the corresponding corrosion rates. Intergranular corrosion is observed in a lower chromium containing alloy (alloy G-3) within less than one minute of aging at 870°C, while G-30 alloy remains unaffected at approximately 10 minutes of aging at the same temperature ^[12].

It is presumed that even though carbide precipitation kinetics in these two alloys are approximately the same, the depleted zones in G-30 alloy remain higher in chromium than those in alloy G-3 and hence G-30 alloy suffers less intergranular attack. However, it should be noted that the higher Cr in G-30 alloy might enhance the formation of sigma phase at high temperatures (870 to 980°C), which also leads to depleted regions and to selective dissolution. Also, the presence of higher Nb in G-30 alloy (0.7%) than in alloy G-3 (0.3%) might lead to precipitation of A₂B –type Laves phase in the former (A = Fe, Ni; B = Nb, Mo, W). Since this phase is low in Cr, preferential corrosion can occur along this phase. The time involved in all precipitation reactions in G-30 alloy is long compared to practical thermal cycles encountered in welding. The effect of welding on corrosion rates of G-30 alloy in 20% HNO₃+6% HF solution is virtually nil ^[12]. No heat-affected zone corrosion attack was observed in the welded test pieces using either Gas Tungsten Arc or Gas Metal Arc Welding techniques.

In phosphoric acid service, there is no single standard method for carrying out corrosion tests. The choice is determined by the nature of the material to be tested and the intended use ^[13]. Laboratory tests can be expected to provide only a rough guide for the performance of specific materials in actual plant operation. Also, these tests are a practical way to obtain comparative information on the performance of different materials. Typically, the corrosion resistance of different alloys can be compared in terms of average corrosion rates. However in wet-process phosphoric acids, the corrosion rates of metallic materials from “similar” tests (such as same acid concentration, but from different plants/producers) often vary substantially. An average corrosion rate may not be indicative of the alloy’s suitability for corrosive services. The new, improved G-30 alloy consistently offers the best corrosion resistance in wet process phosphoric acids, even when the highest corrosion rates are considered (Table 10). Also, when the average corrosion rates are established from tests in acids obtained from different plants, G-30 alloy consistently shows the best corrosion resistance ^[14].

While G-30 alloy was designed as a specialty product to handle phosphoric acids streams, this alloy is also showing improved resistance over its predecessor alloy G-3 in many other acids such as sulfuric, nitric and formic acids (Table 11). In addition, G-30

alloy is equivalent to alloys G/G-3 in resisting localized corrosive attack (pitting, crevice, under deposit corrosion) as illustrated by the similar critical pitting temperature for these alloys. In fact, G-30 alloy offers much better resistance to pitting corrosion than various stainless steel (Figure 3). Finally, G-30 alloy appears to offer the best resistance of the many stainless alloys to corrosion in mixed acids (Table 12), as well as better resistance to stress corrosion cracking than duplex and austenitic super stainless steels (Table 13). In particular, G-30 alloy is showing excellent performance in many applications involving nitric and hydrofluoric acid (Figure 4).

ULTIMET ALLOY

Despite common belief that resistance to wear is a direct function of high hardness, wear is more related to micro-fatigue behavior than it is to hardness. It should be evident that a universal material, resistant to all forms of wear, is impractical, given the incompatible requirements for low stress abrasion and solid particle erosion, for example. Fortunately, the microstructural requirements for several forms of wear are compatible (such as erosion and galling), allowing the scope for the design of alloys which exhibit outstanding resistance to many industrial wear situations, and adequate resistance to others.

In designing ULTIMET alloy, experiments were first carried out to determine appropriate levels of chromium, molybdenum, and tungsten (i.e., levels which would provide resistance to a wide variety of corrosive media). Having fixed these levels, the effects of nickel, iron, carbon, and nitrogen were determined, with a view to striking a balance between wear properties (which, according to theory, should be degraded by stabilizers of the face centered cubic phase), ease of processing and fabrication (which should be improved by the same elements), and resistance to stress corrosion cracking (which, again, should be increased by these elements).

It was discovered that, within their soluble ranges, carbon and nitrogen exert a powerful influence on properties^[15], and that, contrary to theory, carbon is beneficial to wear behavior. This is attributed to its influence on grain boundary cohesion, which appears to override its effect on stacking fault energy, in the soluble range. This hypothesis was supported by the fact that, at very low carbon levels, rapid intergranular stress corrosion cracking was encountered. Nitrogen, the effects of which were relatively unknown in cobalt-base alloys, significantly increased the yield strength of the alloy, and enhanced resistance to pitting. Since grain size, for a given thermomechanical treatment was largely unaffected by nitrogen content, the effects of nitrogen appear to be due to its presence as an interstitial (in the grains).

Having fixed the levels of several elements, and having determined appropriate minor element additions, stacking fault energy control was finally accomplished by varying the nickel content. Several properties were evaluated as a function of nickel additions (in the approximate range 5 to 15 wt. %), before selecting 9 wt. % for the ULTIMET alloy. The effects of nickel, in this range, on resistance to cavitation erosion and pitting are illustrated in Figures 5 to 6. As shown, nickel negatively affects cavitation erosion resistance and resistance to pitting. Nickel also reduces yield strength. On the

other hand, resistance to galling versus the high-nickel corrosion-resistant alloy, alloy C-276, was actually improved by the addition of nickel.

The final chemistry of ULTIMET alloy is set at 26Cr-9Ni-5Mo-2W-3Fe, balance cobalt. In terms of wear properties, this new alloy has exhibited outstanding resistance to cavitation erosion, slurry erosion, galling and moderately high resistance to low stress abrasion, relative to austenitic stainless steels and high-nickel alloys. In a corrosion sense, the alloy possesses similar general corrosion properties to alloy 625 (Table 14), but exceeds alloys 625 and C-276 in resisting localized corrosive attack (Table 15). With regard to stress corrosion cracking, the alloy is considerably more resistant than Type 316L Stainless Steel (Figure 7), but falls short of the performance of the high-nickel corrosion alloys.

INDUSTRIAL APPLICATIONS

Following the initial developmental work, C-22, G-30 and ULTIMET alloys have each been subjected to extensive field testing, as well as evaluations by end users. Rapid acceptance of these alloys is a confirmation of their technical merits, as demonstrated by the multitude of field tests and successful service trials. Herein are some examples of industrial applications relevant to the fertilizer industry.

In wet phosphoric acid production, one area of interest is the reliability of heat exchangers, specifically when handling 54 to 70% P₂O₅. The G-30 alloy has shown the best resistance to corrosion in wet phosphoric acid environments (Table 10). Field tests conducted using test racks placed in the bonnet of heat exchangers, confirmed the relative ranking of various alloys and the superiority of G-30 alloy.

G-30 tubes have been specified for the heat exchangers (Figures 8) and replaced tubes made from alloys G-3 and 625, both of which have failed from general corrosion within months of service. To-date, there are in excess of eleven heat exchangers in wet phosphoric acid services (including those that replaced graphite heat exchangers (Table 16). Several of the G-30 alloy heat exchangers have exceeded three years of satisfactory performance.

In another aggressive application involving sulfuric acid condensates, G-30 alloy pre-cooler units performed well in handling the corrosive emission of kiln hot off-gases (Figure 9).

COST EFFECTIVENESS IN PHOSPHORIC ACID SERVICES

The economic selection of materials for a specific industrial application is influenced by various factors. While corrosion is thought to be the most important factor, there is the opinion that cost is the prevailing factor. It is stated that...“The material having the most durability is not always necessarily the best choice. The premium paid for more durable materials may be greater than the cost and inconvenience of occasional replacements of components subject to corrosion...”^[16]. On the other hand, experience with materials failure and plant maintenance indicates that reliability of operation and performance requires the correct selection and use of materials. The advantage of lower

first cost may vanish if the equipment fails, causes shutdown, and requires excessive maintenance and ultimate replacement at future inflated prices^[17]. This latter position is perhaps the most applicable to high-performance Ni-based and Co-based alloys, since these alloys are generally used when nothing else works and, hence, cost is no longer the predominant consideration.

In developing G-30 alloy as an improved corrosion-resistant alloy the focus was on corrosion prevention as a major objective, i.e., minimizing the risk of unpredictable failure^[18], while being aware of the viewpoint that "...It is rarely the task of the corrosion engineer to stop corrosion. It is his job to ensure that the selection of material is such that an economic operating life is attained at the minimum initial cost..."^[19].

When considering its balanced chemistry of chromium, iron and molybdenum plus tungsten, G-30 alloy turns out to be a cost-effective material with improved resistance to corrosion. Specifically, in terms of "material cost" (dollars per pound), the ¼-inch plate product of G-30 alloy is lower in price than several alloys that showed less resistance to corrosion in wet process acids (e.g., SAN 28 and alloy 625, Table 17). In addition, if one takes into account the "fabricated cost", i.e., material cost plus the cost of fabrication, heat exchangers of G-30 alloy are just about 2.4 times the cost of "unacceptable" 316L stainless steel. Also, G-30 alloy heat exchangers are within 1 percent of the cost of those alloys 825 and 20CB-3, within 6 percent of the cost of alloy SAN 28 heat exchangers and within 27 percent of the cost of those made of alloy 904-L (Table 18). This cost difference becomes even less important when there are high installation costs involved. As such, the current end users are appreciative of using G-30 alloy to achieve over twice the corrosion resistance at less than 25 percent increase in cost. Most important, when compared to the cost of alloy 625 (Tables 17 and 18), G-30 alloy is providing better corrosion resistance at a lower cost.

Equally important consideration must be given to the total "life cycle" cost, which may consist of maintenance costs over the life of a component, lost revenues from unscheduled shutdowns, time value of money, depreciation, and taxes, among others. Many techniques exist for economic appraisal of "life cycle" costs of different materials. These methods include return on investment, payback period, and the discounted cash flow. The last method gives a measure of present worth after taxes and equivalent "uniform annual cost". For a life expectancy of five years, the "uniform annual cost" of a typical heat exchanger of G-30 alloy is about \$32K^[20]. This is a very attractive cost when compared to those of several super stainless steels with less than half the life expectancy of that of G-30 alloy.

When compared to non-metallic materials, such as graphite, G-30 alloy's "uniform annual cost" may not appear economical. However, if the annual maintenance cost increases, or if production loss occurs due to graphite tube breakage, then G-30 alloy becomes the more economical choice. A quick calculation shows that when using a graphite heat exchanger, a "one time" production loss must not exceed \$50K before the G-30 alloy heat exchanger becomes more economical. Other sensitivity analyses also indicate that an "annual" production loss, due to breakage of the graphite heat exchanger, must not exceed an average \$8K per year, otherwise the G-30 alloy heat exchanger becomes the more cost-effective choice. Regardless of the various cost/benefit evaluations, many plants are interested in G-30 alloy as it provides improvement in corrosion resistance and, most importantly, reliability and "ease" of maintenance.

OUTLOOK

Numerous innovations in high performance alloys have been developed based on advances in corrosion science and engineering. A large emphasis is being placed on cost effectiveness that justifies the use of high performance Ni-based and Co-based alloys in corrosion control in aggressive services (e.g., phosphoric acid production). At first glance, limited applications can be identified for further utilization of high performance alloys. However, the issues of reliability, efficiency, "ease of maintenance", and environmental concerns are leading to a wider use of Ni-based and Co-based alloys in critical, aggressive applications. The successful operating experience in these critical applications, coupled with realistic approaches to cost effectiveness is believed to be the main reason for the increase in the use of high performance alloys in chemical processing industries.

Note: HASTELLOY, ULTIMET, C-22 are trademarks of HAYNES International, Inc.

REFERENCES

1. R. Franks, "Corrosion-Resistant Alloys", U.S. Patent No. 1 836 317, 1931.
2. I. Class, H. Graefen, and E. Scheil, "Highly Corrosion-Resistant Ni-Cr-Mo Alloy with Improved Resistance to Intergranular Corrosion", U.S. Patent No. 3 203 792, 1965.
3. F.G. Hodge, Corrosion, 29, p. 375, 1973.
4. A.I. Asphahani, "Corrosion-Resistant Nickel Alloy", U.S. Patent No. 4 533 414, 1985.
5. M.A. Streicher, Corrosion, 32, p. 79, 1976.
6. A.I. Asphahani, "Improved High Performance Alloys and Their Usefulness in Corrosion Prevention and Control in Defense Systems", 33rd Sagamore Army Materials Research Conference, Burlington, Vermont, July 28-August 1, 1986.
7. P.E. Manning and J.D. Schoebel, "HASTELLOY® alloy C-22 – A New and Versatile Material for the Chemical Process Industries", Werkstoffe und Korrosion, 37, p. 137, 1986.
8. J.L. Nickerson and A.I. Asphahani, "Corrosion Evaluation of Alloys for Flexural Hosing in the Space Shuttle Launch Environment", Proceedings of Conference on Aerospace Corrosion Control, Perthshire, Scotland, Salwell Publishing, 1989.
9. I. Sekine, "Material for Conductor Roll", Mitsubishi Metal Corporation, Okegawa, Internal Report 59-9-22, 1985.
10. H. Diekmann, "High Alloy Stainless Steel and Nickel-Base Alloys in Chemical Equipment Construction", Werkstoffe und Korrosion, 37, p. 130, 1986.
11. A.I. Asphahani, W.L. Silence and P.E. Manning, "High-Chromium, Nickel-Base Alloys", U.S. Patent No. 4 410 489, 1983.
12. P.E. Manning, J.D. Smith, and J.L. Nickerson, "New Versatile HASTELLOY® Alloys for the Chemical Process Industry", CORROSION/88, Paper No. 317, St. Louis, March 1988.

13. "Phosphoric Acid", Vol. 1, Part II, ed. A.V. Slack, New York: Marcel Dekker, p. 819, 1968.
14. A.I. Asphahani and J.L. Nickerson, "HASTELLOY® G-30 Alloy: A Specialty Alloy For Applications in the Process Industries", HAYNES Technical Information Bulletin No. H-2058, March 1988.
15. P. Crook, A.I. Asphahani and S.J. Matthews, "Corrosion and Wear Resistant Cobalt-Base Alloy", U.S. Patent No. 5 002 731, 1991.
16. A.V. Slack, Editor, "Phosphoric Acid", Volume 1, Part II, p. 808, Marcel Dekker, Inc., New York, 1968.
17. C.M. Schillmoller, Schillmoller Associates-Consultants, letter to A.I. Asphahani, June 17, 1987.
18. B. Moniz, "Process Industries Corrosion", ASTM Standardization News, p. 50, May, 1987.
19. M. Turner, "Materials for the Process Industry", Metals and Materials, p. 136, March, 1987.
20. D.C. Agarwal, "HASTELLOY alloy G-30 and FERRALIUM alloy 255, the cost effective answers to Corrosion/Erosion problems in Wet Phosphoric Acid Production", AIChE, Clearwater Beach, Florida, May, 1987.

TABLES

Table-1: Nominal chemical compositions (wt. percent)

Alloy	Cr	Mo	W	Fe	Cb	Ti	V	Mn	C	Si	Ni
C	15	16	4	5	-	-	0.35*	1.0*	0.08*	1.0*	Bal.
C-276	16	16	4	5	-	-	0.35*	1.0*	0.01*	0.08*	Bal.
C-4	16	16	-	3*	-	0.70*	-	1.0*	0.01*	0.08*	Bal.
C-22	22	13	3	3	-	-	0.35*	0.05*	0.015*	0.08*	Bal.
625	21.5	9	-	5.0*	3.5	0.40*	-	0.50*	0.10*	0.50*	Bal.

* Maximum

Table-2: Uniform corrosion rates in mils per year*; oxidizing environments

Environment	Test Temp., °C	C-22	C-276	C-4	625
(5% HNO ₃ + 6% HF)	60	67	207	204	73
(5% HNO ₃ + 1% HF)	Boiling	0.5	8	11	1
(5% HNO ₃ + 25% H ₂ SO ₄ + 4% NaCl)	Boiling	12	64	97	713
(25% H ₂ SO ₄ + 1.2% HCl + 1% FeCl ₃ + 1% CuCl ₂)	Boiling	7	55	2294	3847

* 1 mil per year = 0.025 millimeter per year

Table-3: Uniform corrosion rates in mils per year; reducing environments

Environment	Test Temp., °C	C-22	C-276	C-4	625
1.5% HCl	Boiling	11	29	64	353
10% H ₂ SO ₄	Boiling	11	23	31	46
10% H ₂ SO ₄	70	0.5	11	24	121

Table-4: Stress corrosion cracking: C-shape specimens (duration: 1 to 12-month tests)

25% NaCl + 100 psi H ₂ S + 1 g/l Sulfur				
Alloy	177°C (350°F)	232°C (450°F)	4% ZnBr ₂ 204°C (400°F)	1% HCl 177°C (350°F)
625	No Cracking	Failure	Not Tested	Failure
C-276	No Cracking	Failure	Failure	Failure
C-22	No Cracking	No Cracking	No Cracking	No Cracking

Table-5: Hydrogen embrittlement: C-shape specimens coupled to carbon steel, R.T., 5% NaCl + 0.5% acetic acid, saturated H₂S; (duration: 869 hours)

Condition	C-22 Alloy	Alloy C-276
Mill Anneal	NC/NC/NC**	NC/NC/NC
20% CR	NC/NC/NC	NC/NC/NC
40% CR	NC/NC/NC	NC/NC/NC
20% CR + 100 hrs. at 500°C	NC/NC/NC	90/136/160 hrs.
40% CR + 100 hrs. at 204°C	NC/NC/NC	312/312/816 hrs.

* CR = cold-rolled condition; ** NC: no cracking

Table-6: Nominal chemical compositions (wt. percent)

Alloy	Fe	Ni	Cr	Mo	W	Cu
316L	Bal	12	18	2	-	-
904-L	Bal	25	20	4.5	-	1.5
JS777	Bal	26	20	4.5	-	2.5
SAN 28	Bal	31	28	3.5	-	1
20CB-3	Bal	34	20	3	-	3.5
825	Bal	42	21	3	-	1.8
G	20	Bal	22	6	-	2
G-3	20	Bal	22	7	-	1.5
690	9	Bal	29	-	-	-
G-30	15	Bal	30	5	2.5	1.5

Table-7: Effect of chromium (and copper) on corrosion resistance to 46% P₂O₅ (116°C)

Alloy	Corrosion Rates (mpy)
C-276 (16Cr, 0Cu)	44
625 (22Cr, 0Cu)	18
G (22Cr, 2Cu)	16
690 (30Cr, 0Cu)	5
G-30 (30Cr, 1.5Cu)	4

Table-8: Effect of molybdenum on corrosion resistance to 52% P₂O₅ (149°C)

Alloy	Corrosion Rates (mpy)
690 (30Cr, 0Mo)	447
G-30 (30Cr, 4Mo)	61

Table-9: Effect of tungsten on corrosion resistance to 54% P₂O₅ (149°C)

Alloy	Corrosion Rates (mpy)
G-30A (30Cr, 4Mo, 0W)	165
G-30B (30Cr, 4Mo, 2W)	38

Table-10: Highest corrosion rate (mpy)

Alloy	54% P ₂ O ₅ 116°C (240°F)	54% P ₂ O ₅ 149°C (300°F)	70% P ₂ O ₅ 204°C (400°F)
JS777	518	1191	23
SAN 28	63	3236	53
825	553	1331	18
G	94	1700	16
G-3	41	1246	28
625	36	803	22
G-30	7	317	10

Table-11: Average corrosion rates (mpy)

Environment	G-3	G-30
98% H ₂ SO ₄ , 110°C (230°F)	29	17
10% H ₂ SO ₄ , Boiling	24	12
ASTM G-28A, Boiling	11	7
65% HNO ₃ , Boiling	12	4
88% Formic, Boiling	5	1

Table-12: Average corrosion rates (mpy)

52°C (125°F)	316L	904L	825	20Cb-3	AL-6XN	254 SMO	625	G-30
20% HNO ₃ + 1% HF	360	21	27	57	20	28	29	8
20% HNO ₃ + 3% HF	303	50	66	140	54	84	54	18
20% HNO ₃ + 5% HF	1154	100	132	249	94	91	140	29
80°C (176°F)	316L	904L	825	20Cb-3	AL-6XN	254 SMO	625	G-30
11% HLC + 10% H ₂ SO ₄	>10000	520	295	373	337	1034	179	288
11% HLC + 25% HNO ₃	>10000	6281	>10000	>10000	1326	2958	126	23
3% HF + 10% HNO ₃	1700	160	162	1164	204	296	20	5

Table-13: Stress corrosion cracking: C-shape specimens (1-week exposure)

	316L	2205	254 SMO	AL6XN	G-30
25% NaCl 204°C (400°F)	Cracking	Cracking	Cracking	Cracking	No Cracking
35% MgCl ₂ 125°C (257°F)	Cracking	Cracking	Cracking	Cracking	No Cracking
5% NaCl + .5% CH ₃ COOH 149°C (300°F)	Cracking	Cracking	Cracking	Cracking	No Cracking

Table-14: Average corrosion rates (mpy)

Environment	316L	STELLITE	ULTIMET	625	C-276	C-22
65% HNO ₃ , Boiling	9	5434	6	21	848	134
10% H ₂ SO ₄ , Boiling	1868	232	99	37	18	12
1% HCl, Boiling	524	170	0.3	0.9	13	3
54% P ₂ O ₅ , 116°C (240°F)	201	15	8	14	28	9
ASTM G-28A, Boiling	28	14	8	24	246	40
ASTM G-28B, Boiling	3170	2888	2	2721	53	7

Table-15: Critical pitting temperature (temperature at which pitting is initiated in 11.5% H₂SO₄ + 1.2% HCl + 1% FeCl₃ + 1% CuCl₂)

Alloy	Pitting Temperature	
C-22	120°C	(248°F)
ULTIMET	115°C	(239°F)
C-276	110°C	(230°F)
625	75°C	(167°F)
STELLITE 6B	45°C	(113°F)
20CB-3	30°C	(86°F)
316L	25°C	(77°F)

Table-16: Industrial applications of alloy G-30 in phosphoric acid services (circa 1988)

<u>Plant</u>	<u>Environment</u>	<u>Component</u>
AGRICO	54% P ₂ O ₅	Clamps, Bolts, Nuts
Bartow, FL	54% P ₂ O ₅ (Vapor phase)	Attack Tank*
Donaldsonville, LA	54% P ₂ O ₅ + H ₂ SO ₄ + HF	Ejectors
Farmland	28% P ₂ O ₅ + H ₂ SO ₄ + HF	Attack Tank
Bartow, FL	28% P ₂ O ₅ + H ₂ SO ₄ + HF	Agitator Blades
S.I.A.P.E.	70% P ₂ O ₅	Evaporator Tubes*
Tunisia	54% P ₂ O ₅	Pump Parts
Occidental	54 to 70% P ₂ O ₅	Cooler Tubes
White Springs, FL		
Proprietary	58 to 64% P ₂ O ₅	Bar, Plate, Tubes

*Field trial stage

Table-17: Price comparison: corrosion-resistant alloys 500 lb. quantity of ¼-inch plate (as provided by distributors; July, 1987)

Alloys	Dollars per pound	Ratio
316L	1.39*	1
904-L	3.37	2.4
JS700	4.65*	3.4
825	4.07*	2.9
20CB-3	4.50*	3.2
SAN 28	8.30**	5.9
G-3	5.17**	3.7
G-30	5.17**	3.7
625	8.50**	6.1

* Average; ** Producers prices

Table-18: Heat Exchangers “fabricated cost” using various materials circulation rate of 10,000 gpm; Acid feed rate of 100/125 gpm. (Total of 359 tubes of 1.5” OD x .083” wall x 18’ length)

	Cost in thousands of dollars (July, 1987)						
	316L	904L	SAN 28	825	20CB-3	G-30	625
Tubing	23	74	99	105	105	107	136
Sheet, head, nozzles	6	16	21	23	23	24	29
Others (C-steel support)	16	16	16	16	16	16	16
Total Material	45	106	136	144	144	147	181
Total Labor	35	35	45	45	45	45	45
“Fabricated Cost”	\$80K	\$141K	\$181K	\$189K	\$189K	\$192K	\$226K

FIGURES

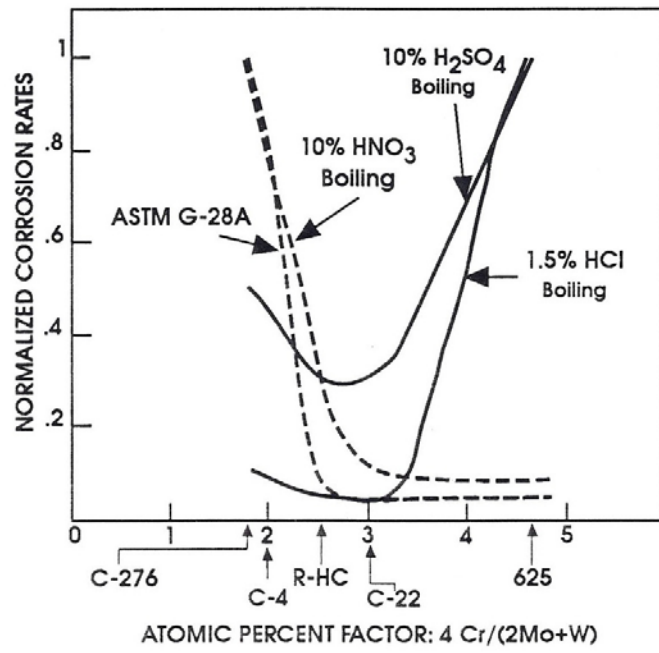


Figure 1. Optimum Range for Best Resistance to Both Oxidizing and Reducing Environments.

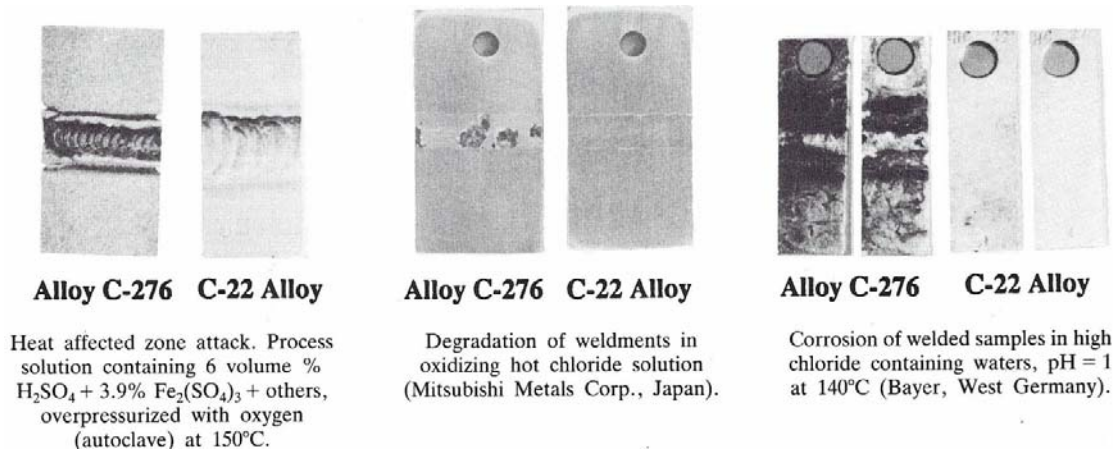


Figure 2. Corrosion Behavior of Welded Samples Showing the Improved Performance of C-22 Alloy Over That of Alloy C-276.

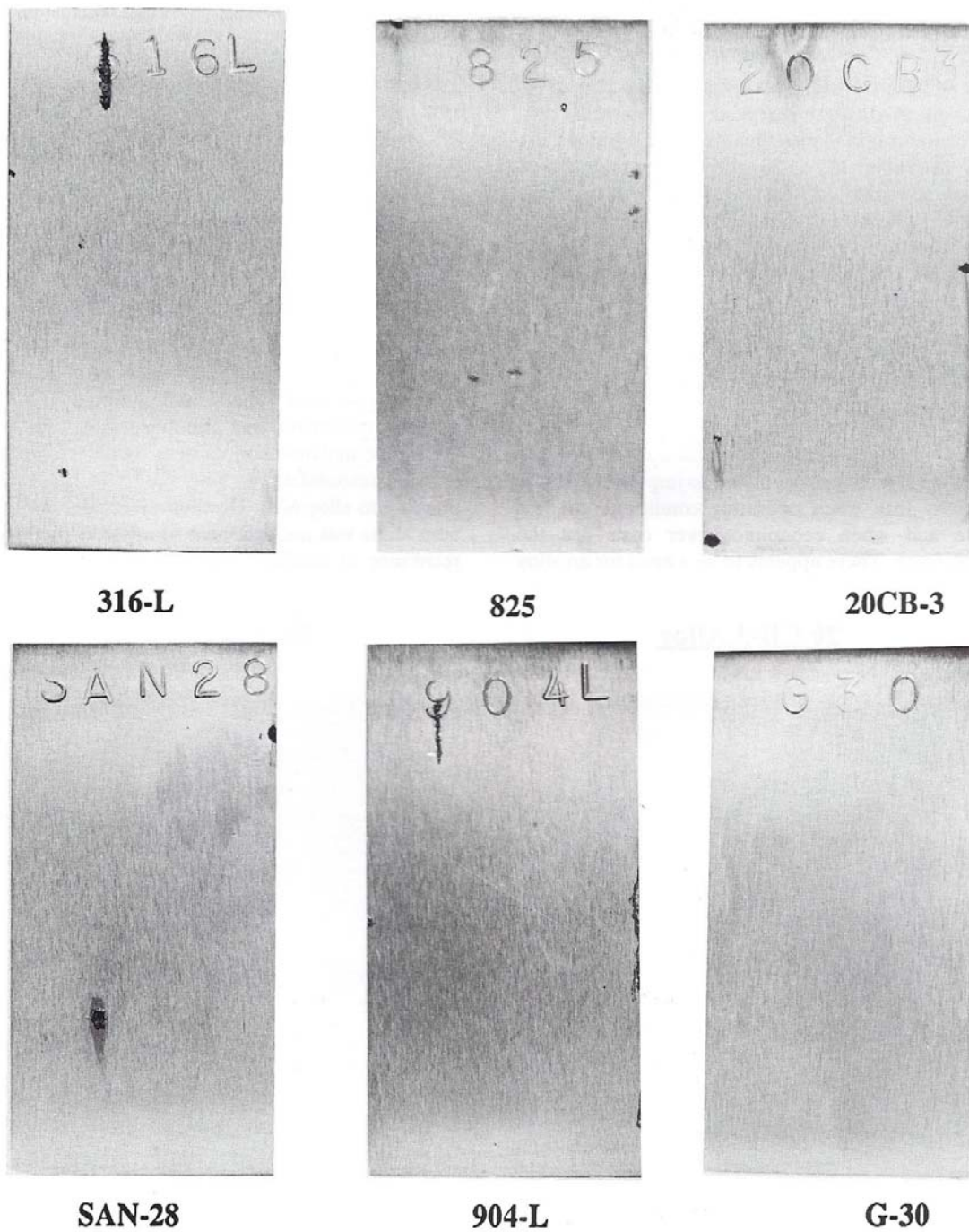
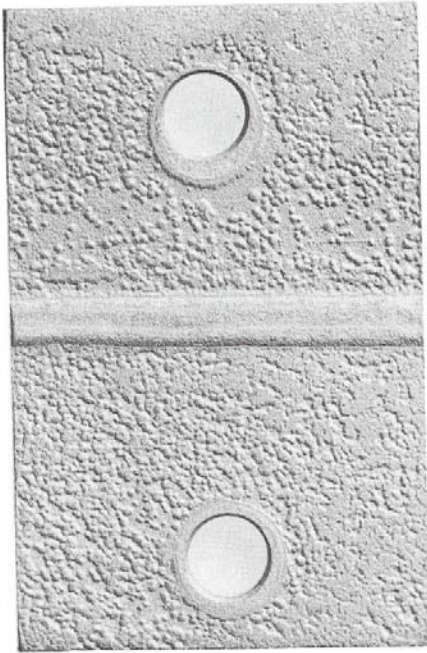


Figure 3. Comparison of Pitting Resistance as Illustrated by Tests in 4% NaCl + 0.1% Fe₂ (SO₄)₃ + 0.01M HCl at 65°C (149°F).

20 CB-3 Alloy



G-30 Alloy

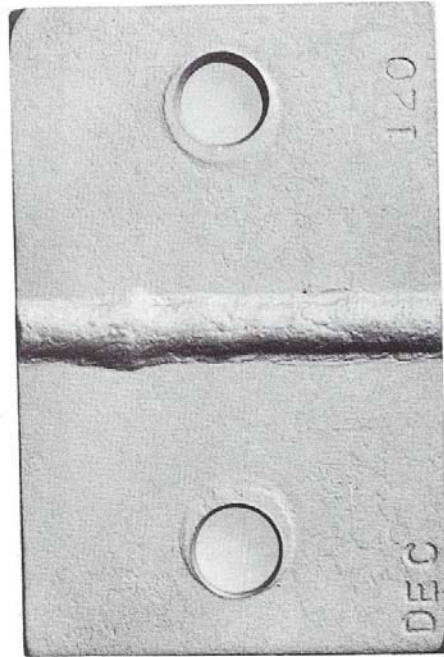


Figure 4. Field Test: 59-Day Exposure in Dust Scrubber Acid Tank–HF Reaction (Sulfuric Acid, Hydrofluoric Acid, Fluorosulfonic Acid, Calcium Sulfate) 120°C (248°F).

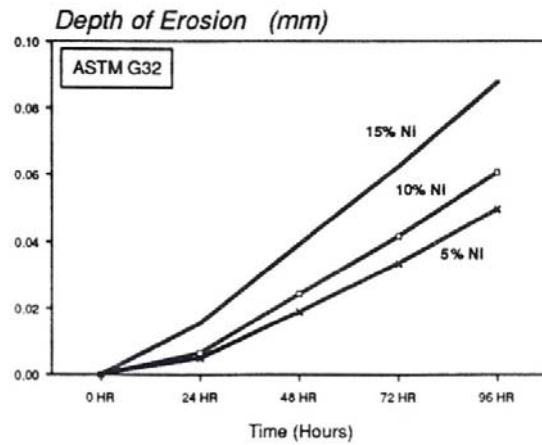


Figure 5. Effect of Nickel Content on Cavitation-Erosion.

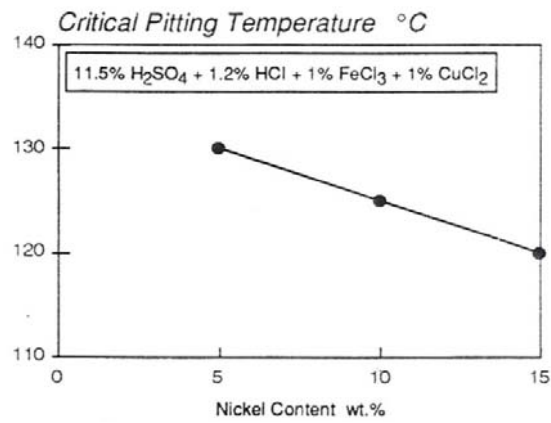


Figure 6. Effect of Nickel on Critical Pitting Temperature.

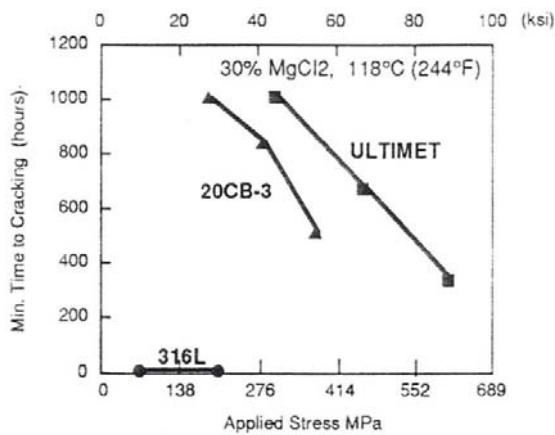


Figure 7. Effect of Applied Stress on Resistance to Cracking.



Figure 8. Super Phosphoric Acid Production (Heat Exchanger).

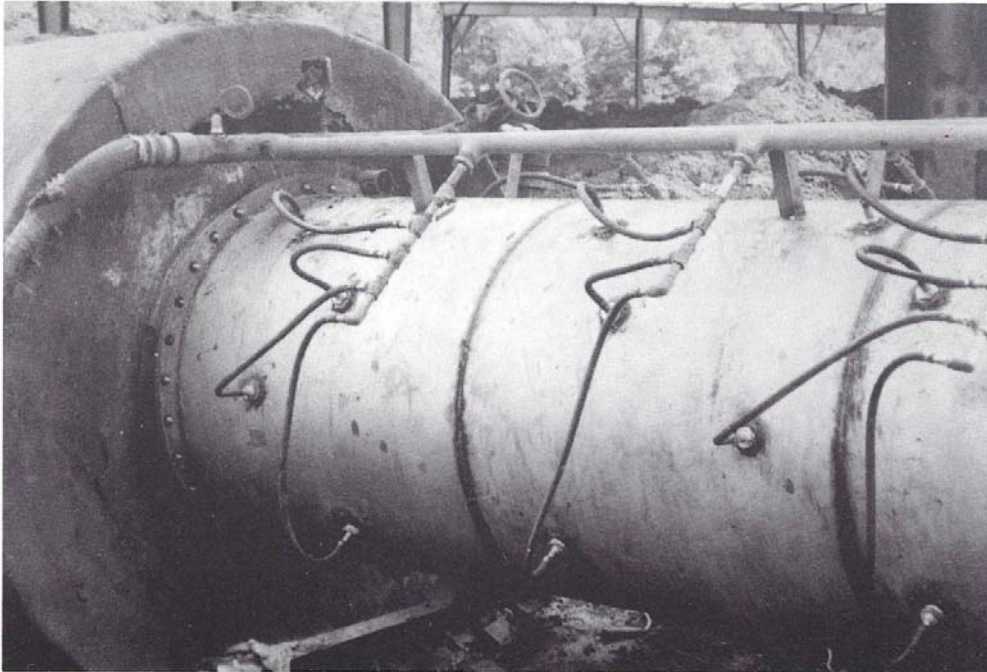
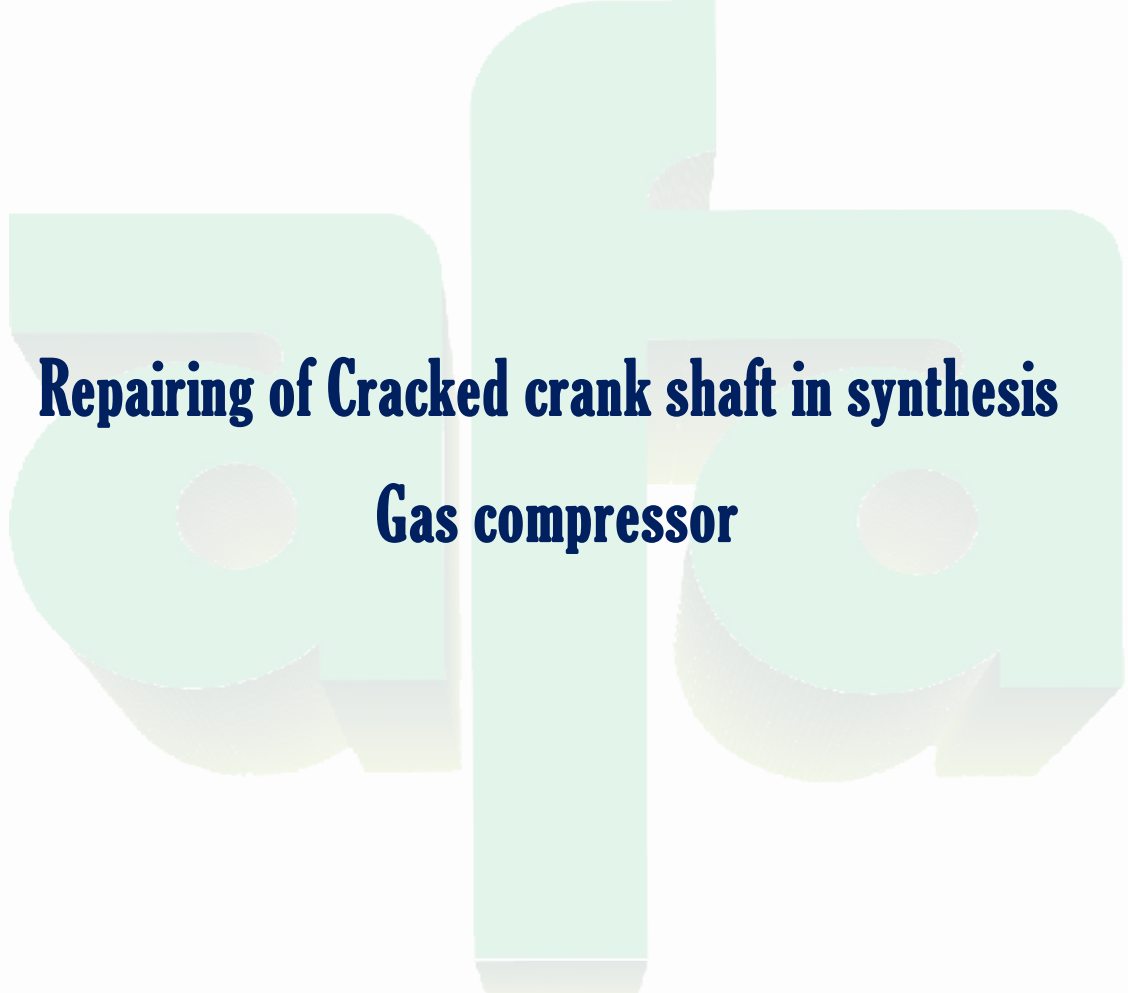


Figure 9. Pre-cooler Unit of HASTELLOY Alloy G-30 to Handle Corrosive Kiln Off Gases and Sulfuric Acid Condensates (courtesy of Eden Machine & Design Company, Eden, North Carolina).

***AFA WORKSHOP: FITNESS FOR SERVICE IN CHEMICAL
INDUSTRIES***

Aswan, EGYPT

25 - 27 Nov 2012



Repairing of Cracked crank shaft in synthesis

Gas compressor

Eng. H. Mostafa

Head of mechanical engineering sector, KIMA, Egypt

EGYPTIAN CHEMICAL INDUSTRIES



KIMA



Case study:

Repairing of Cracked crank shaft in synthesis gas compressor

Prepared by

Eng. Hassan Mostafa Ahmed

1

Introduction

KIMA company in ASWAN city (EGYPT) established in 1958 since about 54 years, it is the second fertilizer plant in Egypt (the first plant was that in Suez on 1951), Aswan by the year 1956 was chosen as the location because the electricity available from Aswan dam (200 M Watt) which only KIMA was a consumer at that time could cover the electric power needed by the electrolysis process, Now KIMA is in a critical situation due to High cost of electric energy, Existing of all machines and Daily shutdown since about eight years from electric energy supplier.

As a result of existing and daily shutdown damage was repeated in machines parts, as occurred in syntheses gas compressor department, it includes five compressors, since four years the fifth compressor out of service

2

due to ultimate failure in crank shaft, Also a crank shaft of third Compressor, was damaged with crack in forty percent of its cross area approx.

This paper reports repairing works in third synthesis gas compressor (All works provided by KIMA), The first part of this paper includes, compressor specifications, crank shaft characteristics and Crack description, The second part presents fastener joint as a suitable choice for repairing technology in this case with its design requirements, and tools, Also estimating the increase in shaft strength capacity due to repairing, and predict the repairing effect on fatigue growth rate.

3

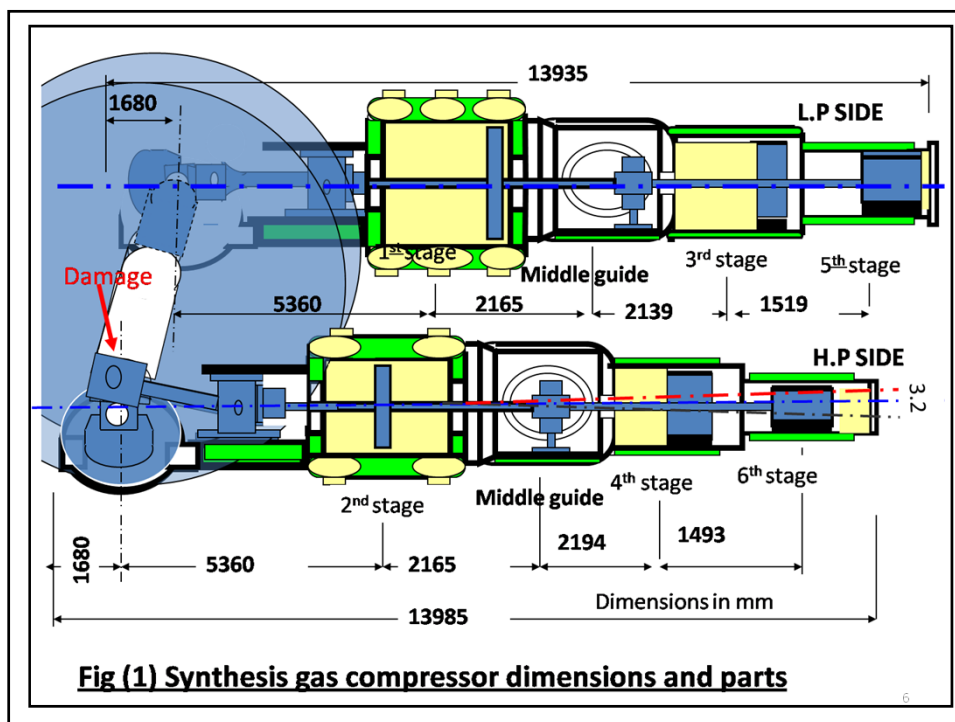
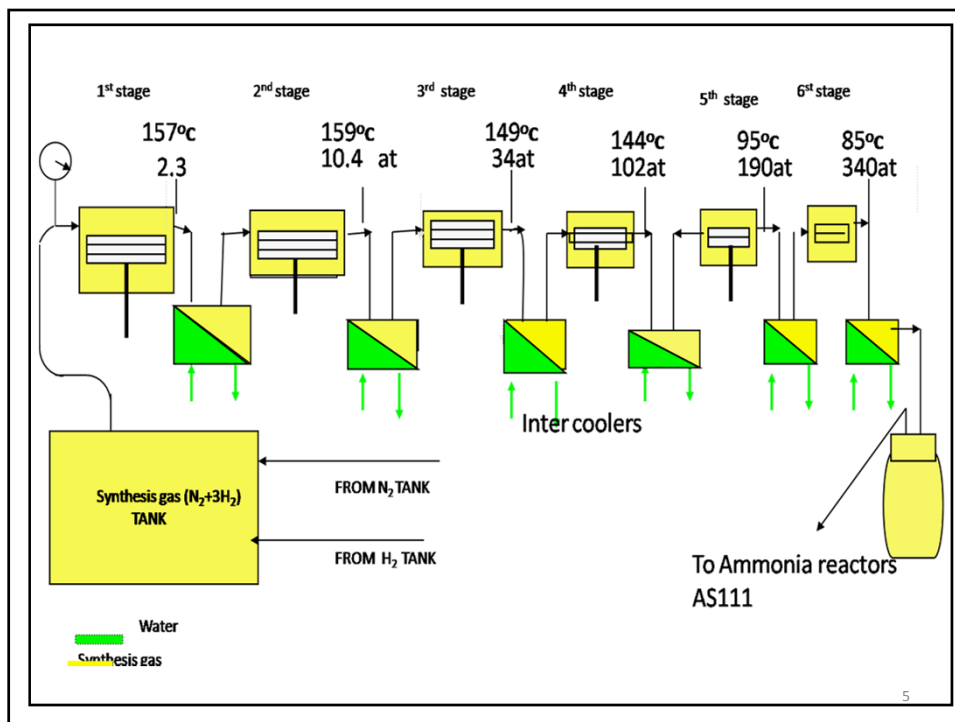
COMPRESSOR SPECIFICATIONS

DEMAG compressor six stages

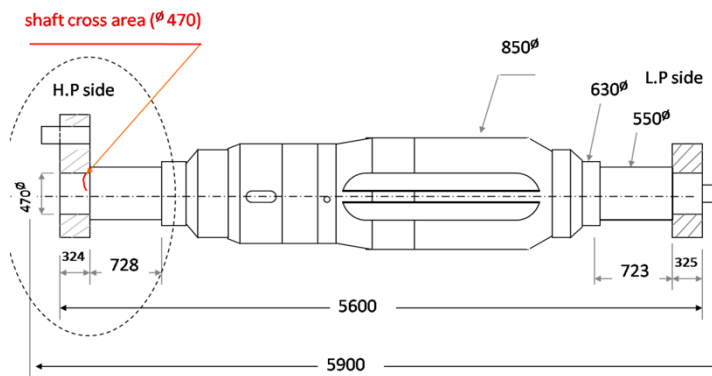
Medium: Synthesis gas (N+3H₂)
Suction pressure : 1.02 ata
Suction temperature: 45 ° C
Capacity: 13150 m³/hr
Discharge pressure: 341 ata
Speed 125 rpm
Power 4300 KW



4



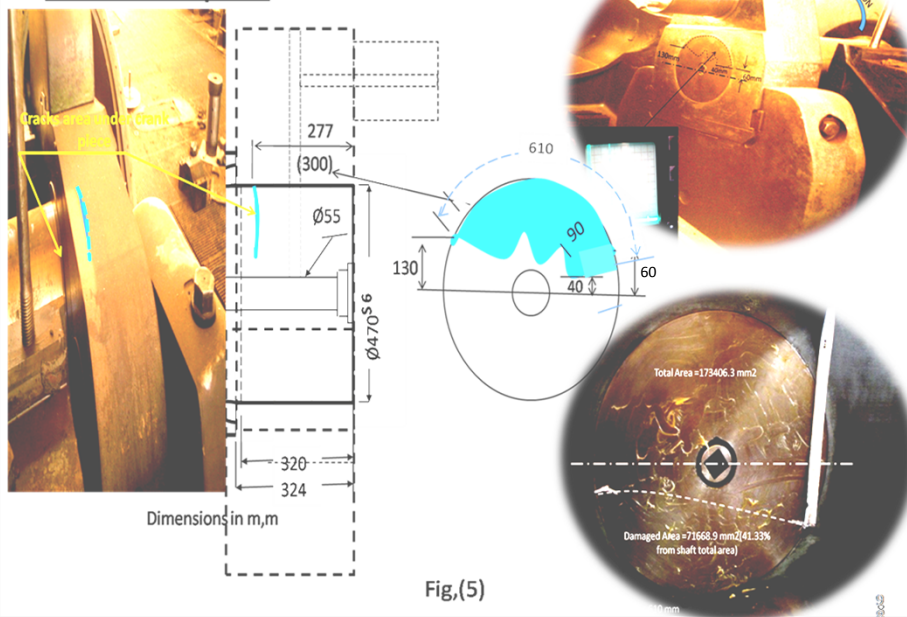
Crank shaft Characteristics



Fig,(6) Crank shaft dimensions

Material Ck35
 Annealed
 Min. Strength 500 Mpa, Max. Strength 600MPa
 Yield 260 Mpa, Impact 20 J

Crack description



Fig,(5)

Repairing Technology

Due to Crack position (fig.5, 6),and Interference fit between shaft and Crank piece, the fastener joints at crack both sides area are used as a suitable choice of repairing in this case .

Main Topics of Repairing:

- 1- Objectives.
- 2- Basic concepts.
- 4- Technologies.

Objectives

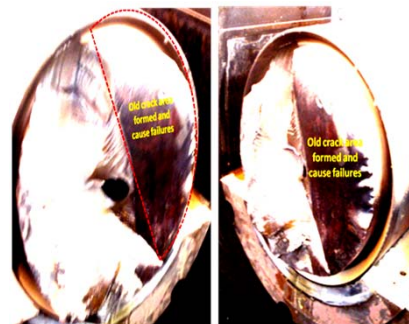
Acc. of History records:

ultimate failure was occurred after operating time of crank shafts of 46 and 48 years in compressors No.1 and No.5, due to Fatigue crack area about **45%** of total shaft c. area,

it will considered as shaft ultimate failure limit (Sh.U.F.L) (fig.9). Fig.9

In the Present Case, fatigue crack area about 41.3% of sh. c. area, (**nearest Sh.U.F.L**)

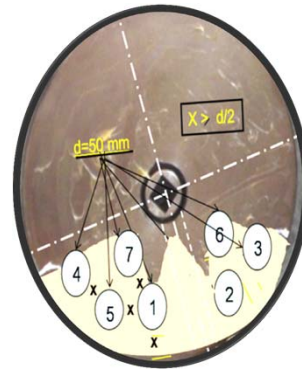
- Repairing objectives are increasing shaft strength, and reducing fatigue crack growth rates, In order to extend shaft operating life time about 5 years (minimum), at that time a new plant KIMA2 (1200 T.A/d) will be in operations, and all gases and ammonia production departments in existing plant will be stopped**



Basic Concepts

Design requirement .

- Joint materials, thread engagement length
- fastener diameter, number of TPI, and length.
- different weights between holes removal metal and stud metal .



Interference

between the shaft and crank piece must not be reduced, then Fasteners are contracted by cooling and inserted into Holes, when at room temperature, expansion creates interference

- Determine fastener cooling time, reduction in dimensions, and assembly time.

11

According to the design requirements:-

1- Stud materials was chosen with high tensile strength "34CrNiMo6".

NDT:- a) Ultra sonic waves. b) Measuring of hardness (36–38 HRC)

-DT:- T.S =1100 N/mm² , Impact=42 J

Mechanical test specimens

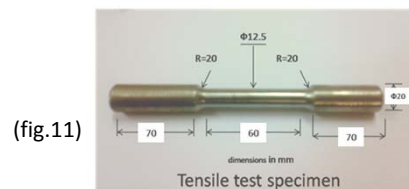
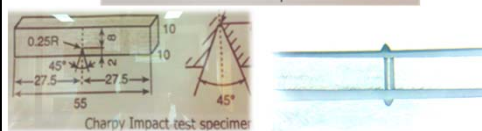
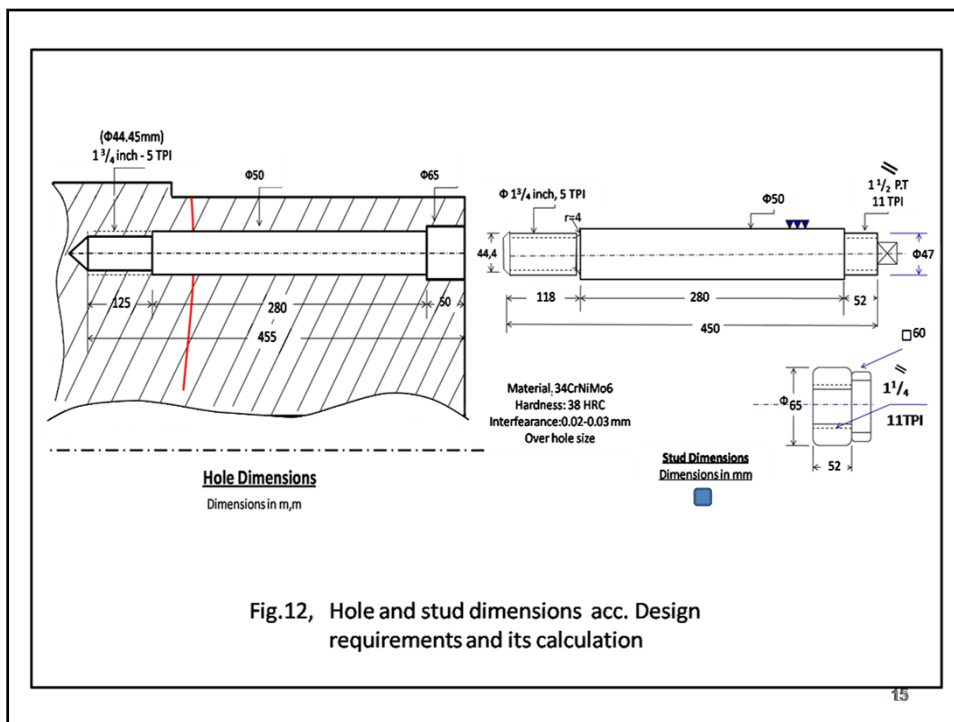


(fig.11)



34CrNiMo6							
Material No:							
1.652							
Material group: Steel for quenching and tempering according to DIN EN 10083							
Chemical composition: (Typical analysis in %)	C	Si	Mn	Cr	Mo	Ni	other
	0.34	0.25	0.50	1.50	0.25	1.55	(Pb)
Application: Heat treatable steel for high strained automotive and motor construction components with a typical tensile strength range of 1000 - 1300 N/mm ² .							

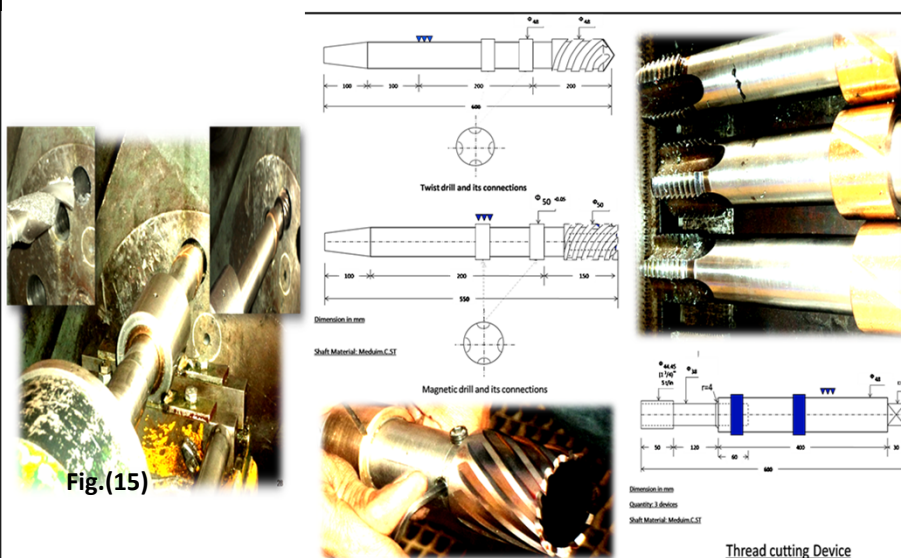
12



15

Machine and Tools: Small Boring machine used at compressor site, (fig15)

With tools as Twist and Magnetic drills, also Thread cutting device fig (14)



18

Discussion

Estimation of strength capacity for shaft and studs.

- 1- Shaft tensile capacity,
- 2- Studs tensile stress area, and Shear area.
- 3- Studs tensile capacity, shear capacity and impact capacity.

Properties	Base Metal (Ck 35)	Stud Metal (34CrNiMo6)
Tensile Strength (N/mm ²)	500	1100
Yield Strength (N/mm ²)	260	900
Impact (J)	20	42
Density g/cm ³	7.86	7.86
Thermal Expansion Factor (20-200 °C)	$11.9 \cdot 10^{-6}$	$12 \cdot 10^{-6}$
Thermal conductivity W/m k	43	38
Specific Heat capacity J/Kg K	440	460

Table 1. Properties of Base and Stud metal

15

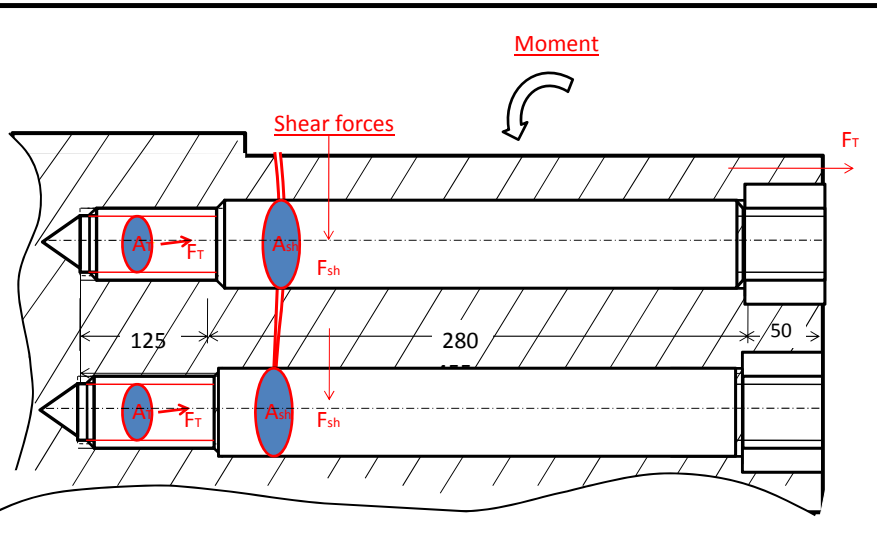


Fig.(20), Forces affects on Stud c. area of fastener Joint

17

Results of calculations

Repairing of shaft by Fastener joints leading to:

- Increasing shaft tensile capacity with 13.7%,
(it becomes 72.37 % of original shaft tensile capacity)
- Increased operating shaft shear area with 9.7% ,
(it becomes 68.37% of original shaft shear area),
- Increasing shaft shear capacity with 20.87%,
(it becomes 79.54 % of original shaft shear capacity).
- Increasing shaft impact capacity with 20%,
(it becomes 78.87% of original shaft impact capacity).
- Comparing these results with ultimate failure limits (55%), specially for shaft strength capacity.

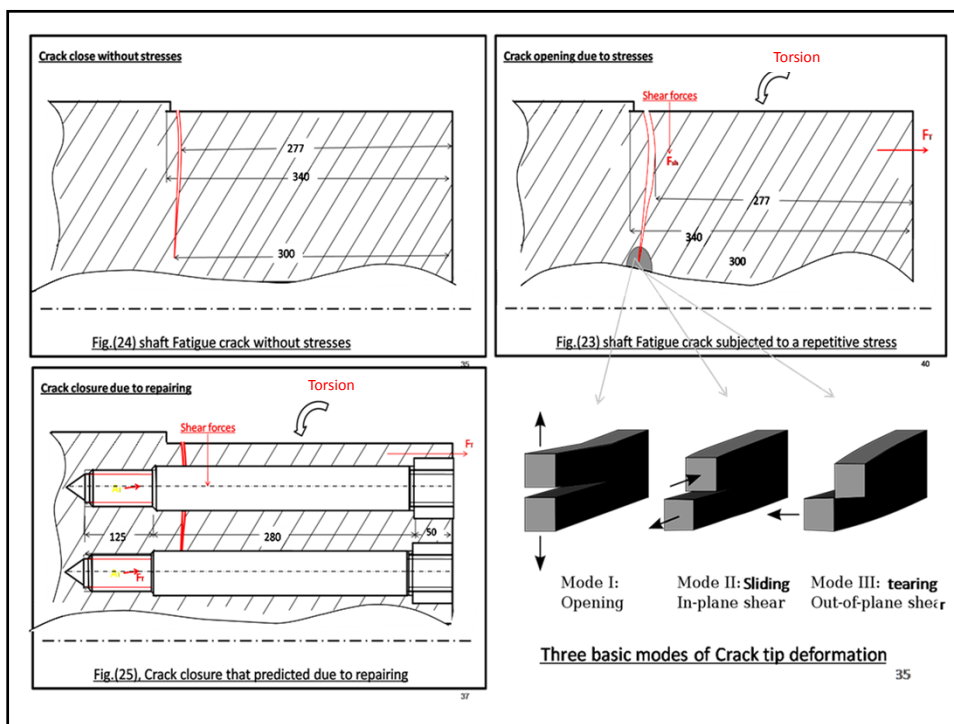
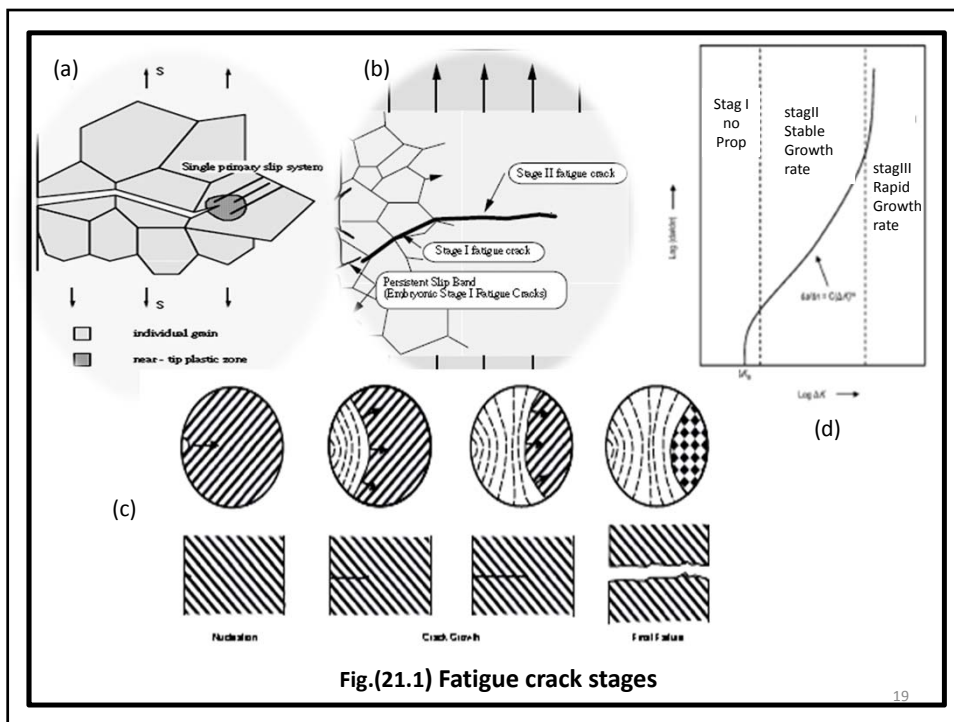
17

- Fatigue crack growth rate

In the present case:

- Crack area, about 41.3% of shaft cross area, nearest the ultimate failure (45%), the fatigue crack was in **stage III**
- Fatigue Crack in its stage III, was rapid growth rate until ultimate failure, fig.(21d).
- Fasteners material "34CrNiMo6" its fatigue life and fatigue resistance strength higher than base metal "Ck35" .
- Repairing by fastener joints in this case leading to:-
 - 1- Partial of load will be picked up by fasteners .
 - 2- The crack will temporarily stop propagating (fig.25).
 - 3- Decrease in the crack growth rate

18



Conclusion

Repairing by Fastener joints in this case will increase shaft resistance for shear load with 20 % , for tensile load with 13.7 % and for impact load with 20 % , So the total shaft strength capacity becomes for shear 78.7% , for tensile 72.4% , and for impact 78.7% of shaft design strength capacity. Also fastener joints holds crack both surfaces and may reduce or stop crack propagating, leading to decrease in the crack growth rate, on the other hand the compressor was in general maintenance and it will be recommended that the maximum load while compressor in operation not exceeds than 70% of its maximum load, in order to be suitable for total shaft strength capacity after repairing, and get more decrease in the crack growth rate, also it will be inspected of shaft cross area at various intervals, to monitoring and estimating the crack growth rate.

***AFA WORKSHOP: FITNESS FOR SERVICE IN CHEMICAL
INDUSTRIES***

Aswan, EGYPT

25 - 27 Nov 2012



Delegates Lists

#	Country	Name	Position	Company
1	Egypt	Diaa IBRAHIM	Vice President of Maintenance & Pipes Sector	Abu Qir Fertilizers Co.
2	Egypt	Khaled ABOU ELENIN	Production Head Sector	Abu Qir Fertilizers Co.
3	Egypt	Mohamed EL ADAWY	GM Processing Ammonia & Acid	Abu Qir Fertilizers Co.
4	Egypt	Salah EL SAWY	GM, Ammonia Production Administration	Abu Qir Fertilizers Co.
5	Egypt	Amr AHMED	Mechanical Engineer	Abu Qir Fertilizers Co.
6	USA	Aziz ASPHAHANI	Chairman	Advanced Motion Technologies
7	Egypt	Shafik ASHKAR	Secretary General	AFA
8	Egypt	Mohamed EL-SHABOURY	Finance & Administration Manager	AFA
9	Egypt	Mohamed Mahmoud ALI	Technical Studies Manager	AFA
10	Egypt	Mushira MOHARAM	Head, Publishing & Doc. Section	AFA
11	Egypt	Wael MAZEN	Head, Administration Section	AFA
12	Egypt	Mazen GHONIEM	Head, Information Center	AFA
13	Egypt	Ehab KHAMIS	Ammonia Maintenance Manager	ALEXFERT Co.
14	Egypt	Ayman SAAD	Urea Maintenance Senior Eng.	ALEXFERT Co.
15	Egypt	Hazem ABBAS	Inspection Eng.	ALEXFERT Co.
16	Egypt	Ahmed SADAWY	Piping Eng.	ALEXFERT Co.
17	Egypt	Maged YASEEN	Chairman	Aqua Trust for Water Treatment Co.
18	Egypt	Fayza ABU ZAID	General Manager	Aqua Trust for Water Treatment Co.
19	Jordan	Nayef KASASBEH	Plants Mechanical Manager	Arab Potash Co.
20	Jordan	Muawia SAMHOURI	Planning & Engineering Manager	Arab Potash Co.
21	Germany	Andrey GUMENYUK		BAM
22	Egypt	Yehya MESHALY	Chairman	Chemical Industries Holding Company
23	Japan	Toshikazu SHIBASAKI	Senior Consultant	Chiyoda Advanced Solutions Corporation
24	Egypt	Hamed Ahmed ABDEL ALEEM	Researcher	CMRDI
25	Egypt	Bahaa ZAGHLOUL	Technical Consultant	CMRDI
26	Egypt	Abdel Monem EL BATAHGY		CMRDI
27	Egypt	Alaedin ABBAS	Managing Director	Consulting Office Mechanical Engineering
28	Egypt	Ashraf Mahmoud ABDEL FATTAH		EEL Delta Co. for Fertilizers
29	Egypt	Mushira Mahmoud EMARA	Ammonia Urea Project, Manager	Egyptian Chemical Industries KIMA
30	Egypt	Mostafa MOHARAM	EFC II Director	Egyptian Fertilizer Co. (EFC)
31	Egypt	Ahmed Mohamed Ibrahim TELEB	Shift Supervisor Engineer Ammonia I	Egyptian Fertilizer Co. (EFC)
32	Egypt	Gamal Fawzy EL SABER	Foreman Ammonia I	Egyptian Fertilizer Co. (EFC)

33	Egypt	Mohamed Elsayed ABDEL MAGUID	Foreman Ammonia II	Egyptian Fertilizer Co. (EFC)
34	Egypt	ElSayed Gaber KOUAD	Mechanical Maintenance Section Head	Egyptian Fertilizer Co. (EFC)
35	Egypt	Mohamed Abdou ABDEL LATIF	Mechanical Maintenance Foreman	Egyptian Fertilizer Co. (EFC)
36	Egypt	Ibrahim ELZAYAT	Mechanical Workshop Section Head	Egyptian Fertilizer Co. (EFC)
37	Egypt	Ismail Mostafa ISMAIL	Mechanical Workshop Foreman	Egyptian Fertilizer Co. (EFC)
38	Egypt	Sameh TOLBA	Civil Section Manager	Egyptian Fertilizer Co. (EFC)
39	Egypt	Ahmed Nabil OSMAN	Inspection Section Head	Egyptian Fertilizer Co. (EFC)
40	Egypt	Adel Mohamed Ibrahim KAOUD		El Delta Co. for Fertilizers
41	Egypt	Hassan Mohamed HASSAN		El Delta Co. for Fertilizers
42	Egypt	Ahmed Talaat IBRAHIM		El Delta Co. for Fertilizers
43	Egypt	Islam Mostafa Saad ABDOU		El Delta Co. for Fertilizers
44	Egypt	Ali Ibrahim Mostafa SEDDIQ		El Delta Co. for Fertilizers
45	France	Claude BATHIAS		Emeritus Professor
46	Saudi Arabia	Arafat GHOSHEH		Guest
47	Egypt	Mokhtar EL GAZZAR	Ammonia Maintenance Manager	Helwan Fertilizers Co.
48	Egypt	Ahmed EL AGAMY	Engineer	Helwan Fertilizers Co.
49	Egypt	Abdel Rahman NAGAH	Engineer	Helwan Fertilizers Co.
50	Egypt	Ahmed KAMAL	Production Engineer, Urea	Helwan Fertilizers Co.
51	Jordan	Salem Mohamed Suliman AL NU'MAN	Supervisor (Mechanical)	Indo- Jordan Chemicals Co.
52	Jordan	Thaer Nafeth Husni AL NAJAR	Technician (Inspection)	Indo- Jordan Chemicals Co.
53	Iraq	JASIM AL-ARCHELELL	Head of quality control	Iraqi ministry of industrial & minerals, Al Karamah company
54	Jordan	Samir ABD AL-RAHEEM	Assistant CEO	JAFCCO
55	Jordan	Khaled AL TARAWNEH	HSE Supervisor	JAFCCO
56	Jordan	Ali AL-HUSSAIN	Maintenance Dept. Manager	JAFCCO
57	Jordan	Jamal SHARAIHA		Jordan Phosphate Mines Co (JPMC)
58	Jordan	Khaldoun KRISHAN		Jordan Phosphate Mines Co (JPMC)
59	Jordan	Mohamed Awad TARAWNEH		Jordan Phosphate Mines Co (JPMC)
60	Jordan	Ghaleb AMIRA		Jordan Phosphate Mines Co (JPMC)
61	Jordan	Hani AL AWNEH	Maintenance Engineer	KEMAPCO
62	Jordan	Riyad HABAHEBH	Maintenance Engineer	KEMAPCO
63	Egypt	Eid Mohamed Abdallah EL HOUT	Chairman & Managing Director	KIMA
64	Egypt	Gamal Ismail MOHAMED	Managing Director - Technical	KIMA
65	Egypt	Mamdouh Zaki HAGAR	Sectors Head, Projects	KIMA
66	Egypt	Mohamed Wagih HASSAN	Cairo & Alex, Office	KIMA

			Manager	
67	Egypt	Mohamed Sayed MOSTAFA	Sector Head, Gas & Ammonia Production	KIMA
68	Egypt	Ahmed Abdel Aziz MOHAMED	Sector Head, Labs & Quality Control	KIMA
69	Egypt	Abou Krisha Mohamed HUSSIEN	Sector Head, Fertilizer & Acid	KIMA
70	Egypt	Hassan Mostafa AHMED	Sector Head, Mechanical Engineering	KIMA
71	Egypt	Salem AL-Shahat SALEM	GM, Maintenance	KIMA
72	Egypt	Mohsen Ahmed HAMIMI	GM, Gas & Hydrogen	KIMA
73	Egypt	Saber Abdel Rahman AL-SAYED	GM, Water, Utilities	KIMA
74	Egypt	Mohamed Abou El-Hassan MAHMOUD	GM, Industrial Safety	KIMA
75	Egypt	Sayed Abdel Hadi MOHAMED	GM, Production Control	KIMA
76	Egypt	Essam Eddine Ahmed KHODARY	GM, Ammonia & Pressures	KIMA
77	Egypt	Hussien Mohamed MOSTAFA	GM, Research & Development -KIMA 2	KIMA
78	Egypt	Ramadan Al-Aref MOHAMED	GM, Transportation	KIMA
79	Egypt	Ahmed Mohamed ABDEL MOUTELIB	Manager, Acid	KIMA
80	Egypt	Adel Ali AHMED	Manager, Labs	KIMA
81	Egypt	Mahmoud Ahmed ABDEL MOUTY	Manager, Nitrogen	KIMA
82	Egypt	Sami El-Sayed MABROUK	GM, Workshop	KIMA
83	Egypt	Abou El-Kassem Hussien AHMED		KIMA
84	Egypt	Abdel Moniem Saeed AHMED		KIMA
85	Egypt	Kareema Mahfouz HASSAN		KIMA
86	Egypt	Khaled Youssef HAMED		KIMA
87	Egypt	Ahmed Mahmoud ADAM		KIMA
88	Egypt	Ahmed Hussien METWALLY		KIMA
89	Egypt	Basel Abdel Azeem MOHAMED		KIMA
90	Egypt	Walid Abou El-Wafa AL-NADY		KIMA
91	Saudi Arabia	Maher Bazroun	Staff Engineer	MAADEN Phosphate Company
92	Egypt	Ibrahim ABDEL WAHAB	Head Sector,	Misr Fertilizer Production Company (MOPCO)
93	Egypt	Mahmoud Ahmed SHETTA	Section Head,	Misr Fertilizer Production Company (MOPCO)
94	Egypt	Hatem Mohamed AHMED	Engineer	Misr Fertilizer Production Company (MOPCO)
95	Egypt	Ahmed Ibrahim ISSA	Engineer	Misr Fertilizer Production Company (MOPCO)
96	Egypt	Ibrahim MOSA	Enginner	Misr Fertilizer Production Company (MOPCO)
97	Canada	Mimoun EL BOUJDAINI		Natural Resources Canada
98	Oman	Ali Salim AL SIYABI	Inspection Manager	Oman-India Fertiliser Co.(OMIFCO)
99	Oman	Ahmed Andullah AL FARSI	Cibil Supervisors	Oman-India Fertiliser Co.(OMIFCO)
100	Oman	Nasr Hamdan AL GHAILANI	Mechanical Engineer	Oman-India Fertiliser Co.(OMIFCO)

101	Oman	Mohammed Obaid AL HABSI	Planning Engineer	Oman-India Fertiliser Co.(OMIFCO)
102	Jordan	Walid ABU HASSAN	Managing Director	Orient Shipping Co. Ltd
103	Kuwait	Jassim AL NOURI	Environment Engineer	Petrochemical Industries Company (PIC)
104	Kuwait	Sultan AL ZAFERI	Workshop Engineer	Petrochemical Industries Company (PIC)
105	Kuwait	Abdullah AL AZMI	Workshop Engineer	Petrochemical Industries Company (PIC)
106	Kuwait	Ali Jawad TAQI	Engineer	Petrochemical Industries Company (PIC)
107	UAE	Adel AL WAHEDI	Senior Mechanical Engineer	Ruwais Fertilizer Industries (FERTIL)
108	UAE	Ali ALIA	Technical Manager	Ruwais Fertilizer Industries (FERTIL)
109	Saudi Arabia	Abdulaziz Al-Mady	General Manager, SABIC Africa	Saudi Basic Industries Corporation (SABIC)
110	Egypt	Ibrahim ABDEL HAY	Chairman & Managing Director	SEMADCO
111	Egypt	Ahmed Gharib KHAISSAM	Head, Economic Sector	SEMADCO
112	Egypt	Mohamed HAMED	Managing Director - Technical	SEMADCO
113	Egypt	El-Sayed Abdel Gawad OWIDAT	Consultant - Electricity Sector	SEMADCO
114	Egypt	Abdel Moniem ABU EL-JHAR	Head Sectors, Engineering	SEMADCO
115	Egypt	Mahmoud Mehasseb BARBARY	Instrument, Head Sector	SEMADCO
116	Egypt	Ahmed AWAD	GM, Finance	SEMADCO
117	Egypt	Adel ABOU EL-ALA	Consultant B - Production Control	SEMADCO
118	Egypt	Khaled Mostafa IDRIS	Maintenance Manager	SEMADCO
119	Egypt	Hassan Ahmed HASSAN	Production Manager	SEMADCO
120	Egypt	Ramadan Ahmed SOLIMAN	Maintenance Manager, Sulphur	SEMADCO
121	Iraq	Salim AL MALIKY	Director General	State company of Southern Fertilizer
122	Iraq	Oday AL KANAAN	Chief Engineer	State company of Southern Fertilizer
123	Iraq	Hajir SWAILM	Cheif Engineer	State company of Southern Fertilizer